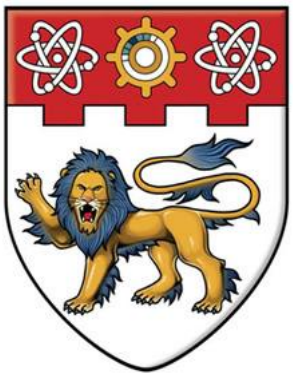

NANYANG TECHNOLOGICAL UNIVERSITY

FIBER OPTICS CHEMICAL SENSORS BASED ON RESPONSIVE POLYMERS

TOU ZHI QIANG

SCHOOL OF CHEMICAL AND BIOMEDICAL ENGINEERING

2015

FIBER OPTICS CHEMICAL SENSORS BASED ON RESPONSIVE POLYMERS

TOU ZHI QIANG

School of Chemical and Biomedical Engineering

A thesis submitted to the Nanyang Technological University

In fulfilment of the requirement for the degree of

Doctor of Philosophy

2015

Statement of Originality

I hereby certify that the work embodied in this thesis is the result of original research done by me and has not been submitted for a higher degree to any other University or Institute.

.....	.....
Date	**Tou Zhi Qiang**

Acknowledgments

Postgraduate studies represent a quantum leap from the structured education experienced during the undergraduate days. This is especially so when given the free rein by one's supervisor to pursue any research interest. Nevertheless, this process of self learning and carving one's direction has taught me many invaluable lessons applicable in later stages of my life.

I will perhaps one day fondly recall the seemingly endless lonely time spent in the laboratory, reminiscence about the times I have to pick myself up after yet another failed experiment, the long walks around the vast campus as I resist the latest impulse to quit, lament about the unappetizing canteen food and the long train ride home.

The PhD journey, although that of self learning, is never a path undertaken alone. I would like to express my gratitude to friends who are willing to lend a listening ear even though they do not have the slightest inkling of my work or difficulties, friends who offer sincere words of encouragement when I am down, labmates (Dr Henry, Lihan, Weichang, Yifan) who show me the ropes and who offer me kind words of advice, collaborators (Dr Eddie, Dr Terrence) who share their experience, undergraduates (Jesmond, Maggie, Marcus, Shermaine, Stephanie, Zhirong) whom I have supervised for tolerating my occasional rants and who add much joy and laughter to an otherwise somber laboratory.

I would like to thank my supervisor, Professor Chan Chi Chiu for instilling in me confidence and independence through his abeyant supervision. I would also like to

express gratitude to Dr Emm. Mic. Drakakis for taking time off his hectic schedule to advice me.

Lastly, I would like to thank Ailing, Bernice, Choon Kit, Darwin, Dr Henry, Jane, Kian Hong, Shurui for their companionship in a land thousands of miles away from home and my family for their unwavering support and love.

Zhi Qiang

Jan 2014

Abstract

Fiber optic chemical sensors (FOCS) have made tremendous progress since developments began in the 1960s with continuous reports of new configurations, materials and applications even today. Techniques like interferometry and plasmonic resonance are set to form the next generation of FOCS, representing a deviation from conventional luminescence based techniques.

The thesis presents an optic fiber sensor platform for localized surface plasmon resonance (LSPR) by using a speciality photonic crystal fiber (PCF) to excite LSPR via cladding modes. The sensor offers facile fabrication and achieves high refractive index sensitivity of -731 % transmittance/RIU with limit of detection (LOD) 1.76 x 10^{-5} refractive index unit (RIU).

Responsive polymers, exhibiting physio-chemical changes when exposed to specific stimuli are investigated for feasibility in FOCS based on LSPR and interferometry. A pH sensor is proposed by formation of a gold nanoparticles (AuNPs) embedded polyelectrolyte multilayer (PEM) consisting of Chitosan and poly(styrene sulfonate) (PSS) onto the forementioned sensor. The sensor exhibits pH responsiveness between physiological range of pH 6.5 to 8 and its behavior can be modeled by the Henderson-Hasselbach equation. The biocompatibility of the materials enables in-vivo application of the sensor.

Interferometry FOCS using hydrogel as sensing material are investigated. Mach Zehnder interferometers (MZI) can be constructed from PCF. A proposed double-pass MZI shows higher Q factor and higher resolution than a single-pass MZI. By

coating a thin poly(HEMA-co-DMAEM) hydrogel film, the MZI pH sensor shows a linear pH response with pH 6.75 to 8.25 (R^2 = 0.986) with LOD pH 0.004. The sensor is successfully applied to the monitoring of cell culture media.

A generalized approach in fabricating hydrogel based interferometric sensors is demonstrated through use of poly(vinyl alcohol) (PVA)-co- poly(acrylic acid) (PAA) hydrogel. The PVA/PAA offers tremendous ease in obtaining thin films on optical fiber via simple dip coating without need for additional cross linkers and polymerisation initiators. The carboxyl groups on PAA offer efficient coupling to a variety of aminated receptors using carbodiimide coupling to realise a myriad of sensing possibilities. The biocompatibility of both PVA and PAA also makes the proposed sensing film suitable for in-vivo applications. The sensor is demonstrated for sensing of small chemical species like Ni^{2+}. It was found that sensitivity of the PVA/PAA is affected by the PVA/PAA ratio and duration of heat induced esterification which controls the degree of cross linking and the maximum amount of receptors that can be immobilised. The optimal PVA/PAA hydrogel is fabrication from a 12:6 wt % ratio and cross linked at 130 ^{o}C for 30 min. By modifying the PVA/PAA hydrogel with hydroxyquinoline, the sensor is able to detect Ni^{2+} with good sensitivity 0.214 nm/μM and LOD 1nM adequate for continuous monitoring of drinking water.

List of Abbreviations

8HQ	8-hydroxyquinoline
APS	ammonium persulfate
Ch	chitosan
DMAEM	2-(dimethylamino)ethyl methacrylate
EGDMA	ethylene glycol dimethacrylate
FBG	fiber Bragg grating
FESEM	field emission scanning electron microscopy
FOCS	fiber optic chemical sensors
FTIR	Fourier transform infra-red spectroscopy
HEMA	2-hydroxyethyl methacrylate
LBL	layer-by-layer
LED	light emitting diode
LOD	limit of detection
LPG	long period grating
LSPR	localized surface plasmon resonance
MIP	molecularly imprinted polymer
MMF	multimode fiber

PAA	poly(acrylic acid)
PCF	photonic crystal fibers
PEM	polyelectrolyte multilayers
PSS	poly(sodium 4-styrenesulfonate)
PVA	poly(vinyl alcohol)
QCM	quartz crystal microbalance
RIU	refractive index unit
SAW	surface acoustic wave
SERS	surface enhanced Raman spectroscopy
SMF	single mode fiber
SPR	surface plasmon spectroscopy
SPW	surface plasmon wave
TEMED	N, N, N', N'- tetramethylethylenediamine
TMSPM	3-(Trimethoxysilyl)propyl methacrylate

Table of Contents

List of Figures

List of Tables

Chapter 1

Introduction

1.1 Motivation and objectives

The advent of optical fibers has brought a significant impact on our data communication, however, the use of optical fibers is by no means limited to telecommunications. One other application field of optical fibers is in analytical chemistry, especially since the analytical sciences have traditionally involved optical techniques like absorption, fluorescence, refractometry, etc.

The use of optical fibers for chemical/biochemical sensing has made much progress since developments began in the 1960s. Initial fiber sensors were limited to detecting chemical species with intrinsic optical properties like colour or luminescence. However, progress in indicator chemistry have seen the use of indicator dyes that change their optical properties in response to a chemical species of interest for fiber sensing of pH, dissolved oxygen, carbon dioxide, etc [170]. Biomolecules including antibodies, enzymes, DNA have also increasingly been used for fiber based biosensors [22].

It is without doubt that optical fiber chemical sensing is a promising technology with novel fiber configurations, materials and applications continuously reported. Amongst the optical techniques, wavelength measurement based techniques like interferometry and plasmonic resonance appear most encouraging for the next generation of fiber optic chemical sensors (FOCS) owning to their high sensitivity, label-less approach with potential for real time, multiplex sensing. Meanwhile, responsive polymer materials that display change in its physio-chemical properties

in response to its environment are playing an increasingly prominent role in diverse applications including sensing [77].

This has prompted the investigation of fiber optics for interferometry or plasmonic resonance based sensing and the incorporation of responsive polymers to fulfill a fully functional FOCS which is the main objective of the thesis.

1.2 Organization of thesis

The thesis is organised as follows:

Chapter 2 aims to introduce readers to FOCS and the advantages of an optical fiber based sensing platform. The principles of light guidance in an optical fiber and the various optical techniques used for sensing will be reviewed. The myriad of optical techniques necessitates a brief introduction of each technique, however, surface plasmon resonance (SPR) and interferometry techniques will be dealt with in further detail owning to the promising potential of these techniques and because of their relevance in later chapters. Responsive polymers and the principles behind their application for sensing will be introduced. Through a brief overview of reported transducers for responsive polymers that follows, it is hoped to impress upon readers the immense sensing possibilities that responsive polymers could bring to FOCS and the aptness of the FOCS for responsive polymer based sensing that are the main focus for the thesis.

Chapter 3 reports a localised surface plasmon resonance (LSPR) refractometer based on a novel fiber configuration consisting a short segment of photonic crystal fiber (PCF) fusion spliced in between multimode fibers. In contrary to common reported sensors, the sensor utilises the evanescent field of cladding modes instead

of core modes for excitation of LSPR, hence providing tremendous ease in fabrication while improving sensitivity.

Chapter 4 is a continuation of work in Chapter 3 whereby the reported LSPR sensor is used for pH sensing by the embedding of gold nanoparticles (AuNPs) within a pH-responsive polyelectrolyte multilayers (PEM) that is coated onto the fiber by the layer-by-layer technique. The LBL technique offers a facile technique for coating optical fibers with precise control of thickness, properties. The pH response of the sensor in buffer solution is characterised based on transmittance change and LSPR peak shift. The data corresponds well with the extended Henderson-Hasselbach model of pH behaviour of weak polyelectrolytes. The biocompatibility of the materials used in the PEM enable the sensor for future in-vivo applications.

Chapter 5 marks the beginning of the author's work on interferometry based FOCS. Fiber interferometers have previously been reported for physical parameters like temperature, strain and have only recently been adopted for chemical sensing owning to their sensitivity, facile readout and dynamic range. A novel double pass Mach Zehnder fiber interferometer is proposed and reported to have a higher Q factor than a single pass interferometer of the same dimensions. pH responsive hydrogel is coated on the sensor and the sensor shows a linear response to pH within the physiological range. The sensor is demonstrated for application in the monitoring the in-vitro pH change in a cell culture of human melanoma cells and provides an insight between extracellular pH and proliferation of cancer cells.

Chapter 6 aims to fulfil the sensing possibilities of responsive polymers based FOCS by outlining a versatile platform that can easily be adapted for sensing various

analytes. The platform is demonstrated on a Mach Zehnder fiber interferometer using a poly(vinyl alcohol) (PVA)/poly(acrylic acid) (PAA) hydrogel. The PVA/PAA hydrogel can be easily formed on optical fiber via dip coating and thermal induced cross linking. The hydrogel is later modified with chemical receptors with an amino end using carbodiimide coupling. The sensor is demonstrated for sensing of Nickel cations using hydroxyquinoline receptor. Various parameters like the degree of cross linking and composition of hydrogel on sensitivity is reported.

Chapter 7 brings a conclusion to the thesis, summarising the key results while providing a glimpse into future work and trend of FOCS.

Chapter 2

Literature Review

According to the IUPAC definition, a chemical sensor is a device that transforms chemical information ranging from concentration of a specific sample component to total composition analysis into an analytically useful signal [1]. It generally consists a chemical receptor that interacts specifically with the analyte molecule while simultaneously changing its physical or chemical properties. These changes are converted by an appropriate transducer into an analytical useful electrical signal that can be processed and recorded by downstream data processing and display units (see Figure 2-1).

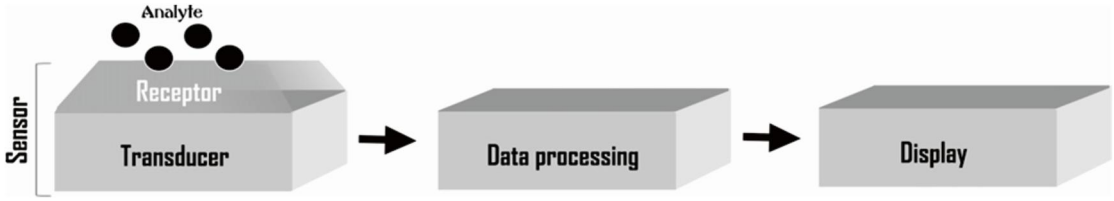

Figure 2-1: General components of a chemical sensor. Reproduced from Ref [89]*.

Fiber optic chemical sensors (FOCS) use optical fibers as transducer and rely solely on optical transduction techniques for detecting chemical species. Building a sensor around an optical fiber platform can offer several advantages including:

1. A vast variety of optical based techniques for chemical analysis including spectroscopy based techniques like fluorescence, absorbance, surface plasmon spectroscopy (SPR), localized surface plasmon resonance (LSPR), Raman spectroscopy, Fourier transform infra-red spectroscopy (FTIR) and

*Reprinted from Progress in Polymer Science, 37, Daniel Buenger, Fuat Topuz, Juergen Groll, Hydrogels in sensing applications, Page 1680, Copyright (2012), with permission from Elsevier

other techniques like interferometry, grating, etc. A review of these techniques is provided in a later section.

2. Miniature size of optical fiber and ability to transmit light over long distances enable remote sensing in difficult-to-access areas without the need for receptor elements to be in close proximity to the downstream processing units.
3. Relative inertness of silica optical fibers enables usage in harsh environments.
4. Use of light instead of electric current or voltages circumvent the problem of electromagnetic interference and is deemed safer for in-vivo applications.
5. Capability for multiplex sensing since an optical fiber can guide light of different wavelength simultaneously, it is envisioned that each wavelength can be designated for a particular analyte, thus several analytes can be detected on a single optical fiber.
6. Low cost. The use of optical fibers in telecommunications have driven prices down tremendously even for specialty fibers designed for guiding light of particular wavelengths with minimal losses.

In the following sections, a brief introduction to light guidance in optical fibers crucial in understanding FOCS will be provided, after which an overview of optical techniques is presented, highlighting the various advantages and disadvantages wherever possible. In the later sections, responsive polymers will be introduced. These polymers show changes in physical/chemical properties in response to specific stimuli and have been actively investigated for sensing applications. Common transducers for responsive polymers will be reviewed. It is hoped that readers will appreciate how polymers represent an exciting class of sensitive materials and in conjunction with fiber optics provide limitless sensing possibilities

(not limited to chemical but also biochemical) while taking full advantage of a fiber optics system.

2.1 Light guidance in optical fiber and the evanescent field

2.1.1 Light guidance in optical fiber

The basic construct of an optical fiber consists a concentric core surrounded by an outer cladding layer. In silica fibers, the core is usually doped with Germanium such that the core refractive index, n_{core} is larger than cladding refractive index, n_{clad}. Light is guided within the core via total internal reflection off the core-cladding interface. Thus, for light to be guided within an optical fiber, the incidence angle, θ must fulfill a critical angle criteria (derived from the Snell's Law and shown below), failing which it will leak from the core and be lost.

$$sin\theta > \frac{n_{clad}}{n_{core}}$$

However, only light rays with discrete values of θ fulfilling the Snell's Law are actually guided by the optical fiber. Each of these specific rays is referred to as a mode which represents a spatial distribution of optical energy that remains constant in time. The number of modes and their spatial distribution can be found from the solution of Maxwell equations while applying the field boundary conditions at the core-cladding interface [2].

Interested reader can refer to Ref [2] for mathematical derivation of the modes. Perhaps, a more intuitive way of understanding the modal propagation of light can be achieved by visualizing the light ray as a plane wave (see Figure 2-2). Each plane

or a wavefront, sharing similar phase and other properties, is normal to the direction of propagation of the light beam. Upon reflection, the planes undergo a phase shift and it is necessary for the planes to remain in phase with the planes before reflection to avoid canceling each other due to destructive interference. Hence, there is only a finite number of paths that light can propagate along the fiber with minimal loss.

In general, for a uniform refractive index core, an important parameter often called the V number can be defined [2]:

$$V = \frac{2\pi a}{\lambda}\sqrt{n_{core}^2 - n_{clad}^2}$$

where α is the radius of the fiber core and λ is the wavelength of light.

For V number below ~2.405, an optical fiber supports only one mode (seen as a single ray of light as shown in Figure 2-2). These fibers supporting only a single mode is aptly called single-mode optical fibers.

For larger V number, the number of supported modes is approximated as $V^2/2$ and fibers that support more than one mode usually have larger optical core diameter and are called multiple-mode fibers.

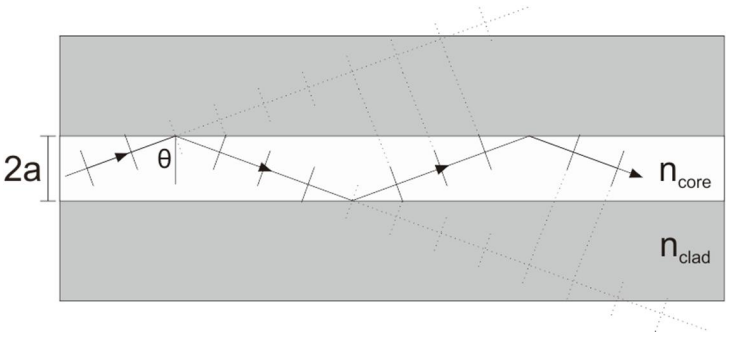

Figure 2-2: Longitudinal section of an optical fiber showing guided ray. Constructive interference between the wavefronts (dashed lines) leads to a guided mode.

2.1.2 Evanescent field

Part of the light reflecting off the core-cladding interface via total internal reflection actually penetrates slightly into the cladding in the form of an evanescent field. This evanescent field is strongest at the interface and decays exponentially into the cladding. The penetration depth, which characterizes the distance at which the evanescent field decays to 1/e of the value at the interface is given by [22]:

$$d_p = \frac{\lambda}{2\pi\sqrt{n_{core}^2 sin^2\theta - n_{clad}^2}}$$

The magnitude of evanescent field, E:

$$E = E_o \exp\left(\frac{-x}{d_p}\right)$$

where E_o is the strength of the evanescent field at the interface and x is the distance away from the interface.

For typical values of n_{core} and n_{clad}, the penetration depth for visible light is in the order of hundred of nanometers, representing a small sensing volume surrounding the core-cladding interface whereby exchange of optical energy with the guided core modes can take place. This is the basis of evanescent wave spectroscopy and other optical fiber based techniques including SPR, LSPR that utilize the evanescent field to excite fluorophores or plasmonic resonances. This will be elaborated further in section, §2.3 on optical techniques.

2.2 Photonic crystal fiber

Improving upon the conventional optical fiber introduced in §2.1, photonic crystal fibers (PCF) represent the next revolutionary frontier of fiber optic technology. Conceived in the 1990s, these fibers guide light by confining it within a periodic array of microscopic air holes running along the entire fiber length [3]. This periodic wavelength scale microstructures strongly reflect light of certain wavelength and incidence angles and when properly designed, exhibit photonic bandgap phenomenon which block light propagation in every direction as long as its wavelength falls within the range spanned by the photonic bandgap.

This unique ability has enabled the design of PCF in which light is guided within a low refractive index hollow air core, thereby achieving unique properties like low-loss single-mode transmission, tunable birefringence and chromic dispersion, and temperature sensitivity which are unattainable with conventional fiber optic technology. The diversity of new and improved optical properties of PCF result in its application in ever increasing areas of science and technology like high harmonics laser generation [4], supercontinuum generation [5], atom and particle guidance [6] which have contributed to the continued research interest in PCF.

2.2.1 Solid core PCF

There are two distinguished types of PCF. The solid core PCF (see Figure 2-3a) is the first PCF to be fabricated in 1995 [7]. It has a hexagonal close-packed array of small air channels approximately 300 nm in size spaced 2.3 μm apart surrounding a central solid silica core. The holes of this PCF were too small to support a photonic bandgap and the mechanism for light transmission is a modified form of total internal reflection since the average refractive index of the cladding is lower due to

the holes. An interesting property of this PCF is it is endlessly single mode—light is guided in single fundamental mode regardless wavelength. The intriguing behavior can be understood by viewing the air holes as a modal sieve that allows narrow lobed higher modes to escape. By appropriate design of hole size (d) and spacing (Λ), higher order modes can be trapped. For $d/\Lambda < 0.4$, it is shown that only the fundamental mode is guided and this has enable large mode area fiber with benefits for high power delivery, amplification and laser to be designed.

a) **b)**

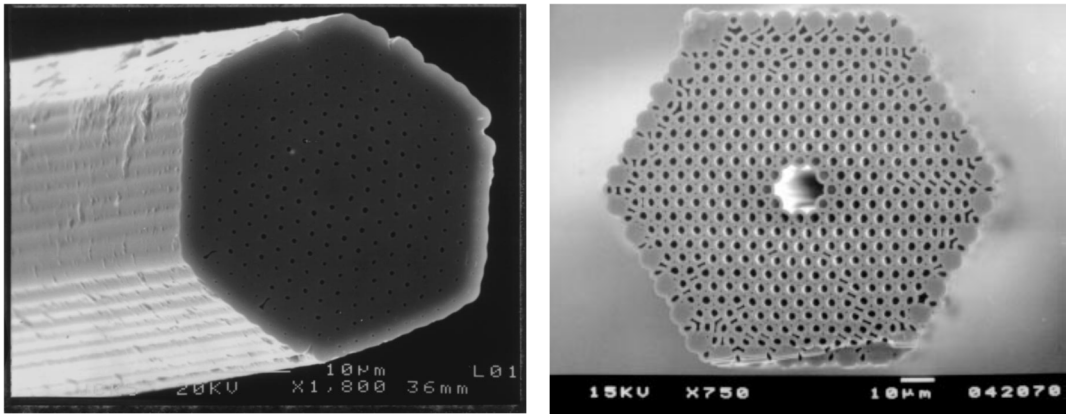

Figure 2-3: SEM micrograph of (a) solid core PCF and (b) hollow core PCF. Adapted from Ref [7] and Ref [8] respectively.

2.2.2 Hollow core PCF

Hollow core PCF (see Figure 2-3b) is demonstrated later in 1998 when technology enables fabrication of fibers with larger air holes. The first reported hollow core PCF [8] has a simple triangular lattice of holes surrounding a hollow core. Launching white light into the fiber causes the transmission of colored modes, indicating guidance of light of certain wavelength coincident with the photonic bandgap. Since light is transmitted in a hollow core, these fibers have potential for

low loss transmission due to reduced Rayleigh scattering arising from silica imperfections.

2.2.3 PCF for sensing applications

PCF has been proposed for sensing application taking advantage of the unique air holes that may serve as microfluidic channels through which the analyte interacts intimately with the transmitted light within the core. Gauvreau et al proposed a PCF based surface plasmon resonance sensor in which the core mode excites plasmon wave on the surface of a thin metal film embedded in the fiber microstructure [9]. By measuring fluorescence within the microholes of the PCF, large background luminescence can be minimized, enabling nanomolar detection of fluorescent molecules [10]. PCF has also been used as a platform for Raman scattering measurement of microliter analyte solution [11]. The inconvenience of injecting and withdrawing aqueous samples within the air holes has so far limited practical usage of PCF to gas sensing applications [12].

2.3 Optical techniques

Optical techniques are optical based methods used to report capture of target analytes on the receptors. Figure 2-4 provides an overview of optical techniques that have been utilized by FOCS. According to the optical technique used, FOCS can be broadly classified as direct and indirect sensors. The former detects analytes based on their intrinsic optical properties while the latter uses an intermediate reagent that report the presence of the analyte.

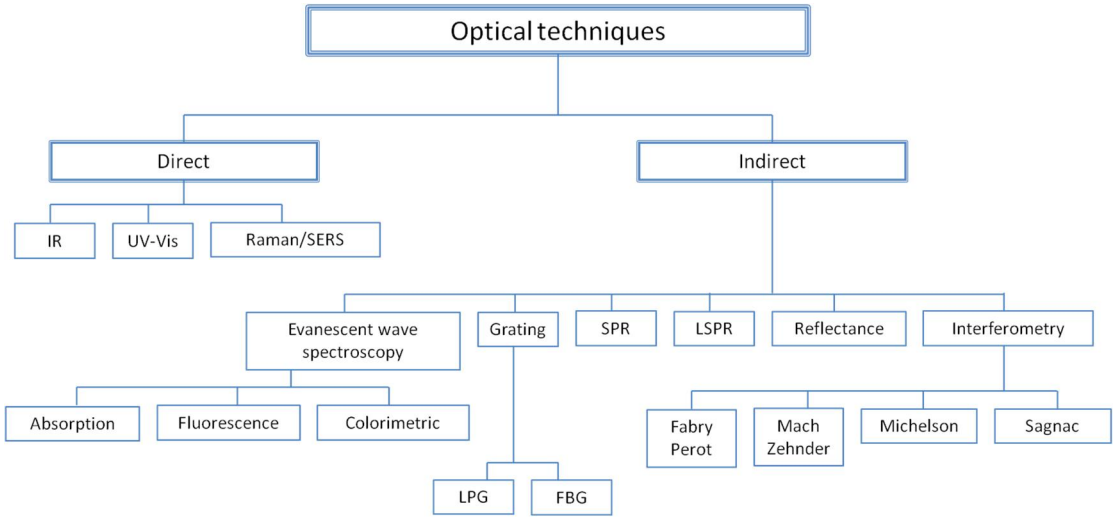

Figure 2-4: Optical techniques used by FOCS.

2.3.1 Direct optical techniques

Direct optical sensors measures the intrinsic properties of the analyte such as IR absorption, UV-Vis absorption or Raman/SERS and have mostly been limited to gas sensing.

2.3.1.1 IR spectroscopy

IR spectroscopy has been used for detection of gases like, CO_2, CO, NO_2, NH_3 and CH_4 that absorb at specific IR wavelengths corresponding to vibrational modes of the molecule [13, 14]. Photonic crystal fibers (PCF) which are specialty fiber that guide light using a regular array of air holes, have been used as gas cells that provide long interaction length between gas and light in the detection of methane [15].

2.3.1.2 UV-Vis spectroscopy

Molecules with π-electrons or non bonding electrons can absorb electromagnetic energy in the ultraviolet to visible range to excite these electrons to higher molecular orbitals and thus can be directly detected by UV-Vis spectroscopy. Tao et al uses a light guiding, flexible fused silica capillary for monitoring Cr (VI) ions in water via

evanescent field absorption spectroscopy based on Cr (VI) instrinsic absorption at 374 nm [16].

2.3.1.3 Raman spectroscopy and surface enhanced Raman spectroscopy

Raman spectroscopy makes use of the Raman effect whereby a molecule scatters photons that interact with its vibrational energy levels [17]. Since each molecular species will have its distinct Raman "fingerprint", Raman spectroscopy is a highly selective technique but suffers from poor signal-to-noise ratio owning to low Raman scattering cross sections. Surface enhanced Raman scattering (SERS) overcomes the weak Raman effect by bringing nanostructured metals in close proximity with the analyte to amplify Raman scattering [18]. Khijwania et al presents a fiber optic Raman sensor based on a Y reflection probe to sense ethanol/methanol concentration in an aqueous solution [19]. Lucotti et al uses a silver nanoparticles coated tapered optical fiber tip as a SERS probe for detecting crystal violet and malachite green [20].

2.3.2 Indirect optical techniques

Most FOCS uses indirect optical techniques requiring an intermediate reagent to report the presence of an analyte. In most cases, these intermediates are also the receptors that undergo an analyte-dependent change in optical properties mainly fluorescence, absorption, colour change, or refractive index that is converted by the transducer.

2.3.2.1 Evanescent wave spectroscopy

The overwhelming majority of optical techniques used is the evanescent wave spectroscopy first mentioned in §2.1.2. The evanescent field of core mode can be made to excite a fluorophore and its fluorescence is directed by the fiber to the photodetector (the techniques is also known as total internal reflection of fluorescence, TIRF) or be absorbed, resulting in overall decline in light intensity at the detector (the techniques is also known as attenuated total reflection, ATR). Ref [21] provides a review of common optical fiber configurations for indirect optical techniques utilizing the evanescent field whereby the fiber cladding is usually removed or modified with the intermediate reagent. Tapering [22] and bending [23] of fibers are used to increase evanescent field interaction with reagent.

2.3.2.2 Reflectance

Reflectance is another common technique. Colorimetric, absorbing materials or material exhibiting a refractive index change have been coated on the distal end of a fiber (where light is reflected) that is bifurcated on the other end to connect both the light source and photodetector. The presence of the analyte alters the reflected intensity or spectrum (refer to Table 2-1).

2.3.2.3 Fiber Bragg grating

Fiber Bragg gratings (FBG) like long period gratings (LPG) (§2.3.2.4) are fiber based gratings and have also been used in FOCS. A FBG is an optical fiber with a periodic modulation of refractive index that has been inscribed into its core [24]. This periodic modulation reflects a set of beams when the FBG is illuminated with

a broadband light source that destructively interferes with one other unless the Bragg's law is fulfilled:

$$\lambda_B = 2n\Lambda$$

where n is the effective core index and Λ is the period of the refractive index modulation.

FBGs have long been reported for measurement of physical parameters like temperature, strain and pressure. Any alterations in these parameters changes the period of the core index modulation, thus varying the Bragg wavelength, λ_B. More recently, FBGs have also been explored for chemical sensing.

Cong et al [25] reported a salinity sensor by coating acrylamide hydrogel on a FBG. Swelling of the gel in response to salinity exerts mechanical stress on the FBG, changing the core index period. However, the well-known cross sensitivity of FBG based sensors to temperature and strain have so far limited their use in chemical sensing. Newer generation of FBGs like tilted FBG promise elimination of temperature cross sensitivity by referencing to cladding mode resonance [26] but its application in chemical sensing has not been explored.

2.3.2.4 Long period grating

Similar to FBG, LPG also has a periodic refractive index inscribed into its core but this is where the similarities end. The period of the refractive index modulation of the latter is much larger in the range of 100 μm to 1mm and promotes coupling between forward propagating core and cladding modes [27]. Since cladding modes are highly attenuated, the transmission spectrum of LPG demonstrates transmission minima each representing coupling to a particular cladding mode.

LPGs have been used for chemical sensing due to their sensitivity to the refractive index in the region surrounding the LPG. The change in refractive index alters coupling between the core and cladding modes, leading to a phase shift in the wavelength of transmission minima. The relationship between the transmission LPG minima wavelength (λ_{LPG}) and grating period (Λ) is given by

$$\lambda_{LPG} = \left(n_{core} - n_{cladding,m}\right)\Lambda, \qquad (m = 1, 2, \dots)$$

where n_{core} and $n_{cladding,m}$ are the effective indices of the core mode and the m^{th} cladding mode respectively.

A hydrogen sensor has been fabricated by coating a Pd nanolayer on a LPG. Hydrogen interact strongly with the metallic film [28], changing its refractive index. LPGs are also known to suffer from cross sensitivities to temperature, bending, etc.

2.3.2.5 Surface plasmon resonance

The potential for SPR for the monitoring of chemical process was recognized in the late seventies [29], leading to the successful demonstration of gas sensing and biosensing in 1982 [30]. SPR sensing has received much attention from the research community ever since with development and reports of new SPR configuration and applications. Much of this attention is due to its potential for real time analysis of chemical/biochemical interactions without the use of labeled molecules.

The phenomenon of SPR arises from quantum of charge density oscillation (surface plasmon oscillation) along a metal-dielectric interface. These oscillations are accompanied by a p-polarized electric wave (surface plasmon wave, SPW) that decays exponentially in the metal and dielectric with maximum intensity at the

metal-dielectric interface. The propagation constant of this SPW, K_{SPW}, is dependent on both metal and dielectric and is found from solution of the Maxwell's equation:

$$K_{SPW} = \frac{\omega}{c}\sqrt{\frac{\epsilon_m \epsilon_s}{\epsilon_m + \epsilon_s}}$$

where ω and c are frequency and velocity of incident light respectively, ϵ_m and ϵ_s are dielectric constant of the metal and dielectric medium respectively.

In fiber optics SPR sensors, the evanescent field (§2.1.2) having propagation constant along the direction of the core-cladding interface is used to excite SPW in thin metal films coated onto the thinned (or removed) cladding fiber [31]. This excitation of surface plasmon transfers energy away from guided light within the fiber, reducing the light intensity transmitted. Hence, for a given frequency of light and dielectric constant of metal, a change in dielectric environment alters the resonance conditions (K_{SPW}), leading to resonance wavelength shift in the transmitted light. This is the basic principle underlying fiber optics SPR sensors.

Srivastava et al [32] reported a fiber optic SPR sensor for glucose detection by the immobilization of glucose oxidase on 50 nm gold film. Dielectric changes to the glucose oxidase film in the presence of glucose gives rise to a shift in resonance wavelength which is monitored.

2.3.2.6 Localized surface plasmon resonance

A closely related technique to SPR is the localized surface plasmon resonsance (LSPR) involving noble metal nanoparticles. The collective charge oscillations within the nanostructure in response to incidence light of resonant frequency leads to strong scattering and absorption within the UV-vis band [33]. For the simple case

of a metallic nanosphere, the optical property can be modeled from Mie theory with the extinction (sum of absorption and scattering), E given by [34]:

$$E(\lambda) = \frac{24\pi N_A r^3 \varepsilon_m^{\frac{3}{2}}}{\lambda \ln(10)} \left[\frac{\varepsilon_i}{(\varepsilon_r + \chi\varepsilon_m)^2 + \varepsilon_i^2} \right]$$

where N_A and r are the area density and radius of metal nanospheres respectively, ε_m is the dielectric constant of the medium surrounding the metal nanospheres, ε_r and ε_i are the real and imaginary parts of the dielectric constant of the metal dielectric function and χ is the aspect ratio of the nanoparticle. Hence, the LSPR of an isolated nanosphere is dependent on material, size and its dielectric environment. For an ensemble of nanoparticles or nanoparticles existing as a colloid, the LSPR also depends on interparticle spacing, resulting in two main mechanisms for transduction of chemical events namely a change in refractive index [35] or nanoparticle aggregation [36].

Besides nanospheres, a variety of metal nano structures have also been investigated for LSPR [37]. Fiber based LSPR sensors involve the immobilization of these metal nanoparticles on the exposed fiber core for excitation by the evanescent field. This will be discussed further in Chapter 3.

2.3.2.7 Interferometry

Fiber interferometry is a relatively new class of fiber optic techniques that is used for chemical sensing. It uses the interference of light that has travelled different optical paths in the fiber, one of which the presence of analyte alters the optical path difference, resulting in a phase shift in the interferogram. Fiber interferometers can give highly sensitive, accurate wide dynamic range readings and measurands can be

quantified by a few methods including change in wavelength, phase, intensity, frequency or bandwidth [38]. Various fiber interferometers like Fabry Perot (see §2.5.7), Mach Zehnder (see §5.1), Michelson and Sagnac are reviewed in Ref [39].

Fabry Perot interferometers are based on the interference pattern produced from the superposition of multiple beams reflected off two highly reflecting surfaces of separated by distance, L. In most fiber optic implementation of the Fabry Perot interferometer, this is reduced to a 2 beam interferometer owing to the weak reflection at the fiber-exterior interface (normal reflection coefficient at silica-air interface is approximately 4%) and coupling loss due to beam divergence (see Figure 2-5a). Changes in L or refractive index of the medium between the reflecting surfaces alters the optical path difference between the 2 beams responsible for a phase shift in the interferogram.

Light is split into two paths (reference and sample) by a coupler and recombined by another coupler in the Mach Zehnder interferometer (see Figure 2-5b). Interaction with the sample for light in the sample path causes an accumulation of a phase difference with respect to light in the reference path.

The Michelson interferometer in Figure 2-5c is similar to the Mach Zehnder except it operates in the reflection mode and the same coupler is used for the splitting and recombining of the light.

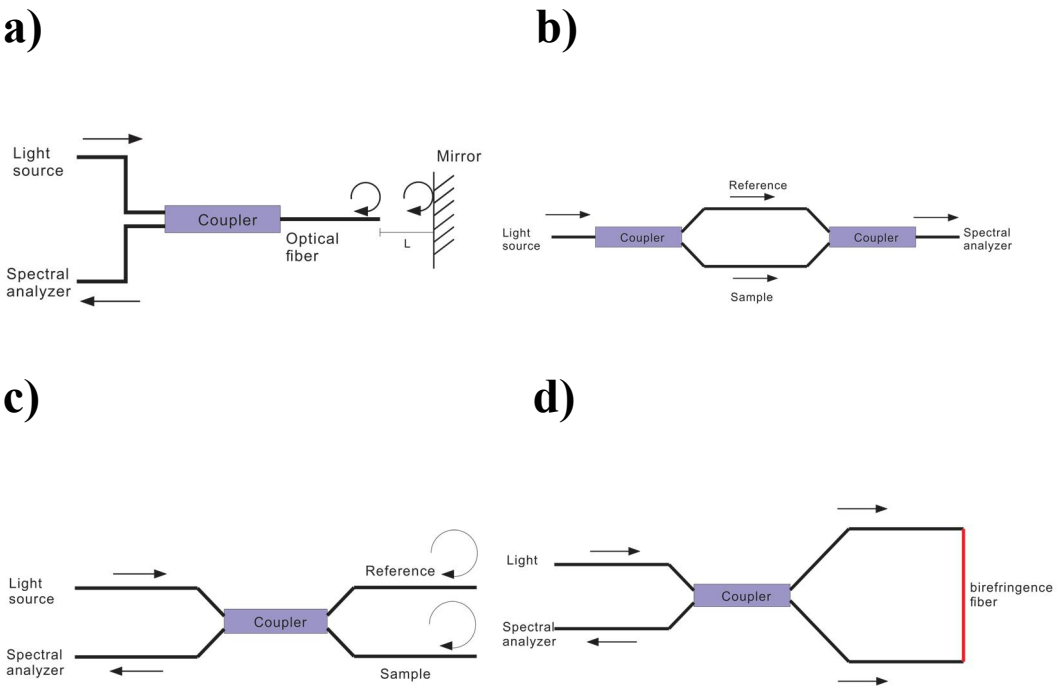

Figure 2-5: Illustration of the (a) Fabry Perot, (b) Mach Zehnder, (c) Michelson, (d) Sagnac fiber interferometers.

The Sagnac interferometer (Figure 2-5d, included here to complete the discussion on fiber optic interferometers but is not used in the author's work) consists a fiber loop containing a segment of birefringent fiber. Light is split by a coupler and the two counter propagating beams are recombined by the same coupler. Beams are polarized along the slow and fast axis of the birefringent fiber and the phase of their interference, ψ is given as [39]:

$$\psi = \frac{2\pi}{\lambda} BL$$

where λ is the wavelength of light, B is the birefringent coefficient of the fiber and L is the length of the birefringent fiber.

2.3.3 Summary of optical techniques

Various materials for indirect sensing and the corresponding optical techniques are summarized in Table 2-1. Intensity measurements based on fluorescence or absorbance still occupy a majority of FOCS and these suffer from instability arising from light source instability, photobleaching, background fluorescence, leaching of fluorophores. Several measures have been proposed to mitigate these problems like ratiometric sensing that ratios optical signal with an analyte independent signal to remove environmental perturbations [40], fluorescence lifetime measurements that measure the decay characteristics of the fluorescence [41] and phase fluorescence method that measures the phase shift between excitation light and emitted fluorescence [42]. However, there may not exist a convenient independent reference point for ratiometric measurements and more complex instrumentation is required for fluorescence lifetime and phase measurements.

Hence, wavelength based methods like SPR, LSPR and interferometry are of particular interest as well as novel sensing materials non reliant on fluorescence or absorption. One such material, responsive polymers are reviewed next.

Table 2-1: Materials for indirect sensing and their optical techniques

Material	Analyte	Optical technique	LOD	Ref
Single walled carbon nanotubes	VOC	evanescent wave spectroscopy		43
Doped polypyrrole	Ammonia	evanescent wave attenuation		44
WO3/Pt film	Hydrogen	evanescent wave attenuation		45
Pd/Au film	Hydrogen	evanescent wave attenuation		46
ZnO film	Relative humidity	evanescent wave attenuation		47
Ir(II) complex	Oxygen	Quenching of fluorophore- evanescent field spectroscopy	0.009%	48
ZnO nanocrystals	Ammonia	absorption- evanescent wave spectroscopy		49
SnO2 nanoparticles	ethanol	absorption- evanescent wave spectroscopy		50
Ti based compound	H2O2	absorption- evanescent wave spectroscopy	74nM	51
8-amino-1-naphthol-5-sulfonic acid	NO2,O3	colorimetric-transmittance	0.64 ppb (NO2) 0.42 ppb (O3)	52
pH indicators (Cresol red, bromophenol blue, chlorophenol red)	pH	colorimetric- evanescent wave spectroscopy		53
Thymol	CO2	colorimetric- evanescent wave spectroscopy		54
Fluorescein	pH	fluorescence- evanescent wave spectroscopy		55
Lunogallion	Al3+	fluorescence- evanescent wave spectroscopy	100uM	56

DNA	Hg2+	fluoresence- evanescent wave spectroscopy	2.1 nM	57
Bacterioirhodopsin film	Ammonia	Absorbance-reflectance	5ppm	58
polypyrrole polymer	methanol, ethanol	Reflectance	1ppm	59
Graphene	Acetone	Reflectance		60
Silver doped zeolite	Hg2+	Reflectance	1ppm	61
2,7-bis(2-arsenophenylazo)1,8- dihydroxynaphthalene-3,6-disulfonate	Pb2+	Reflectance spectroscopy	0.01ppm	62
Ru (II) complex	Oxygen	Quenching of fluorophore-reflectance		63
Pt(II) complex	Oxygen	Quenching of fluorophore-reflectance		64
Pd(II) complex	Oxygen	Quenching of fluorophore-reflectance		65
Pd film	Hydrogen	SPR		66
phytochelatin on AuNP	Cd2+	LSPR	0.16ppb	67
Monoclonal antibodies on AuNP	Pb2+	LSPR	0.27ppb	68
WO3/Pt film	Hydrogen	FBG		69
Silica nanospheres	Relative humidity	LPG		70
Pt film	Hydrogen	LPG		71
Perovskite oxide film	Hydrogen	LPG		72
Zeolite film	methanol, propanol, toulene	Fabry Perot interferometry		73

2.4 Responsive polymers

Responsive polymers or "smart" polymers are polymers that exhibit physico-chemical changes upon receiving a specific external stimulus [77]. These materials represent an area of immense research in a broad range of applications including drug delivery, tissue engineering, sensing, microelectromechanical systems. Various smart systems that respond to a myriad of stimuli including temperature, light, ionic strength, pH, magnetic field, electric field, mechanical force, chemical and biochemical species have been developed. Upon receiving the stimulus, these smart polymers may undergo conformational or chemical changes accompanied by changes in physical properties like volume, refractive index, wettability, permeability, etc [74].

Hence, incorporating these smart polymers onto fiber optics sensor could potentially improve the sensitivity and vastly expand the range of sensing of present sensors. The following section will review some polymeric systems that are of interest for sensing as well as the transducers that are being used to convert the polymers' physico-chemical changes to a readable optical or electronic output crucial in any sensors.

2.4.1 Polymeric brushes

Polymer brushes are chains of polymers that are anchored to a support via appropriate functional group at one end [75]. When grafting density is sufficiently high, the polymer chains are stretched as they encounter excluded volume repulsions. Depending on the properties of the polymer chain and grafting density, reconfiguration of the polymer brush and its properties may be triggered by its environment.

The polymer brushes which may be a homopolymer (Figure 2-6a), co-polymer (Figure 2-6b), or mix of polymers (Figure 2-6c). A homopolymer is a polymer made up of the same type of monomers units. A co-polymer is a polymer made up of two or more types of monomers units. Lastly, a mix of polymers is literally a mixture of 2 or more types of polymers.

In Figure 2-6, 2 types of monomers (green and red) are shown. A homopolymer consists solely of the green monomer is shown in Figure 2-6a. A co-polymer consisting red and green monomers is shown in Figure 2-6b. Figure 2-6c demonstrates a mixture of 2 homopolymers (one consisting only green monomers and one consisting only red monomers). For each subfigure, the 2 contrasting configurations that the polymeric brushes may take in response to external stimuli are presented.

In Figure 2-6a, the homopolymeric brush may assume an extended form or a collapsed form as a result of inter-chain or intra-chain interactions between the same type monomer subunits. Co-polymers brushes also exhibit similar behavior, arising, in the case, from the interactions between different type monomer subunits. In mixed polymer brushes, the environment may favor the display of a polymeric type on the surface over another polymeric type as seen in Figure 2-6c.

The polymer brushes may be prepared by a grafting-to or a grafting-from technique. In the former, synthesized polymer chains are anchored to the substrate with steric hindrance a main stumbling block in achieving a high grafting density. The latter, also known as surface initiated polymerization, involves the immobilization of polymerization initiators that initiate polymerization of brushes from monomers on the substrate surface.

Wu et al [75] reported the fabrication of poly(acrylic acid) brushes on a flat silicon substrate via the grafting-from technique. Wet thickness is found to be dependent upon ionic strength and pH due to charge density dependent extending or relaxing of brushes.

Xu et al [76] proposed a tunable surface based on block co-polymer brushes. Depending on solvent nature that affects balance of electrostatic, hydrophobic and steric forces between the blocks, a particular block could be selectively expressed on the surface.

Mixed polymer brushes consisting of two or more randomly grafted polymer chains exhibit stimuli dependent phase separation that affect material properties on the surface [77]. For instance, mixed polymer brushes consisting hydrophobic polystyrene and hydrophilic poly(acrylic acid) can change its surface wettability according to solvent [78].

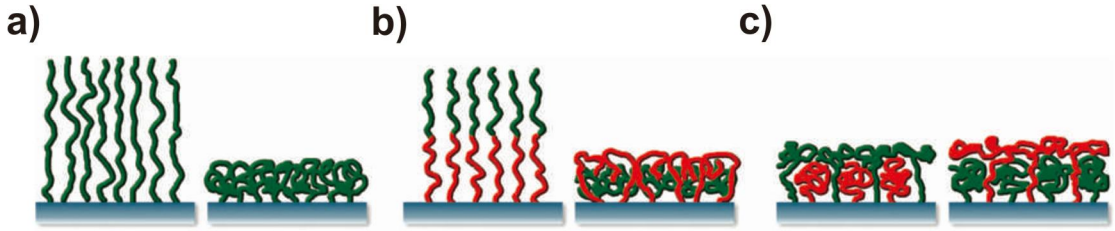

Figure 2-6: Illustration of (a) homopolymer (b) block co-polymer and (c) mixed polymer brushes and their response to stimuli. Reprinted by permission from Macmillan Publishers Ltd: Nature Materials, Ref [77], copyright (2010). http://www.nature.com/nmat/index.html

2.4.2 Layer-by-layer films

Layer-by-layer films are first demonstrated by Decher et al for polyelectrolytes [79]. It involves the cyclical deposition of polyelectrolytes from solution onto a solid surface to build a layered thin film (see Figure 2-7). The method has been adopted

widely for its simplicity in fabricating films on any arbitrary shaped surface with controlled thickness based on the materials used, the number of layers build and deposition conditions including temperature [80], pH [81] and ionic strength [82]. Traditional LBL techniques have been limited to charged polyelectrolytes where electrostatic forces are responsible for holding the layers together, however, recent work has seen LBL systems exploiting hydrogen bonding [83], covalent bonding [84], blurring the distinction between LBL and hydrogel films (to be discussed later). A common pH sensitive LBL is that of poly(allylamine hydrochloride) and poly(acrylic acid) which demonstrate a swelling response in the pH range 3 – 9 [85].

While LBL that shows responsiveness to a variety of stimuli have been reported, they have so far been restricted to non-sensing applications like drug delivery [86]. LBL for sensing has not been commonly reported apart from pH sensing because the sensitivity is not inherent within the film but due to incorporation of responsive materials within the LBL film (e.g. magnetic nanoparticles for magnetic field sensitivity [87]) or due to irreversibility in the LBL response from rearrangement of polymer chains, leading to large hysteresis behavior.

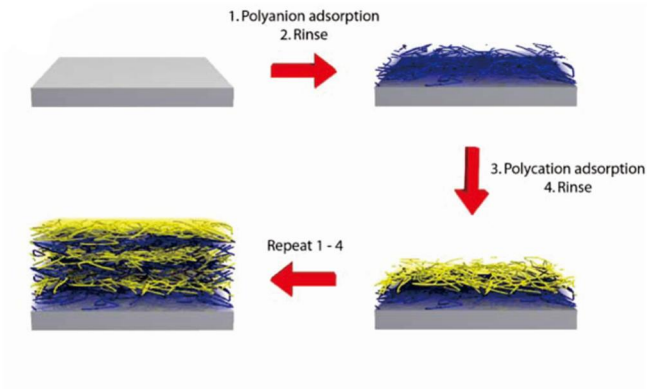

Figure 2-7: Illustration of LBL assembly of polyelectrolytes. Adapted from Ref [88] with permission of The Royal Society of Chemistry.

2.4.3 Hydrogel

Hydrogels are three dimensional hydrophilic polymer network structures formed from crosslinking homopolymers or copolymers and are capable of swelling without dissolution when placed in an aqueous environment [89] (see Figure 2-8). The cross linkages may be physical (hydrophobic interaction, ionic, hydrogen bonding) or chemical (covalent) in nature and give the gel its mechanical and chemical characteristics.

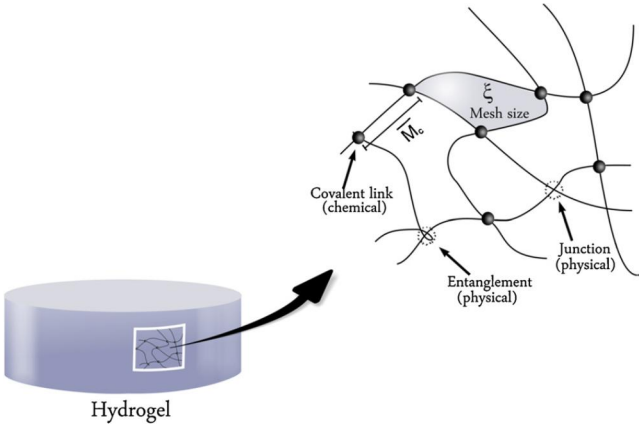

Figure 2-8: Illustration of cross linked hydrogel structure. Ref [89]*.

*Reprinted from Progress in Polymer Science, 37, Daniel Buenger, Fuat Topuz, Juergen Groll, Hydrogels in sensing applications, Page 1682, Copyright (2012), with permission from Elsevier.

Hydrogels are intensively investigated for sensor applications owning to its tunable mechanical and chemical properties that give good sensitivity to external stimuli. In addition, biomolecules like antibodies and enzymes are less likely to denature when immobilized onto the soft hydrogel, making hydrogels a suitable matrix for biosensing applications. The relatively inertness and biocompatibility of most hydrogels enable in-vivo applications.

The key principle of hydrogel as a sensitive material lies mainly in its stimuli dependent swelling response that determines its equilibrium volume. The swelling behavior of hydrogels is most frequently explained by the Flory-Rehner theory [90, 91, 92] which theorizes that the equilibrium volume of a neutral hydrogel network is governed by two opposing forces: osmotic pressure leading to expansion of the hydrogel network and a retracting force resulting from the elastic stretching of polymer chain fragments that resists the expansion. Accordingly, the free energy of the neutral hydrogel (ΔG) is the sum of contribution from elastic retractive forces ΔG_{el} and thermodynamic compatibility between the hydrogel and the surrounding solvent, ΔG_{mix}.

$$\Delta G = \Delta G_{el} + \Delta G_{mix}$$

At equilibrium, the equation can be written in terms of chemical potential, with total chemical potential, μ equaling zero:

$$\mu = \mu_{el} + \mu_{mix} = 0$$

The change in chemical potential arising from elastic forces can be expressed by the theory of rubber elasticity [93] and contributions from the mixing of the hydrogel

in the solvent by the heat and entropy of mixing [94]. Taking into account chemical potential change due to the presence of solvent, the equation can be rewritten [95]:

$$\frac{1}{M_C} = \frac{2}{M_N} - \frac{\left(\frac{\bar{\upsilon}}{V_1}\right)[\ln(1 - v_{2,s}) + v_{2,s} + \chi_1 v_{2,s}^2]}{v_{2,r}[\left(\frac{v_{2,s}}{v_{2,r}}\right)^{\frac{1}{3}} - \left(\frac{v_{2,s}}{2v_{2,r}}\right)]}$$

where

M_c = molecular weight between 2 cross links

M_N = average molecular weight of the polymer chains in absence of cross linkers

$\bar{\upsilon}$ = specific volume of solvent

V_1 = molar volume of solvent

$\upsilon_{2,s}$ = polymer volume fraction in the fully swollen state

$\upsilon_{2,r}$ =polymer volume fraction in the relaxed state

χ_1 =polymer-solvent interaction parameter

Another important parameter of the hydrogel is the mesh size, ξ that determines the diffusional space for movement of solvent or solute through the hydrogel matrix (see Figure 2-8). In many cases, the mesh size plays an important role in the responsiveness of hydrogel based sensors. Assuming isotropic swelling, the mesh size is calculated:

$$\xi = v_{2,s}^{-\frac{1}{3}}(r_o)^{\frac{1}{2}} = v_{2,s}^{-\frac{1}{3}}\left(\frac{2C_N M_C}{M_r}\right)^{\frac{1}{2}} l$$

where

r_o = unperturbed end-to-end distance of the polymer chain between cross link points

C_N = Flory characteristic ratio

M_r = molecular weight of the repeating unit

l = length of the bond along the backbone chain

Various responsive hydrogels have been reported, highlighting its versatility. pH sensitive hydrogel is reported by endowing weak acidic or basic pendant groups within the hydrogel network [96]. Temperature responsive hydrogels are investigated using polymers exhibiting a critical solution temperature like poly(N-isopropylacrylamide) [97]. Biosensing hydrogel are made from functionalising gel with biorecognition elements like enzymes [98], antibodies [99], peptides [100], DNA [101], whole cells [102], etc.

For hydrogels in optical based sensor techniques, the refractive index increase/decrease of the hydrogel as it deswells/swells is most commonly monitored. The refractive index change can be thought to arise from the change in optical density of the hydrogel. The aqueous medium that imbues and surrounds the hydrogel is usually of much lower refractive index than the polymeric chains that make the hydrogel. Thus, as the hydrogel swells, there is increasing proportion of lower refractive index aqueous medium within the hydrogel network, hence decreasing the overall refractive index. The swelling/deswelling behavior has also been monitored optically by the absorbance of plasmonic nanoparticles embedded within the hydrogel [103].

2.4.4 Molecularly imprinted polymer

Molecularly imprinted polymers (MIP) are strictly not responsive polymers in the sense that they do not actively "respond" to a stimulus (as seen in later discussion) but are nevertheless included here for completeness in the review of polymers for sensing applications.

MIP can be thought of as artificial recognition elements capable of binding an analyte with affinity similar to the corresponding receptors [104]. Its fabrication involves the impressing of molecular cavities in a polymer matrix using an analyte or its surrogate which act as a template that is later removed after polymer formation. The removal leaves behind imprinted cavities complementary to the template to which the analyte can fit. Figure 2-9 outlines a general method for preparation of MIP using functional monomers that may interact with templating molecules through covalent, non-covalent, semi-covalent or coordination bonding.

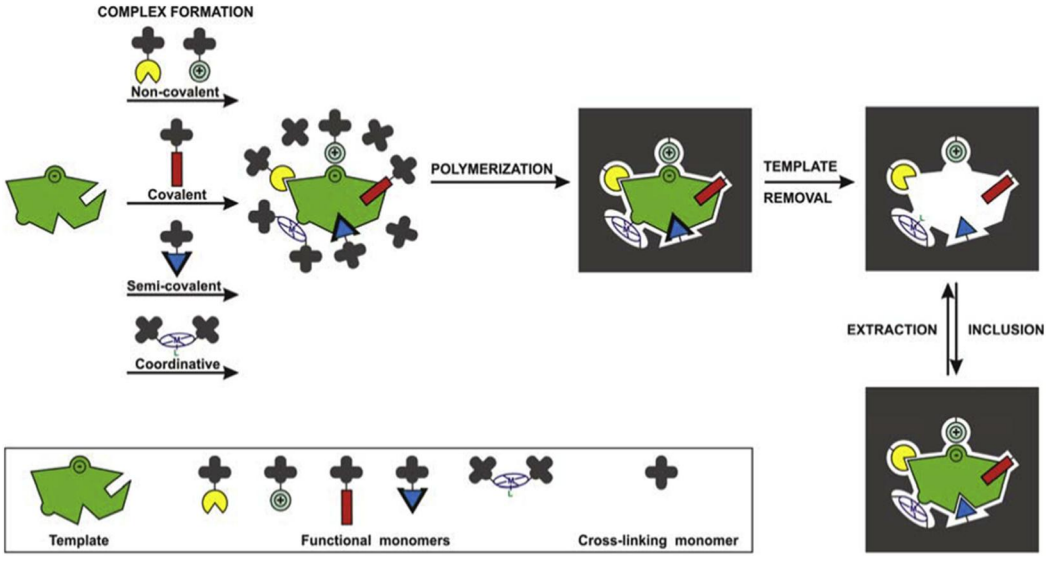

Figure 2-9: Preparation of MIP. Reprinted from TrAC Trends in Analytical Chemistry, 51, Piyush Sindhu Sharma, Marcin Dabrowski, Francis D'Souza, Wlodzimierz Kutner, Surface development of molecularly imprinted polymer films to enhance sensing signals, Page 147, Copyright (2013), with permission from Elsevier.

Various MIP have been reported mimicking many of the natural biomolecules like antibodies, enzymes, nuclei acids that are used for chemical/biochemical sensing [105]. MIP poses significant advantages over these natural biomolecules in their low cost, higher stability to temperature, pH, and ability to function in organic solvent. It is theoretically possible to prepare MIP for any compound.

However, the main challenge in MIP lies in the choosing of an optimal polymerization protocol and the vast magnitude of parameters like types of monomers, cross linkers, solvent, temperature, etc. Choice of monomers has largely been based on the structure of the template and selection is made either empirically [106] or by computational design [107]. Three broad categories of polymers have been used for molecular imprinting:

1. Acrylic monomers like acrylamide to produce a hydrogel matrix
2. Silane monomers to produce sol-gels
3. Thiol derivatives or other surfactants capable of self-assembly to form a 2D sensing surface on a substrate

Table 2-2 provides some examples of polymers used for MIP and their templates.

2.4.5 Summary of responsive polymers

In summary, responsive polymers exist in various forms and hydrogels, in particular, could extend the range of sensing possibilities of fiber optics sensors. Nevertheless, one may need to consider several properties of polymers prior for fiber optic based sensing:

1. Optical properties of the polymers

The polymer should be optically transparent in the optical range tested. The refractive index of the polymer may also be important.

2. Ease of formation/coating on optical fibers

The polymeric material should be easily and precisely coated onto optical fibers with minimal handling, taking into account of the fragile nature of optical fibers.

3. Rate of response of the materials

The polymers should respond rapidly to changes in its environment to ensure the robustness of sensor

Table 2-2: Table of monomer reported for MIP and their template.

Category	Monomer	Template	Ref
1	acrylamide	cytochrome c, transferrin, haemoglobin	108
1	acrylamide and 4-vinylpyridine	BSA	109
1	acrylamide and acrylic acid	Anthrax protective agent	110
1	acrylamide and chitosan	albumin	111
1	agarose	BSA	112
2	aminopropyltrimethoxysilane, tetraethyl orthosilicate	bovine haemoglobin	113
2	3-aminosilane, tetraethoxysilane and octyltrimethoxysilane	BSA	114
2	3-aminosilane, tetraethoxysilane and octyltrimethoxysilane	Staphylococcus enterotoxin B	115
3	11-mercapto-1-undecanol	myoglobin and haemoglobin	116
3	3-aminophenylboronic acid	papain and trypsin	117
3	3-aminopropytrimethoxysilane and trimethoxypropylsilane	haemoglobin	118

4. Amplitude of change in polymer's properties in response to stimuli

The sensor should respond with significant change in its properties in response to minute changes in stimuli. The changes should ideally be reversible with minimal hysteresis.

The stimuli dependent changes to a responsive polymer must be converted by a suitable transducer into an electrical or optical signal for recording and processing purposes. Some commonly used transducers will be reviewed in the next section.

2.5 Transducers for sensing based on responsive polymers

Responsive polymers have been used as sensitive materials in conjunction with various transducers for sensor application. This section reviews several transducers that are commonly reported. These transducers can be broadly classified according to the properties of sensitive material which they transduce which may be mass, charge density, refractive index or volume/shape (see Figure 2-10).

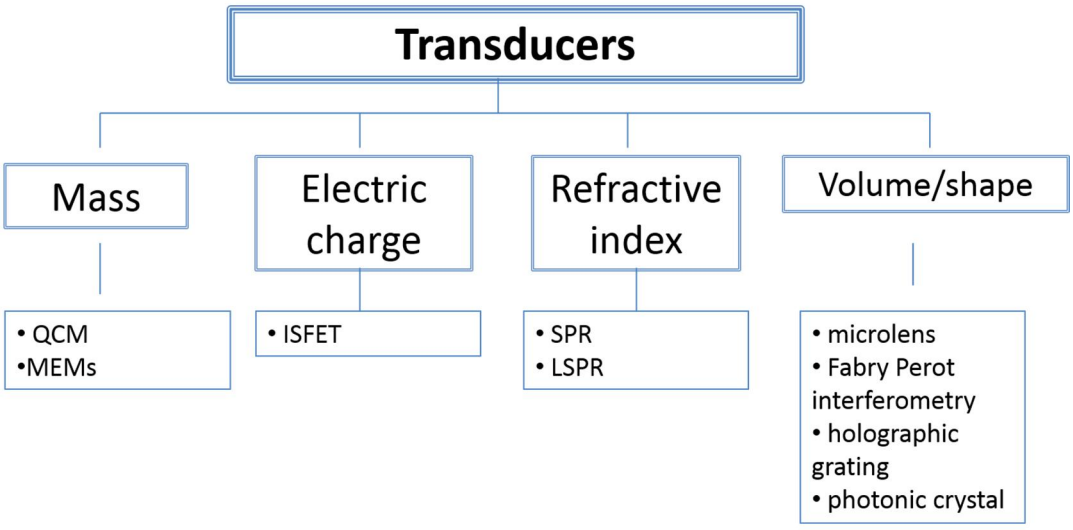

Figure 2-10: Common transducers for stimuli responsive polymers.

2.5.1 Quartz crystal microbalance (QCM)

QCM is an acoustic wave resonator, typically made of a thin piezoelectric quartz disk sandwiched between two gold electrodes [119]. Application of an alternating electric field produces tangential deformation on both surfaces of the disk in parallel and opposite directions. This results in acoustic waves propagating through the disk in a perpendicular direction from the surface that reflect off the surfaces, establishing a resonant condition when wavelength is an odd multiple of the double disk thickness. Small mass changes alter the density of the quartz crystal that affects acoustic wave velocity, changing the resonant frequency. This change in frequency, Δf_o with respect to small mass change, ΔM is the basic principle of QCM based sensors and is described by the Sauerbrey equation [120]:

$$\Delta f_o = -\frac{2}{\sqrt{Ep}} f_o^2 * \frac{\Delta M}{A}$$

where A, E and p are area, shear modulus and density of the quartz crystal.

2.5.2 Microelectro-mechanical systems (MEMS)

Improvement in integrated circuit microfabrication techniques since the 1980s has led to significant development in MEMS, enabling a new class of chemical and biological sensors. Currently, the MEMs represent a diverse family of designs operating based on transduction of mechanical energy in the form of movement or deformation of micromachined parts to an electronic or optical readout reporting a change in the physical, chemical or biological environment.

One of the simplest MEMs is the microcantilever that operates similar to the atomic force microscope (AFM) by measuring deflection, resonance frequencies or

damping characteristics [121]. Bashir et al [122] reported a highly sensitive pH sensor by coating pH sensitive polymer consisting of poly(methacrylic acid) (PMAA) and poly(ethylene glycol) dimethacrylate on a microcantilever (see Figure 2-11a). Expansion of the polymer network when pH is increased above the pKa value of PMAA causes the microcantilever to bend due to surface stress with a maximum sensitivity of 1 nm/5 x 10^{-5} ΔpH. Poly(N-isopropylacrylamide) polymer brushes have also been grafted onto microcantilevers [123]. These brushes exhibit solvent dependent phase transition that cause changes in the surface stress of the cantilevers leading to deflections.

Another important class of MEMs used for chemical sensing is the piezoelectric mass resonant systems. Most of these sensors operate similarly to the QCM. Thin piezoelectric films generate acoustic waves whose wave propagation properties vary according to chemical/biochemical events on the surface. The output of these sensors is usually a shift in resonant frequency that provides a quantitative measurement of mass change on the sensor surface. An absolute mass change in the order of pg to fg has been reported with mass resolution of ng/cm^2 in liquid. Wohltjen et al reported a surface acoustic wave (SAW) device for detection of organic vapor using a sensitive polymer coating [124] (see Figure 2-11b). These SAW devices use interdigital transducer to generate and detect acoustic waves that are confined at the surface of the piezoelectric film to achieve high sensitivity [125].

a) b)

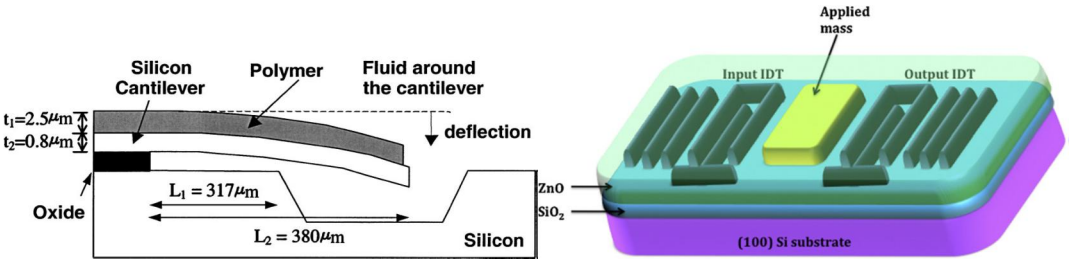

Figure 2-11: (a) Schematic of a microcantilever/polymer gel for pH sensing based on cantilever bending. Reprinted with permission from Ref [122, 125]. Copyright 2002, AIP Publishing LLC. (b) Schematic of a SAW device showing the piezoelectric film, interdigited transducers and sensitive polymer coating.*

2.5.3 Ion sensitive field effect transistors (ISFET)

Field effect transistor (FET), the basic building block of modern electronics has also been used for chemical sensing of charged analyte. A FET typically has 3 electrodes: gate, source and drain. A fixed voltage, V_{ds} is applied between the source and drain. A current, I_{DS} flows between the source and drain along a temporary channel consisting of charge carriers from the doped silicon substrate underneath. The gate potential, V_{gate} decides the charge carrier density that in turn modulates I_{DS} [126].

In chemical sensing FETs, the gate electrode is eliminated and replaced by a sensitive layer as seen in Figure 2-12. Binding of charged analyte modulates V_{gate} and thus I_{DS}. Sallacan et al coat an imprinted polymer on the gate surface of an ISFET for sensing of charged nucleotides [127].

*Reprinted from Biosensors and Bioelectronics, 33, Ioana Voiculescu, Anis Nurashikin, Acoustic wave based MEMS devices for biosensing applications, Pages 6, Copyright (2012), with permission from Elsevier.

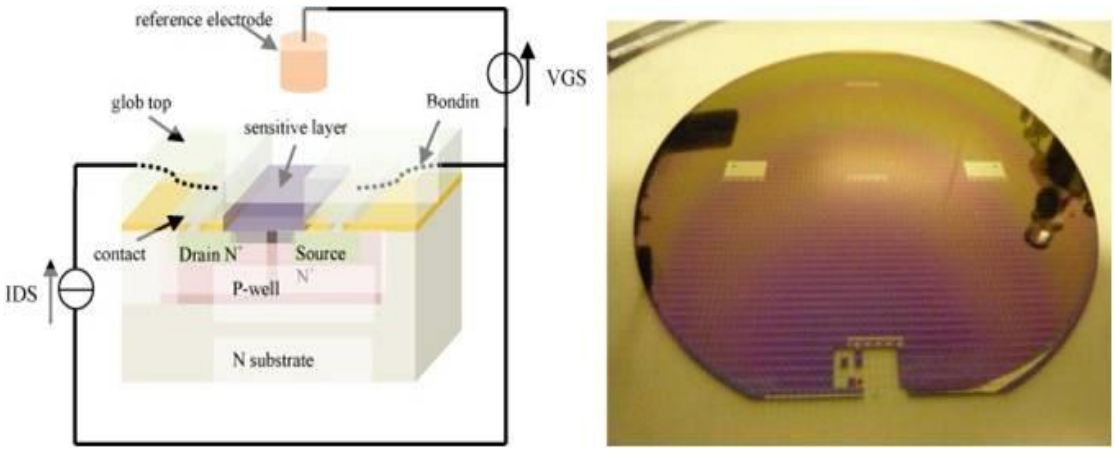

Figure 2-12: Illustration of a typical ion sensitive field effect transistor (left) and its mass production from a silicon wafer (right).*

2.5.4 SPR

The theory of SPR has been briefly described earlier. Gabai et al [128] demonstrated a glucose sensor based on an acrylamidophenylboronic acid-

acrylamide hydrogel film. The glucose sensitive film is coated onto an Au covered slide and studied using a commercial SPR Kretschmann type spectrometer. Glucose binding to boronic acid ligands leads to gel swelling that decreases the interfacial refractive index and resonant angle.

2.5.5 LSPR

LSPR has also been similarly applied to report refractive index change of responsive polymers in presence of stimuli. Gold nanoparticles are embedded in an imprinted poly(2-vinylpyridine) gel coated onto a gold nanoislands deposited glass slide for cholesterol sensing [129]. Binding of cholesterol increases refractive index and shifts the absorbance maximum as seen in Figure 2-13.

*Reprinted from Sensors and Actuator B: Chemical, 177, A. Cazale, W. Sant, Launay, F. Ginot, P. Temple Boyer, Study of field effect transistors for the sodium ion detection using fluoropolysiloxane-based sensitive layers, Page 516, Copyright (2013), with permission from Elsevier.

The LSPR has also been used to report analyte dependent volume change of responsive polymers. Here, the change in interparticle distance between embedded metal nanoparticles during volume change alters the LSPR [130].

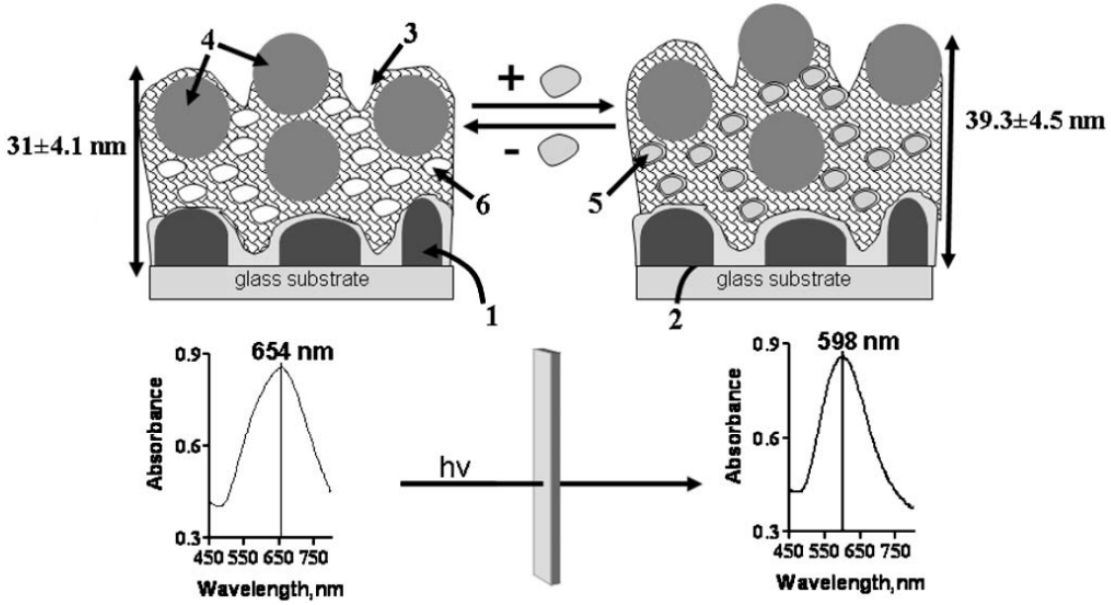

Figure 2-13: Schematics of a molecularly imprinted polymer sensor employing LSPR. Binding of analyte increases refractive index, thus shifting LSPR absorbance peak. Reproduced from Ref [129] with permission of The Royal Society of Chemistry.

2.5.6 Microlens

Liquid microlens integrated into a microfluidic system has been used to report polymer swelling behavior [131]. A ring-shaped pH sensitive acrylic acid gel exhibits swelling/deswelling in response to pH that changes the shape of the liquid meniscus at a water-oil interface that acts as a liquid microlens, changing its focal length in the process.

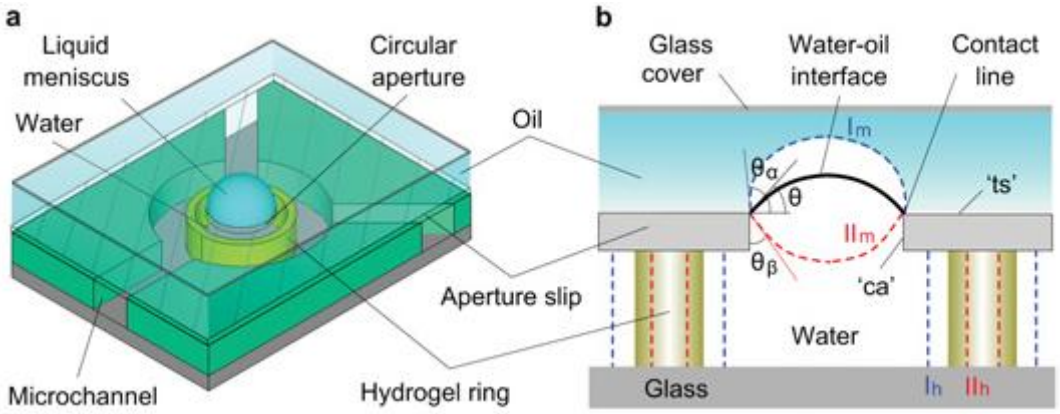

Figure 2-14: (a) Microlens sensor using a liquid microlens formed from water-oil interface. (b) Swelling and deswelling of the polymer gel regulates the shape of the liquid meniscus by changing angle θ of the pinned water-oil interface. Adapted by permission from Macmillan Publishers Ltd: Nature, Ref [131], copyright (2006)

2.5.7 Fabry Perot interferometry

The principles of the Fabry Perot interferometer has been introduced in §2.3.2.7 and was used by Tierney et al who formed a Fabry Perot etalon consisting pH-sensitive N-(3-dimethylaminopropyl)acrylamide gel at the distal end of an optical fiber [132] (see Figure 2-15). The pH dependent swelling/deswelling behavior leads to both a refractive index and volume change, resulting in a phase shift, Δθ corresponding to:

$$\Delta l_{opt} = \Delta\theta \frac{\lambda_o}{4\pi}$$

where λ_o is the center wavelength of the light source used and Δl_{opt} is the change in optical path length given by:

$$\Delta l_{opt} = \Delta l n_{gel} + l \Delta n_{gel}$$

where l and n_{gel} are the physical length and refractive index of the gel. The same group also uses the setup for an in-vivo glucose sensor based on a boronic acid

modified acrylamide gel [133]. However, the use of a relatively thick hydrogel film (50 -60 µm), required to observe the interference fringes within a reasonable bandwidth, may limit response time.

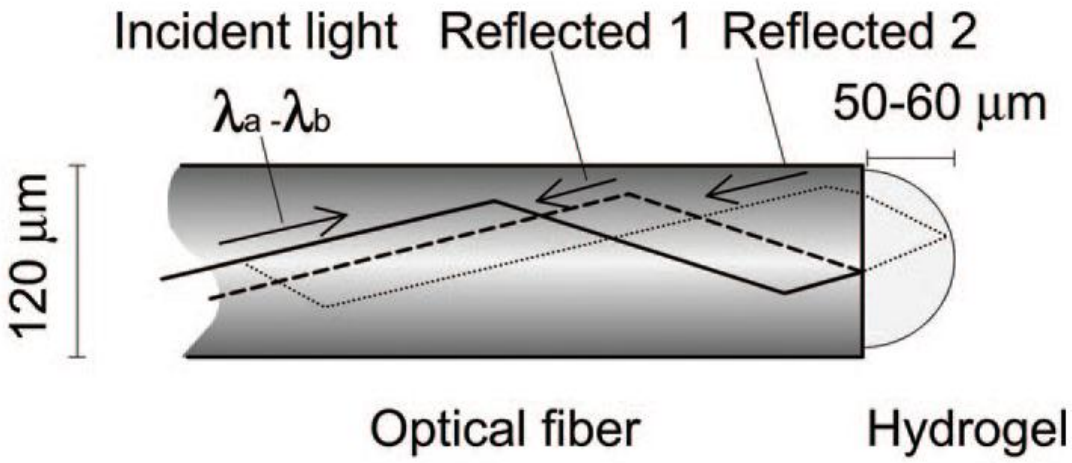

Figure 2-15: A Fabry Perot etalon formed from hydrogel at distal end of an optical fiber. Adapted with permission from Ref [132]. Copyright (2008) American Chemical Society.

2.5.8 Holographic grating

Responsive polymers have also been fashioned into holographic gratings using techniques like photolithography patterning [134], holographic lithography [135].

The gratings act like reflector of light of wavelength, λ_{max} dependent on the fringe separation, d as related by the Bragg equation:

$$\lambda_{max} = 2ndcos\theta$$

where n is the refractive index of the grating and θ is the incidence angle of light. Hence, any gel volume change in response to stimuli will alter fringe spacing and transduced into a shift in spectral peak (see Figure 2-16).

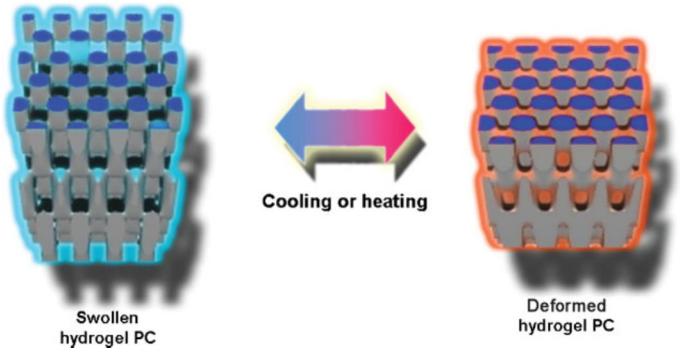

Figure 2-16: Hydrogel halographic grating. Vicoelastic deformation during temperature increase or decrease change interlayer spacing in the [111] direction. Reproduced with permission from Ref [135135].

2.5.9 Photonic crystal

The photonic crystal colloidal array (PCCA) technology was pioneered by Asher et al [136]. It involves the embedding of a highly organized array of colloidal particles in a responsive polymer gel that Bragg diffracts light (see Figure 2-17). Volume change in the responsive gel changes the intercolloidal distance and alters the diffraction spectra. The group has successfully used the technology for sensing pH [137], ammonia [138], glucose [139] and heavy metal cations [140]. The technology provides direct detection through an observable colour change but response time is often slow (~30 min).

2.6 Chapter conclusion

The basic components and principles of a FOCS are introduced along with the advantages of an optical fiber based sensor. A wide range of optical techniques broadly classified as direct or indirect can be implemented.

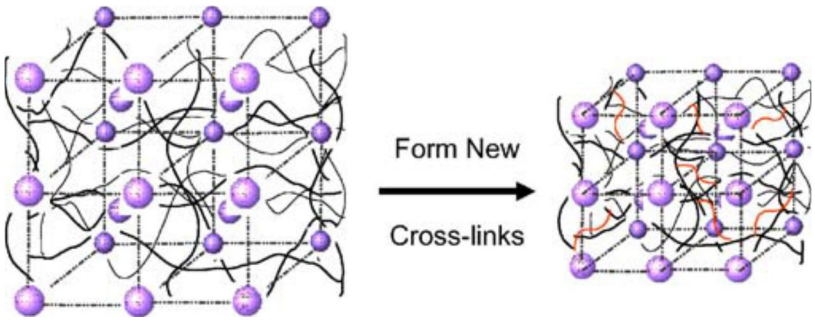

Figure 2-17: PCCA showing increased cross linking in presence of analyte. The spacing between diffracting planes in the PCCA decreases, causing diffracted light to blue-shift. Reproduced from Ref [138]. Springer and Analytical and Bioanalytical Chemistry, 385, 2006, Page 680, Progress toward the development of a point-of-care photonic crystal ammonia sensor, Kyle W. Kimble, Figure 2, with kind permission from Springer Science and Business Media.

The majority of indirect sensors utilise the evanescent field of guided modes at the core-cladding interface to probe fluorophores/ colormetric/ luminescent reagents that report presence of an analyte by a change in fluorescence or absorbance in a technique known as evanescence field spectroscopy. These optical intensity based techniques require a stable light source and may suffer inaccuracies arising from photobleaching, background fluorescence, fluorophore leeching, etc, thus requiring special measurement techniques like ratiometric measurement, fluorescence lifetime and phase measurements which may not always be feasible or involve additional instrumentation.

Meanwhile, responsive polymers that change its physio-chemical properties in response to a physical or chemical stimulus have been an area of immense research and development. Various transducers using responsive polymers as the sensing component have been reported in literature and reviewed here. Whilst many transducer systems are available, they usually require expensive equipment or tedious and costly fabrication processes. QCM, MEMs and ISFET require costly

fabrication in a foundry involving complex mask fabrication, lithography and etching. While holographic grating and PCCA techniques are considerably cheaper, they have thus for been limited to discrete measurements. The PCCA has a slow response time arising from the relatively thick hydrogel materials and thus is incapable of real time measurements.

Hence, it is proposed here that a fiber optic platform may be a suitable transducer for responsive polymers based sensing. The merging of these 2 technologies will reap many benefits including the increase in sensing possibilities of fiber optic sensors and enabling a sensor device that is miniature in size, low cost, robust, and capable of real time and multiplex sensing.

Two optical techniques have been identified for responsive polymer based sensing: LSPR and interferometry. The following chapter reports a novel fiber configuration for LSPR sensing in preparation for a fiber optic LSPR pH sensor in Chapter 4.

Chapter 3

Fiber Optic Refractometer based on Cladding Excitation of Localized Surface Plasmon Resonance*

3.1 Introduction

The phenomenon of SPR which is the collective oscillation of free electrons at a metal-dielectric interface in response to electromagnetic radiation fitting the resonant conditions has been introduced in §2.3.2.5. Since its first demonstration for biomolecular detection [141], SPR has received tremendous research interest owing to its potential for label-free detection in real time and has since been successfully commercialized [142].

However, the basic SPR setup requires a light source of well-defined polarization and incidence angle and bulky optical components like a prism to excite SPR and photodiode arrays to accurately determine resonant position, leading to costly instrumentation with limited point-of-care applications [143].

More recently, LSPR observed in certain metal nanostructures have been investigated for sensing applications. Similar to SPR, LSPR is sensitive to the local dielectric environment but eliminates the geometric and polarization requirements of SPR and allows direct transmission detection. In addition, the LSPR is tunable

over a wide wavelength range by controlling the nanostructure's composition, size, shape and interaction [144], thus opening the possibility for multiplex sensing [145]. The electromagnetic field enhancement at the metal nanostructure's surface also allows simultaneous measurement of surface-enhanced Raman spectroscopy (SERS).

Several optical fiber based LSPR sensor have been reported to take advantage of the miniature size, ruggedness, inertness of optical fibers for sensing of biological and chemical species like proteins [146, 147, 148, 149, 150, 151], heavy metal ions [152, 153, 154]. Figure 3-1 illustrates the reported fiber optic configurations used for LSPR sensing.

In most of these works, the cladding of a fiber segment is removed in order to access the evanescent field of guided modes within the fiber core that excites LSPR in immobilised gold nanoparticles on the fiber surface. Chemical etching using hazardous hydrofluoric acid is most commonly used for cladding removal and often, the transmittance or reflectance have to be monitored during the etching process to determine the extent of cladding removal. The removal of cladding compromises the structural integrity of the fiber sensor (see Figure 3-1a).

Chen et al [155] uses a femtolaser to micromachine a U-shape trench on an optical fiber that exposes the fiber core (see Figure 3-1c). However, the reported sensor has modest sensitivity to refractive index (LOD 1.06 x 10^{-3} RIU) and uses costly femtolaser for fabrication.

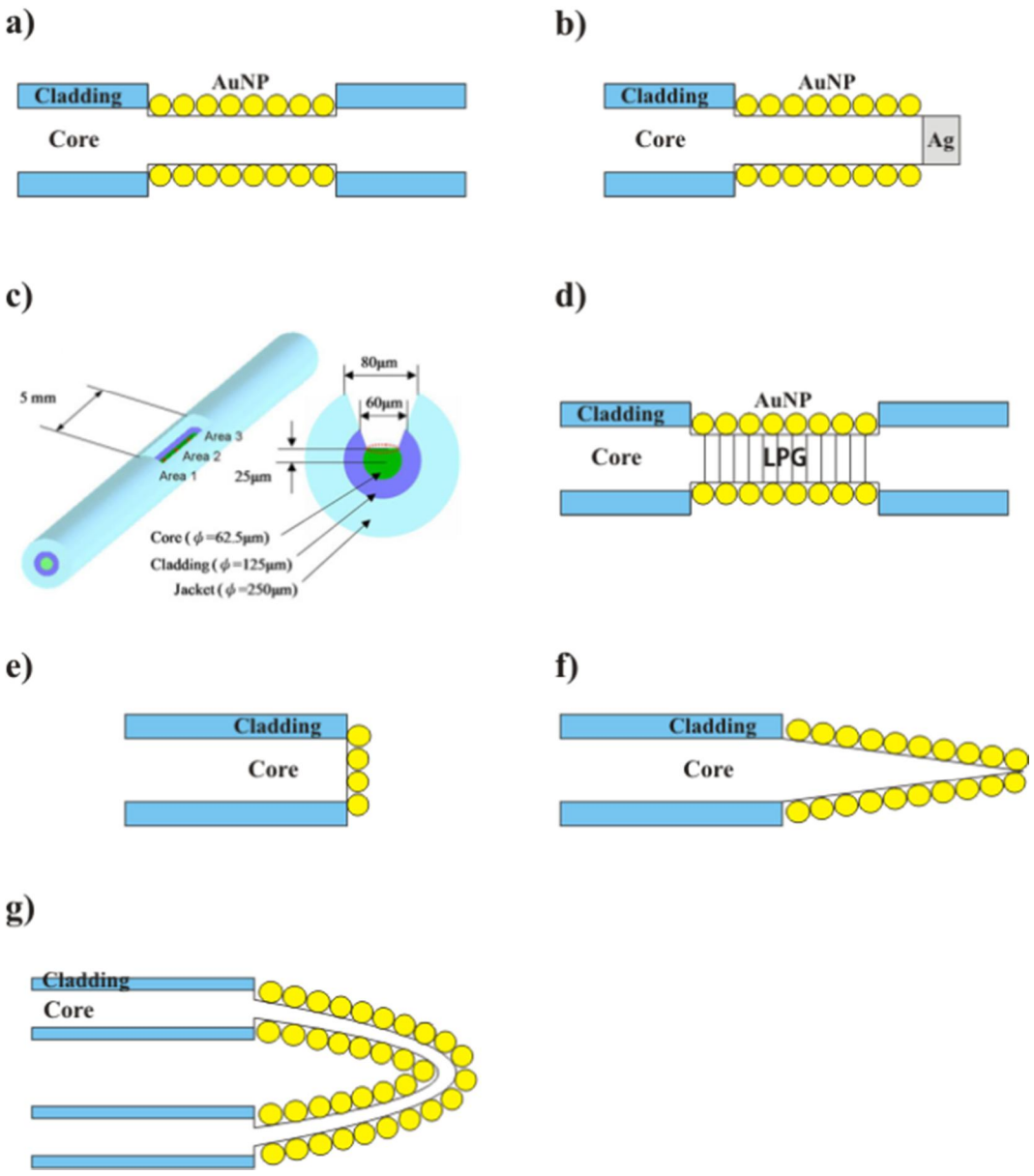

Figure 3-1: Illustration of reported fiber optic configurations for LSPR sensing. a) Transmission, Ref [149], b) reflection, Ref [152], c) U-shape trench, Ref [155]*, d) LPG, Ref [156], e) end-face coated, Ref [148], f) tapered tip, Ref [157], g) U-shape bend, Ref [150].

*Springer and Microsystem Technologies, 16(7), 2009, Page 1212, Novel U-shape gold nanoparticles-modified optical fiber for localized plasmon resonance chemical sensing, Chien-Hsing Chen, Figure 7a, with kind permission from Springer Science and Business Media.

Gold colloid is coated onto a LPG by Tang et al [156] (see Figure 3-1d). Cladding removal is necessary to improve sensitivity and the LPG suffers from cross sensitivity to temperature. Fiber tapering [157] and bending to form a U-shape [150] (see Figure 3-1f and 3-1g respectively) have been reported but it is unlikely to obtain uniform and reproducible structures without automation and large optical losses are expected.

In this chapter, a novel fiber configuration that employs photonic crystal fiber (PCF) for the excitation of LSPR of AuNPs coated directly onto the fiber surface is presented. The cladding modes are used to excite LSPR instead of core modes, offering tremendous improvement in ease of fabrication.

The fabrication of the sensor and its characterization with respect to its sensitivity to refractive index changes are detailed in §3.2 and §3.3. The results pave the way for an fiber optic pH sensor based on LSPR in Chapter 4.

3.2 Materials and methods

3.2.1 Materials

Optical fibers including multimode fiber (62.5/125 μm) (MMF) and PCF (10.1/125 μm LMA-10) are purchased from Corning and NKT Photonics respectively.

Chlorauric acid ($HAuCl_4$. $3H_2O$) and sodium citrate (citric acid, trisodium salt 98%) are purchased from Acros. Sulfuric acid (95-97%) and hydrogen peroxide (30%) are from Merck and VWR respectively. Hydrochloric acid (≥ 37%) and nitric acid (70%) are from Sigma-Aldrich.

All reagents are of analytical grade and solutions are prepared using ultrapure water with resistivity 18.2 MΩ cm from Milli-Q system.

3.2.2 Methods

3.2.2.1 Preparation of fiber sensor

LMA-10 is a PCF in which light is confined within a 10.1 μm solid core via air holes arranged in a regular hexagonal lattice around the core. The mode field diameter is 8.4 μm for light with 532 nm wavelength and is designed to operate in single-mode at all wavelengths with low fiber loss [158].

A segment of LMA-10 is stripped of its acrylate jacket and fusion spliced in between MMF using an electric arc splicer (Type 39, Sumitomo). All fiber ends are stripped of the acrylate jacket and wiped with ethanol to remove any debris prior to cleaving with a precision fiber cleaver (Fujikura, CT-30).

The arc splicer is operated in the manual mode and fiber ends are aligned based on their edge. An electric arc is applied to melt the fiber ends while simultaneously pushing the fibers towards one another. Repeat arcs are added to collapse the air holes at the splice intersection.

3.2.2.2 Synthesis of gold nanoparticles

AuNPs are prepared using Turkevitch's method of citrate reduction of aqueous chlorauric acid [159]. All glassware used in the synthesis of AuNPs is treated with aqua regia (nitric acid and hydrochloric acid in 1:3 volume ratio) prior to use to dissolve any gold that may serve as nucleation sites. 50 ml of 0.4 mM aqueous chlorauric acid is brought to a boil under constant vigorous stirring to avoid temperature inhomogeneity. 0.5 ml of preheated 0.08 M sodium tricitrate is added

and the solution is left to boil for a further 10 mins during which a red colloidal solution is obtained.

3.2.2.3 Immobilization of AuNPs on fiber

The PCF segment of the sensor is treated in Piranha solution consisting 70 % v/v concentrated sulphuric acid and 30 % v/v hydrogen peroxide at 80 ^{o}C for 30 mins to increase surface density of hydroxyl groups prior to silanization in 5 % v/v (3-aminopropyl)trimethoxysilane (97 %, Aldrich) in methanol (Merck) for 4 hours. The fiber is rinsed thoroughly with methanol and placed in 120 ^{o}C oven to activate the silanization process. AuNPs are immobilized on the fiber surface via a 5 min immersion in gold colloid after the fiber has cooled.

3.2.2.4 Field emission scanning electron microscope (FESEM)

The AuNPs coated fiber is viewed using FESEM (JSM-6700F, Jeol) after sputtering with a fine layer of Palladium.

3.2.2.5 UV-Vis spectroscopy

The UV-Vis spectrum of the AuNPs colloid is determined using Shimadzu UV-Vis spectrometer, UV-2450.

3.2.2.6 Experimental setup for determining sensitivity to refractive index

One end of the fiber sensor is coupled to white light source (Yokogawa, AQ4305) and the transmitted light at the other end is measured by fiber spectrometer (Ocean Optics, USB4000) (see Figure 3-2). Since the fibers' diameter comply with telecommunication standard, bare fiber adapters (Bullet) can be used for coupling to light source and spectrometer without need for tedious optical alignment. A laptop

running SpectraSuite (Ocean Optics) is used for data collection and further processing and plotting of data is carried out using OriginPro 8 (OriginLab Corporation, USA).

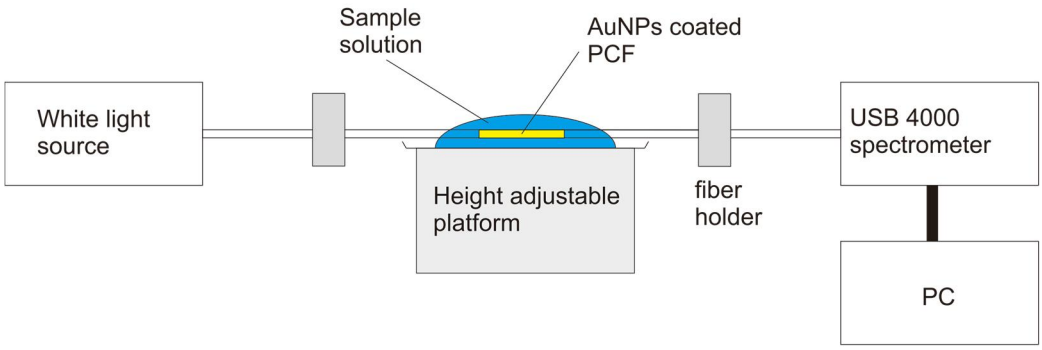

Figure 3-2: Illustration of experimental setup for proposed fiber LSPR refractometer.

3.3 Results and discussion

3.3.1 Characterization of AuNPs

Figure 3-3a shows the UV-Vis spectra of the synthesized AuNP colloid and AuNPs immobilised on the fiber LSPR sensor. The AuNP colloid exhibits a distinctive LSPR absorbance peak at 523.8 nm. This is fitted with theoretical calculation from the multipole scattering theory [160] that established relations between observed absorption, A with the extinction cross section (σ_{ext}):

$$A = \frac{\sigma_{ext} d_0 N}{2.303}$$

where d_0 and N are the path length of the spectrometer and number density of AuNPs per unit volume respectively. σ_{ext} of a spherical particle with radius R in a medium of dielectric function, ϵ_m at wavelength, λ is given by [161]:

$$\sigma_{ext} = \frac{2\pi}{|k|^2}\sum(2L+1)Re(a_L + b_{L)}$$

where wave vector, k is given by:

$$k = \frac{2\pi\sqrt{\epsilon_m}}{\lambda}$$

$a_L(R, \lambda)$ and $b_L(R, \lambda)$ are the scattering coefficients in terms of Ricatti-Bessel functions ($\eta_L(x)$ and $\psi_L(x)$):

$$a_L = \frac{m\psi_L(mx)\psi_L^{'}(x) - \psi_L^{'}(mx)\psi_L(x)}{m\psi_L(mx)\eta_L^{'}(x) - \psi_L^{'}(mx)\eta_L(x)}$$

$$b_L = \frac{\psi_L(mx)\psi_L^{'}(x) - m\psi_L^{'}(mx)\psi_L(x)}{\psi_L(mx)\eta_L^{'}(x) - m\psi_L^{'}(mx)\eta_L(x)}$$

where size parameter $x = kR$, $m = n/n_m$, n is the complex refractive index of the particle and n_m is the real refractive index of the medium surrounding the particle. For small particles (x<<<1), only the first electric dipole term (L = 1) suffice.

An algorithm provided in Ref [160] is used to calculate extinction efficiency of the AuNPs, Q_{ext} using n_m (1.333), Au plasma frequency (138 x 10^{14} Hz), Au collision frequency (0.333 x 10^{14} Hz), Au Fermi velocity (1.4 x 10^8 cm/s) and complex refractive index of bulk Au given in Ref [162]. The absorbance, A is calculated from earlier equation using the relationship, $Q_{ext} = \pi R^2 \sigma_{ext}$, d_0 = 1 cm and N is derived from Ref [160]. The calculated AuNPs diameter is derived from R that gives A that best

fits the empirical derived absorbance spectrum and this corresponds to a diameter of 19.5 nm.

The AuNPs are viewed using FESEM (see Figure 3-3b) and the images are processed using ImageJ to obtain particle size. The average diameter of 100 AuNPs measured is 19.3 nm with a 5.02% standard deviation. This is in close agreement with theoretical calculations and indicates the AuNPs are fairly monodispersed.

Owning to citrate's role as both a reducing agent and an electrostatic stabilizer, the size of the AuNPs can be controlled by the citrate to chlorauric acid mole ratio in the precolloidal solution. Smaller AuNPs results from a higher citrate to chlorauric acid mole ratio [163].

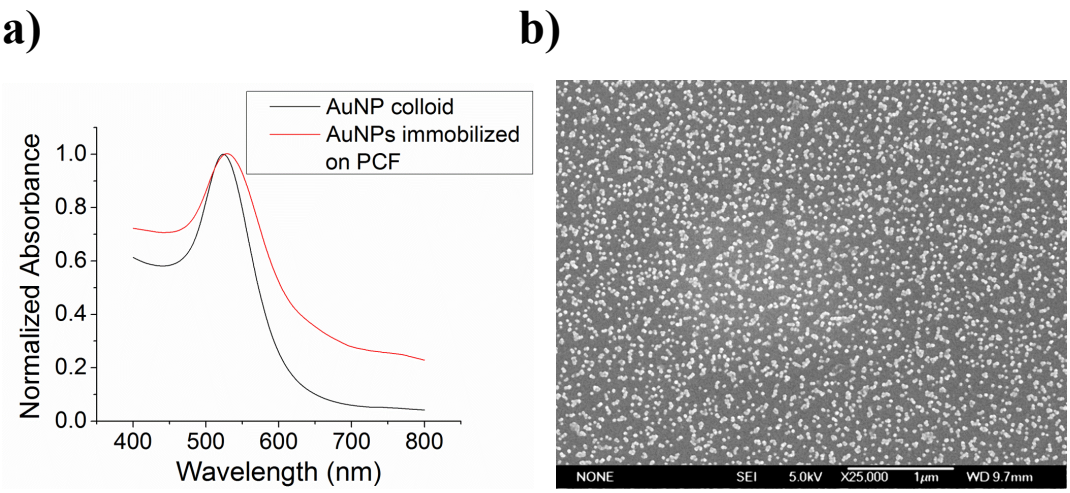

Figure 3-3: (a) Normalized absorbance spectra of AuNPs colloid and AuNPs immobilized on PCF. (b) FESEM micrograph of AuNPs electrostatically immobilized on PCF.

3.3.2 Electrostatic immobilization of AuNPs

The AuNPs obtained from citrate reduction are negatively charged and bind electrostatically to the positively charged amino terminated fiber surface. The LSPR peak of the fiber bounded AuNPs red shifts by 5 nm as seen in Figure 3-3a as a result of plasmonic coupling due to reduced inter particle distance. Broadening of the LSPR peak can be attributed to the non-perfect spherical structure of the AuNPs and their varying orientation on the fiber may have induced various plasmon modes. The surface coverage of AuNPs on the fiber defined as the ratio of surface area of AuNPs on the fiber to surface area of entire fiber is found by first converting the FESEM micrograph to binary image using an appropriate threshold and taking the ratio of the respective pixel count. The surface coverage was determined to be approximately 21.2 %. Slight aggregation of AuNPs can be observed.

3.3.3 Principles of operation of fiber refractometer

The proposed fiber sensor uses the evanescent field of cladding modes for excitation of LSPR in immobilised AuNPs on the surface, circumventing the need for tedious and hazardous chemical etching of cladding common in reported fiber LSPR sensors. By making use of PCF's unique optical property to guide light with a cladding comprised of a regular array of air holes, a strategy of mode splitting and recoupling between core and cladding modes by selective collapsing of the air holes has previously been reported for fiber intermodal interferometers [202]. The method is adapted here for LSPR based sensing.

As light is confined within the regular array of air holes in a PCF, there is loss of confinement of light in the collapsed region. Light propagating within the multimode

core of MMF diffracts and broadens as it transverses the collapsed region, exciting both the cladding and core modes within the PCF (see Figure 3-4a).

The evanescent field of the cladding modes penetrates into the exterior and excites LSPR in the immobilized AuNPs when frequency is resonant with collective oscillation of conduction electrons within the AuNPs. For spherical particles with diameter much smaller than the wavelength of the excitation light which is the case here, the LSPR can be viewed as dipolar, with resonance occurring at a specific frequency. The second collapsed region serves to couple the PCF cladding modes back into the MMF core and to the spectrometer. The polarizability of the AuNPs is enhanced at LSPR, leading to enhanced light scattering and absorption of the evanescent field, reducing transmitted light intensity (increased absorbance) (see Figure 3-3a).

The length of the collapsed region along the PCF is measured to be around 135 μm when viewed under microscope (Olympus, BX51) (see Figure 3-4b). The insertion loss for a 10 mm PCF measured using a 635 nm bench top laser (Photonik) and photodetector (New Focus, Model 2011) is 5 to 7 dB in ambient air which is lower than reflectance at a silica-air interface (typically 4%).

a)

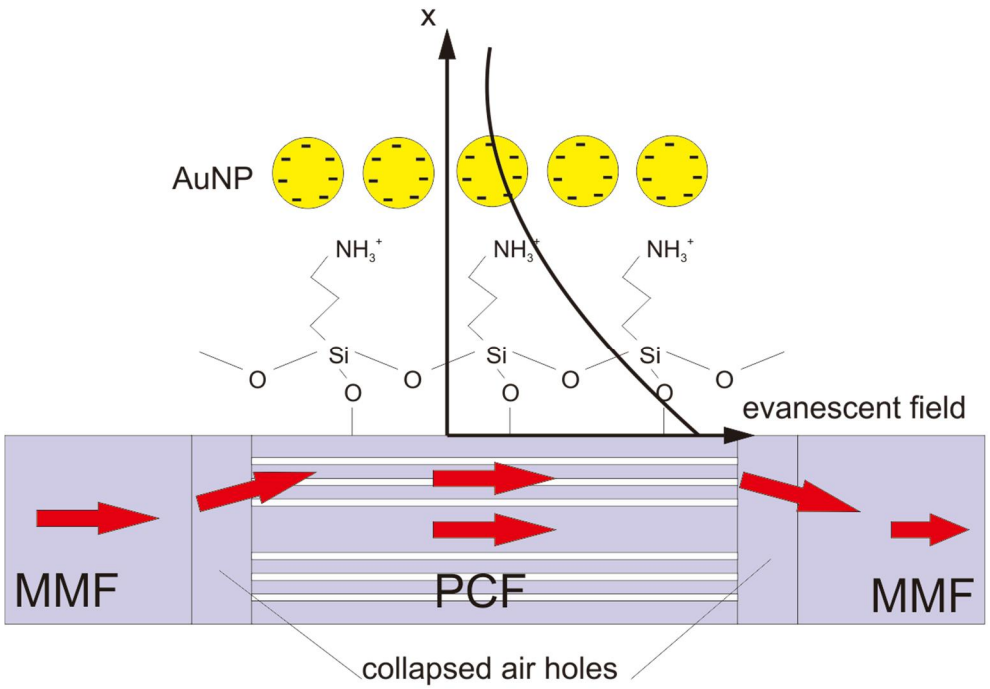

b)

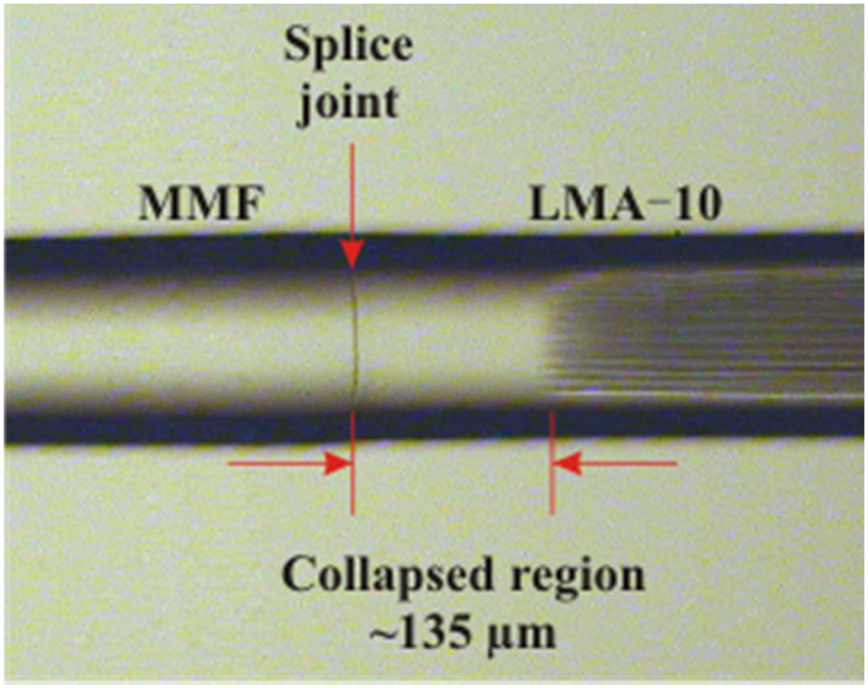

Figure 3-4: (a) Excitation of LSPR in AuNPs electrostatically immobilized on surface by evanescent field of cladding modes in PCF. (b) Micrograph of splice intersection between MMF and PCF showing the collapsed air holes.

3.3.4 Sensitivity to refractive index

The transmission spectrum of the uncoated fiber is collected prior to immersion in AuNP colloid and used as reference, I_{ref}, in the calculation of absorbance ($-\log_{10}(I/I_{ref})$) of the sensor in varying refractive index solutions. Sucrose solutions of various concentrations are used as standards to calibrate the sensor using the setup in Figure 3-2. The refractive indices of the sucrose solutions are predetermined at room temperature using a portable electronic refractometer (Atago, PAL-RI) accurate to 0.0001 RIU. In between measurements, the sensor is rinsed with distilled water prior to the next measurement. The absorbance spectra are digitally filtered using a Savitzky-Golay filter and the LSPR peak determined via the peak analyzer function in OriginPro. The peak shift with respect to the AuNPs coated fiber in distilled water, $\Delta\lambda_{max}$, is plotted against refractive index in Figure 3-5 with the corresponding absorbance spectra at different refractive indices across the range of sucrose solutions.

The LSPR absorbance peaks shifts towards longer wavelengths (red-shifts) as the external refractive index increases. The points can be fitted with a linear line with squared correlation coefficient value, $R^2 = 0.9967$. The sensitivity of the LSPR sensor is given by the slope of the linear regression and determined to be 67.0 nm/RIU. Taking into consideration only the spectral resolution of the spectrometer (i.e. 0.2 nm), the limit of detection is 2.99×10^{-3} RIU.

a)

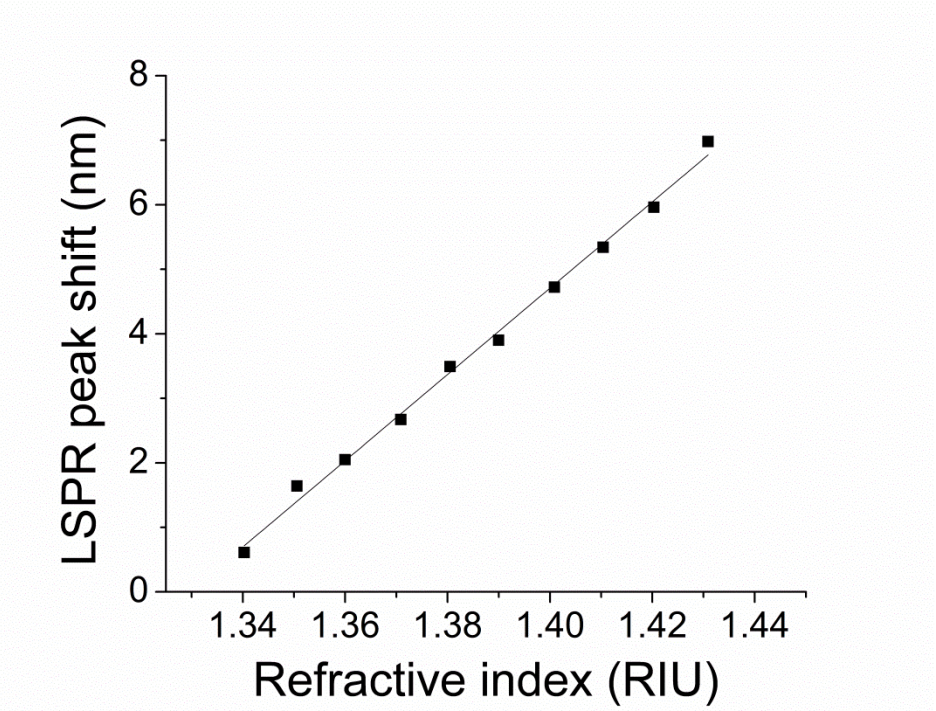

b)

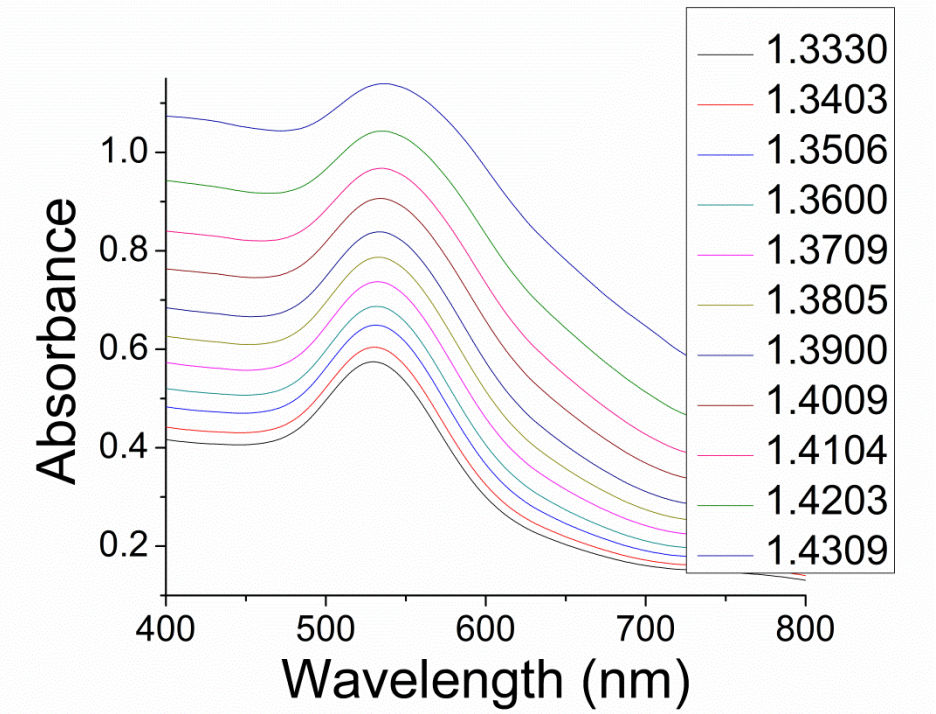

Figure 3-5: (a) Plot of LSPR absorbance peak shift versus external bulk refractive index. The points can be linearly fitted with slope, 67.0 nm/RIU and R^2 = 0.9967. (b) Corresponding absorbance spectra at various refractive indices.

The response of the LSPR sensor with refractive index was also characterized by the change in normalized transmitted intensity, I_{norm}, at a specific wavelength. The transmitted intensities at various refractive indices were normalized with respect to intensity of the AuNPs coated sensor in distilled water (RI = 1.3330 RIU). Figure 3-6 shows the plot of normalized intensity versus refractive indices at wavelength, λ = 525.02 nm for the fiber prior and after AuNPs coating.

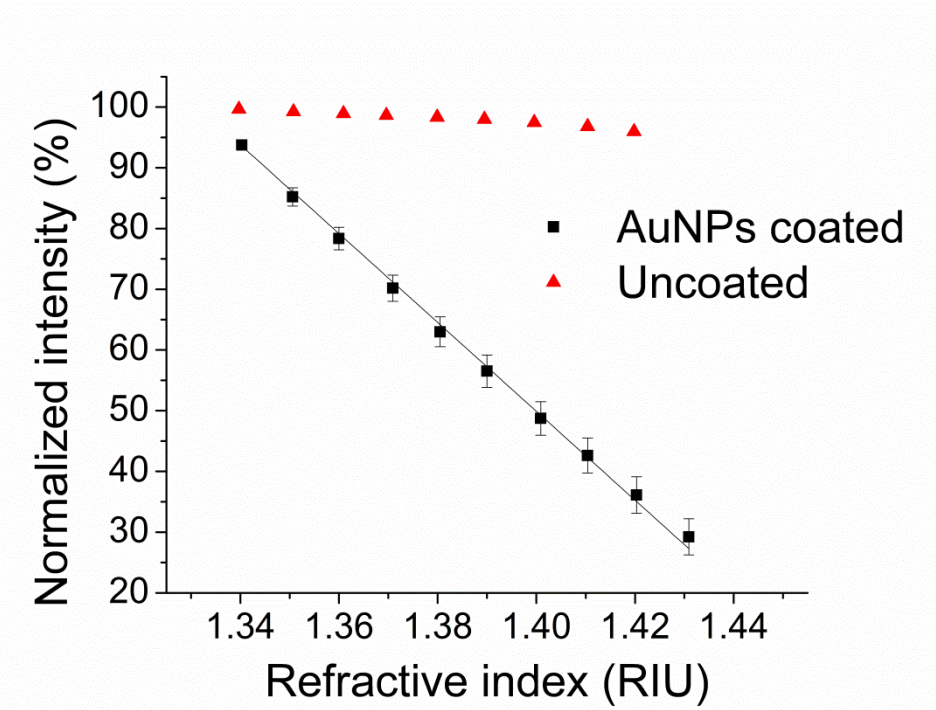

Figure 3-6: Plot of normalized transmitted intensity versus external bulk refractive index at wavelength, λ = 525.02 nm for AuNPs coated and uncoated fibers. The points for the former can be linearly fitted with slope, -731 %/RIU and R^2 = 0.9988.

Prior to AuNPs coating, the normalized transmission light intensity changes from 99.6 % to 96.0 % when refractive index is changed from 1.3397 RIU to 1.4198 RIU. The normalized transmission intensity decreases with increase in external refractive index due to decreasing refractive index difference between the cladding and external since the cladding modes propagate via Fresnel reflections off the cladding-

external interface. More significant change in transmitted power can be expected when external refractive index approaches that of the PCF cladding.

A much steeper decrease in normalized transmitted intensity can be observed for AuNPs coated fibers in Figure 3-6. The error bars corresponds to standard deviation in performance of 3 separate LSPR fiber sensors prepared similarly. Sensitivity, given by the slope of the linear regression line is -731 %/RIU with $R^2 = 0.9988$. The limit of detection, (LOD), defined as the smallest measurable absolute refractive index change, is calculated from the ratio of sensitivity over 3σ, where σ is the standard deviation of 5 normalized intensity readings at RI = 1.4309 RIU which has the worst signal-to-noise-ratio and is determined to be 1.76×10^{-5} RIU.

Two methods for characterizing sensor response to external refractive indices have been used. Monitoring of absorbance peak shifts returns a fairly poor sensitivity and limit of detection. This is in part due to the poor resolution of the spectrometer and the broad LSPR peak. By normalizing transmission intensity at a single wavelength in the second method, a simplified experiment setup using low cost light emitting diode (LED) and photodiode could be used. The sensitivity of the LSPR sensor inevitably depends on characteristics of the immobilized AuNPs. Various parameters like AuNPs diameter, surface density, coating temperature, coating time have been reported to affect overall sensitivity [149, 164], thus it is difficult to compare the performance of current work with those reported. The sensitivity and limit of detection obtained from the wavelength shift interrogation methods fairs poorly compared to those reported in part due to lower surface density used in this work. Lee *et al.* [149] reported an increase in sensitivity with increased surface density up to 60 % coverage for 60 nm diameter AuNPs and Tu *et al.* [164] obtained higher sensitivity using similarly sized AuNPs but at almost twice the

surface density used in this work. The surface density of the immobilized AuNPs can be increased by increasing coating time, but, nevertheless, we have found the repeatability of sensor performance to degrade when coating time is increased. This may be attributed to the uncontrollable aggregation of AuNPs. The performance of the sensor using normalized intensity interrogation compares favorably with Shao's work [147] which uses similarly sized AuNPs (-594%/RIU) and has an order of magnitude better LOD than Ref [152, 153, 154, 155]. The sensor also exhibits good linearity over RI range 1.33 RIU to 1.43 RIU which is of biological and chemical sensing importance.

3.4 Chapter conclusions

An optical fiber refractometer based on cladding mode excitation of surface immobilized AuNPs has been demonstrated. Simple splicing and chemical surface modification are used to fabricate the sensor, eradicating the need for cladding removal using chemical etching that is both hazardous and compromises mechanical integrity of the sensor. The LSPR sensor exhibits good linearity (R^2 = 0.9988) in normalized transmitted intensity with high sensitivity of -731 %/RIU in response to external bulk refractive index change in the region 1.33 RIU to 1.43 RIU with a limit of detection of 1.76 x 10^{-5} RIU and is highly reproducible, making it useful for biological and chemical sensing applications.

The reported sensor serves as platform for a pH sensor in the next chapter by embedding AuNPs within a pH sensitive polymer structure realised using the layer-by-layer technique.

Chapter 4

Fiber optic pH sensor based on gold nanoparticles embedded polyelectrolyte multilayers*

4.1 Introduction

Chapter 3 reports a novel fiber configuration for LSPR-based sensing. The evanescent field of cladding modes propagating along a PCF is used to excite LSPR of immobilised AuNPs on the surface. The sensor boosts facile fabrication with improved sensitivity over reported fiber sensors that rely on core mode excitation. In this chapter, the sensor is applied for pH sensing by embedding AuNPs within a pH sensitive polyelectrolyte multilayers formed by the layer-by-layer (LBL) technique on the fiber surface.

pH, a measure of acidity or basicity of a solution, is defined as the decimal logarithm of the hydronium activity in the solution:

$$pH = -log_{10}\alpha(H_3O^+)$$

where $\alpha(H_3O^+)$ is the activity of hydronium which can be equated to the concentration of hydronium if concentration is low.

The pH is an important biochemical parameter as seen in its strict regulation within a narrow range in the body. Almost all proteins depend on pH to maintain its structure and function, thus changes in pH regulate many metabolic reactions, and subsequently cellular behaviour like proliferation, migration and transformation [165]. In chemical process manufacturing, the pH of the reaction is buffered at the optimal pH to maximise yield. Hence, the monitoring of pH is of upmost relevance in many scientific research and practical applications, driving the development of pH sensors [166,167, 214].

The glass electrode pH meter is the most common device used for pH measurements. It consists a glass bulb membrane that separates an internal solution and a silver/silver chloride electrode from the solution whose pH is being measured. The pH meter measures the potential difference across the glass membrane obtained from an inner solution electrode and a reference electrode (shown in Figure 4-1 for a combination design pH electrode). The thin glass membrane made from amorphous silicon dioxide has embedded oxides of alkali metals that undergoes ion exchange with hydronium in the sampled solution, establishing a potential difference at the glass membrane/solution interface, $E_{glass|solution}$ (derived from the Nernst equation) [168]:

$$E_{glass|solution} = \frac{RT}{2.303F} log\alpha(H_3O^+) = -\frac{RT}{2.303F} pH$$

where *R* is the molar gas constant, *T* is the temperature in Kelvins, *F* is the Faraday constant and $\alpha(H_3O^+)$ is the activity of hydronium. The internal solution is sealed and has a fairly constant pH, keeping the inner potential unchanged. Hence any changes in potential difference arise due to pH change of the sample solution.

The glass electrode pH meter suffers from many drawbacks like the fragility and bulkiness of the glass membrane bulb, the need for constant recalibration as the glass membrane ages, thus limiting its effectiveness in pH measurement of small volume samples or when continuous pH measurements is required. This has spurred development in alternative pH sensors.

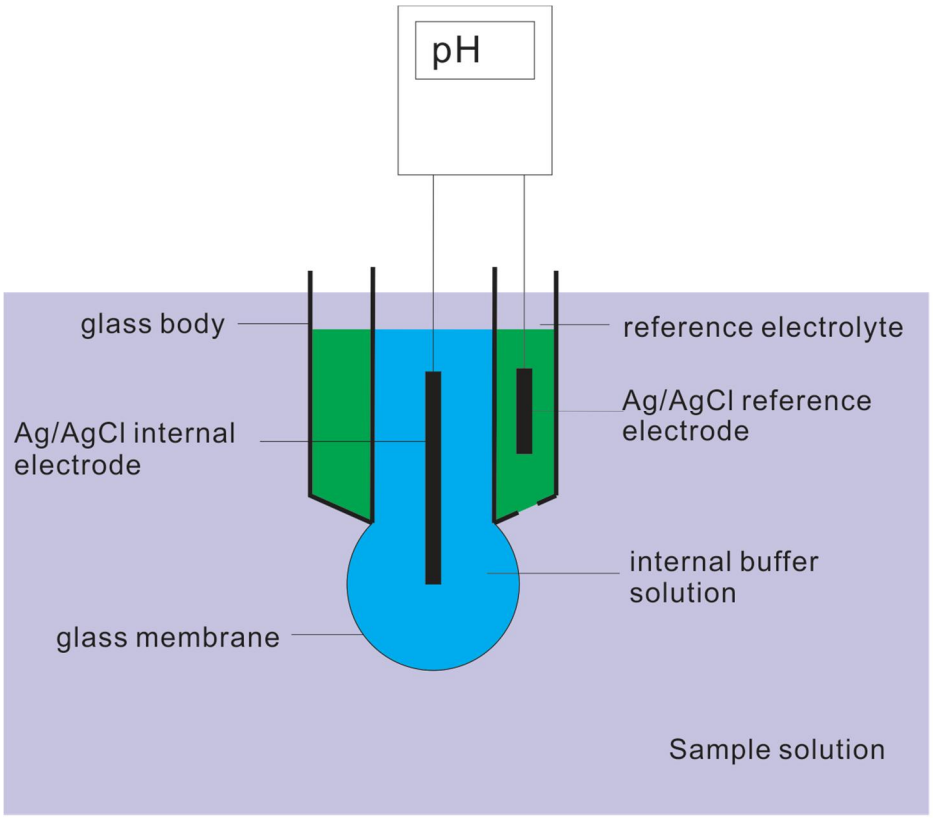

Figure 4-1: Illustration of a combination glass electrode pH meter.

Fiber optic pH sensors have emerged as a promising device owing to its use of electromagnetic radiation instead of electrical potential for measurement which enhances the safety aspect for in vivo applications and make it relatively free from electromagnetic interference. In addition, fiber optics can be easily miniaturized and implemented as a probe based platform which facilitates insertion into the body through a catheter. It is also potentially more stable than electrode based devices as it does not require maintenance of a reference electrode potential [169]. Numerous

fiber optic pH sensors have been developed and have been comprehensively reviewed in Ref [166,170].

The overwhelming majority of the developed fiber optic pH sensor utilizes pH sensitive dyes immobilized within a sensing film either on the distal end or unclad portion of an optical fiber. The pH sensitive dye is a weak acid or base with distinct optical spectral properties dependent upon its protonation state that is in turn determined by the local pH environment. Measurement of absorption [171] or fluorescence [172] of these dyes is the basis of fiber optics pH sensor. However, the absorption method is less sensitive and the fluorescence method requires the use of dyes with large Stoke's shift and filtering to avoid interference from the excitation source. The measurement of fluorescence lifetime though less sensitive to excitation light fluctuations and dye leeching requires more sophisticated setup including a pulse light source and high bandwidth photoreceiver and post processing circuitry in order to demodulate fluorescence lifetimes which may be less than 10 ns [173].

In this chapter, a fiber optic pH sensor based on AuNPs incorporated within a pH responsive polyelectrolyte multilayers (PEM) is demonstrated. The LSPR effect exhibited by the AuNPs is free from photobleaching commonly suffered by fluorophores and is proven to be highly sensitive in many sensing applications [174, 175]. The pH responsive material is coated onto PCF to allow excitation of the AuNPs by evanescent field of cladding modes. Properties of the PEM including number of layers and AuNPs loading are studied to optimize sensitivity. Lastly, an alternative reflection configuration is proposed by coating on the distal end of the optical fiber.

4.2 Materials and method

4.2.1 Materials

Optical fibers including multimode fiber (MMF, 62.5/125 μm) and PCF (10.1/125 μm LMA-10) are purchased from Corning and NKT Photonics respectively.

Chitosan with Mw ~ 140,000 to 220,000 and degree of acetylation ≤ 40 mole%, poly(sodium 4-styrenesulfonate) (PSS) with Mw ~70,000, sodium tetraborate (99%), sodium borohydride are obtained from Aldrich. Hydrochloric acid (37%), sulfuric acid (95-97%) and acetic acid (glacial) are procured from Merck while hydrogen peroxide (30%) is from VWR and hydrogen tetrachloroaurate (III) trihydrate from Alfa Aesar. Nitric acid (min 69%) is from Honeywell.

All reagents are of analytical grade and solutions are prepared using ultrapure water with resistivity 18.2 MΩ cm from Milli-Q system.

4.2.2 Method

4.2.2.1 Preparation of fiber sensor

The preparation of the fiber sensor is similar to §3.2.2.1. Briefly, a 20 mm segment of PCF is fusion spliced in between MMF using electric arc splicer (Type 39, Sumitomo). All fiber ends are cleaved using a precision fiber cleaver (Fujikura, CT-30) prior to splicing. The fiber ends are aligned manually based on the fibers' edge and electric arc of 1 arbitrary step lasting 0.01s is applied with overlap of 10 μm. Repeat arcs each of 40 arbitrary steps and 0.40s are applied to collapse the PCF's air holes at the splice point. The PCF segment will later serve as the sensing region of the fiber sensor.

4.2.2.2 Preparation of PSS stabilized AuNPs colloid

All glassware involved in the synthesis of AuNPs are immersed in aqua regia consisting of nitric acid and hydrochloric acid in a 1:3 volume ratio then washed thoroughly with distilled water and oven dried prior to use.

8.5 mM hydrogen tetrachloroaurate is prepared in 0.1 w/v % PSS solution. To 11.5 ml of this solution, 0.115 ml of 0.1M sodium borohydride is added and the solution is stirred vigorously for 3 hours during which a wine red color develops. The PSS stabilized gold colloid is stored at 4 ^{o}C till use.

The number density of synthesized AuNPs can be increased by centrifuging the gold colloid at 150 000 rpm for 10 min at 4 ^{o}C and removing part of the supernatant before vortexing.

4.2.2.3 LBL assembly of Chitosan/AuNPs-PSS PEM

The PCF segment is immersed in Piranha solution (sulfuric acid and hydrogen peroxide in 7:3 volume ratio) and heated to 80 ^{o}C for an hour and washed thoroughly with distilled water and dried under nitrogen stream.

The PEM is formed by the layer-by-layer (LBL) technique by cyclical immersion in the constituting polyelectrolytes with a washing step in between until the desired number of layers is attained. The piranha treated fiber is first immersed in a 1 wt/v % Chitosan in 0.75 v/v % acetic acid with pH adjusted to 1.7 pH units using 1M hydrochloric acid for 15 mins then washed twice in pH 1.7 dilute hydrochloric acid for 1 min each before immersion in the PSS stabilized AuNPs colloid for another 15 minutes and similarly washed. This makes up a full cycle that forms a

Chitosan/AuNPs-PSS bilayer and is repeated till the desired number of bilayers is obtained. The PEM is left to dry under ambient conditions overnight.

4.2.2.4 Experimental setup

The experimental setup is similar to §3.2.2.6. One MMF end is connected to white light source (AQ4305, Yokogawa) and the other end to spectrometer (USB4000, Ocean Optics). The spectrometer is controlled by laptop running the software SpectraSuite. The PCF segment is held between fiber holders in a homemade sample chamber to prevent bending induced fluctuations.

pH response is characterized by flowing buffer solutions of varying pH into the sample chamber. The pH of the solution is simultaneously measured using a conventional glass electrode pH meter (Orion 320, Thermo) that has been precalibrated using standard pH buffers (CertiPUR, Merck).

4.3 Results and discussion

4.3.1 Characterization of AuNPs-PSS

Figure 4-2a shows the UV-Vis absorbance spectrum (UV-2450, Shimadzu) of the synthesized AuNPs along with the theoretical absorbance calculated from the multipole scattering theory [160] described in §3.3.1. A distinct absorbance peak centered at 531.5 nm is observed and the corresponding AuNPs diameter is estimated to be 50.6 nm. The broader absorbance peak for the empirical results arises from size inhomogenity within the AuNPs.

The AuNPs are also immobilized on a mercaptopropyltrimethoxysilane modified glass slide and viewed using field emission scanning electron microscope (FESEM, Jeol, JSM-6700F). The diameters of the AuNPs are measured using image processing software (ImageJ). The average diameter of 150 AuNPs is found to be 51.2 nm, in close agreement with theoretical values. The larger measured size may be attributed to thin film of Palladium that has been sputtered onto the sample to avoid charging effect. The size distribution of the AuNPs is presented in the histogram in Figure 4-2b.

The gold colloid is stable and no significant change in its UV-Vis spectrum for weeks as a result of electrosteric stabilization by PSS [176].

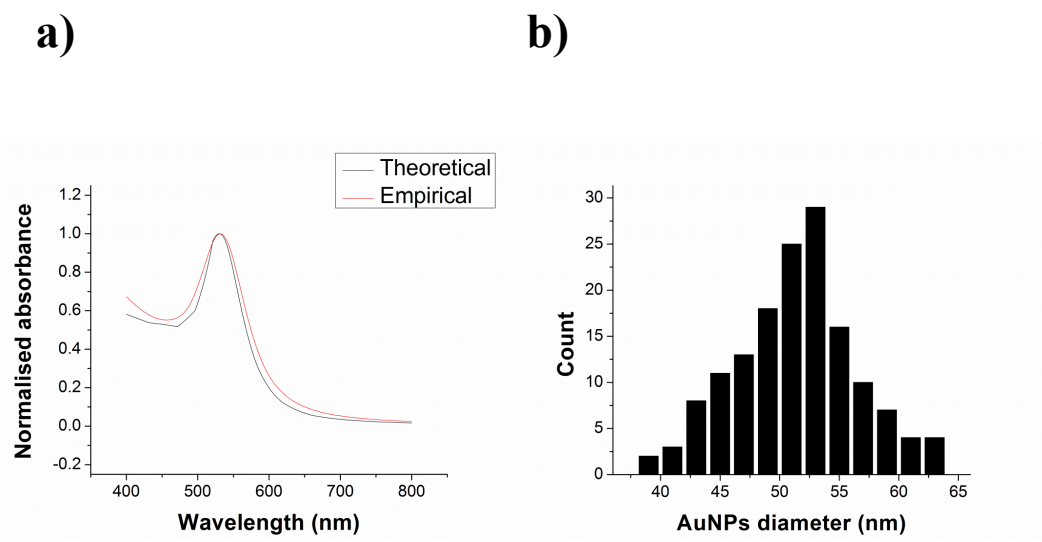

Figure 4-2: (a) Normalized UV-Vis spectra of synthesized AuNPs and theoretical calculation from multipole theory. (b) Histogram showing size distribution of 150 AuNPs.

4.3.2 Principles of operation of sensor

The LSPR effect and its application for sensing based on dielectric environment or interparticle distance changes that affect scattering and absorption properties has been described earlier.

The principles of operation of the sensor is described in §3.3.3 and is based on the evanescent field of cladding modes exciting LSPR of surface immobilised AuNPs.

4.3.3 PEM formation and characterization

The alternating adsorption of oppositely charged polyelectrolytes onto a charged substrate to build a multi-layered structure was first demonstrated by Decher et al [79]. Electrostatic attraction is the main contributor to PEM formation though hydrophobic interaction [177] and hydrogen bonding may also play a role. This LBL technique offers a facile and versatile approach to film formation on substrates of arbitrary shapes with fine control of film thickness, structure and composition through varying certain aspect of the coating process like polyelectrolyte used, ionic concentration, pH and temperature.

The PEM buildup is monitored via absorbance change after each bilayer is coated (Figure 4-3a). A distinct LSPR absorbance peak can be observed as early as the first bilayer. The peak center closely resembles that of the gold colloid used for coating, indicating successful incorporation of the AuNPs into the PEM structure. The absorbance values at 2 different wavelengths are plotted in Figure 4-3b where it can be observed that there is a slow initial increase in absorbance before an approximate linear increase in absorbance is observed from the 3rd bilayer onwards. The slow initial absorption of AuNPs is attributed to the substrate effect. The PEM is not strictly a stratified structure since interpenetration and complexation of newly absorbed polyelectrolytes with underlying layers take place which is absent in the initial layers that are in close proximity to the substrate [178]. The linear increase in

absorbance suggests a uniform increase in absorbed materials in each bilayer consistent with other reported PEM systems [179].

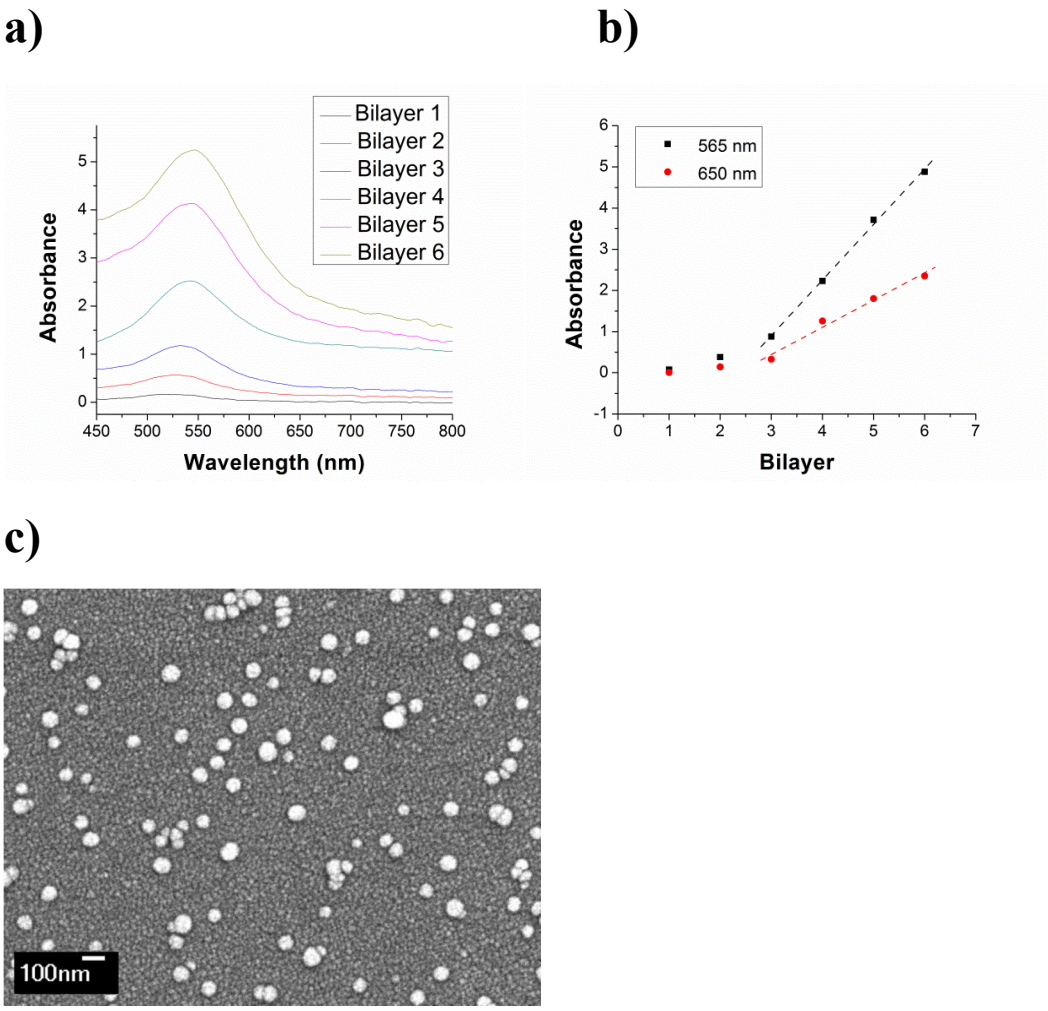

Figure 4-3: UV-Vis absorbance during PEM formation. (b) Absorbance at 565 nm and 650 nm during PEM formation, showing linear increase in absorbance from 3th bilayer onwards. (c) FESEM micrograph of AuNPs embedded PEM.

A FESEM image of a 5-bilayer PEM structure (Figure 4-3c) built using a 4X concentrate of the synthesized gold colloid shows the AuNPs to be fairly round in shape and slight aggregation of AuNPs is observed. The surface coverage of the AuNPs is fairly low at approximately 9.5% and explains the absence of secondary absorbance peaks [180].

4.3.4 pH response of LSPR sensor based on AuNPs embedded PEM

Figure 4-4 shows the pH response of the fiber sensor. The transmittance and absorbance are referenced using the transmitted light intensity of a coated fiber sensor when exposed in air. The transmittance spectrum is plotted in Figure 4-4a, with the transmittance change at 585 nm (marked by vertical line) versus pH in Figure 4-4b. There is clearly an increase in transmittance when pH is increased.

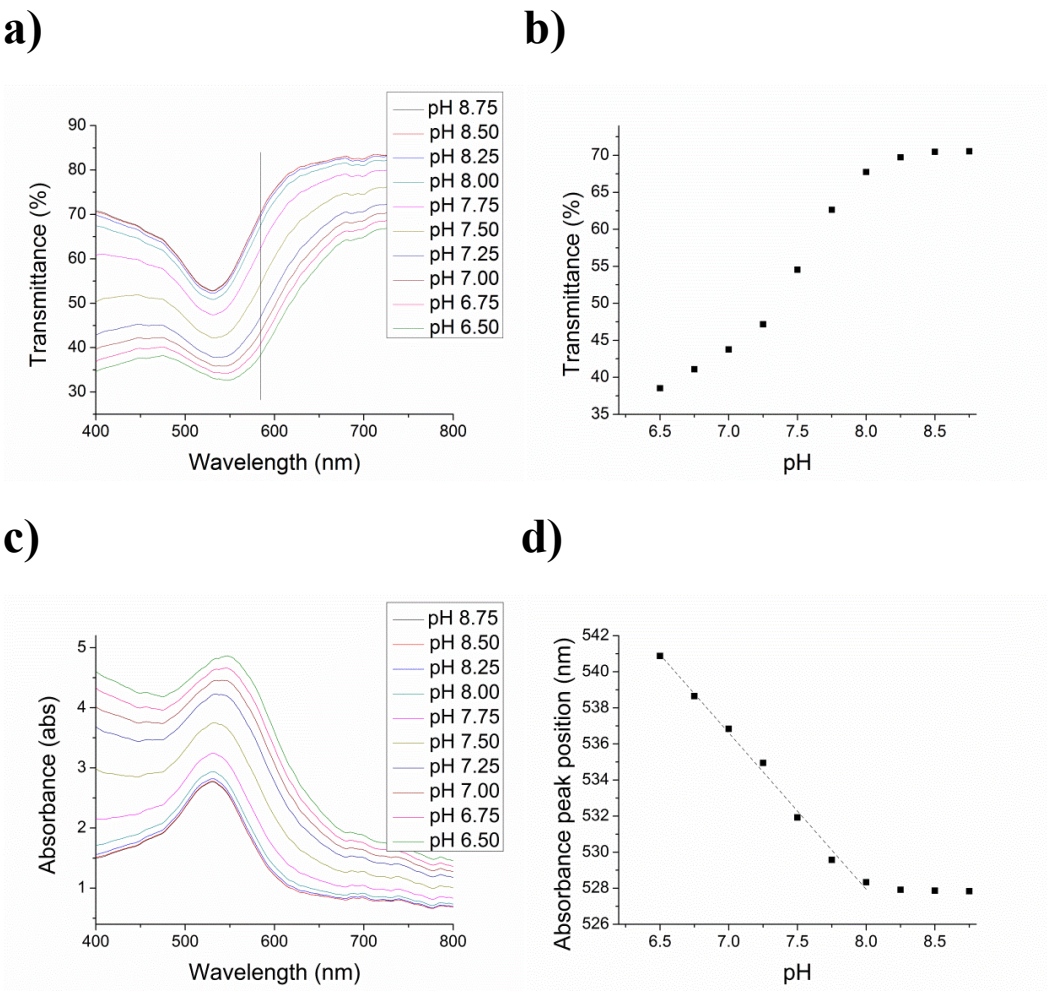

Figure 4-4: (a) Monitoring transmittance change with pH. (b) Plot of transmittance at 585 nm versus pH. (c) Monitoring absorbance change with pH. (d) Plot of absorbance peak position versus pH. A 5-bilayer PEM built from a 4X AuNPs-PSS concentrate is used.

The absorbance spectrum change with pH is shown in Figure 4-4c. A distinct LSPR absorbance is observed at all pH and absorbance values increase as pH is

decreased. A broadening of absorbance peak and shifting of peak absorbance towards longer wavelength are also observed. The absorbance peak wavelength is located using a centroid algorithm and plotted, displaying an approximately linear decline in peak position of approximately 8.67 nm/pH as pH is varied from 6.5 to 8.0 ($R^2 = 0.99$) (see Figure 4-4d).

The pH response of the AuNPs embedded PEM necessitates a discussion on the material properties of the components of the PEM. Chitosan (see Figure 4-5a) is derived from the partial deacetylation of chitin (poly (β-(1-4)-N-acetyl-D-glucosamine), a natural polysaccharide commonly extracted from the exoskeleton of crabs and shrimps [181]. It is the only pseudo natural cationic polymer and is a material of immense research interest due to its biocompatibility, biodegradability, film forming [182], anti-bacterial [183], chelating properties and the ease of modification of amino group at C2 position which allows design of polymers for use in diverse fields ranging from pharmaceutical [184], food, waste water treatment [185], etc. Owing to protonation of the amino functional group on the C2 position in acidic medium, Chitosan is a weak cationic polyelectrolyte with an apparent dissociation constant, pKa value of ~6.2 in water [186].

PSS (see Figure 4-5b) is a strong anionic polyelectrolyte whose ionization is independent of the surrounding pH and is most common component used to model a polyelectrolyte multilayer system [187]. Its sulfonate groups interact electrostatically with protonated amino group on Chitosan and also forms hydrogen bonds with hydroxyl groups (on C3 and C6) of Chitosan [188]. Both materials are selected for the PEM due to their biocompatibility and their capability to form highly swollen structures due to a lower degree of cross linking [189].

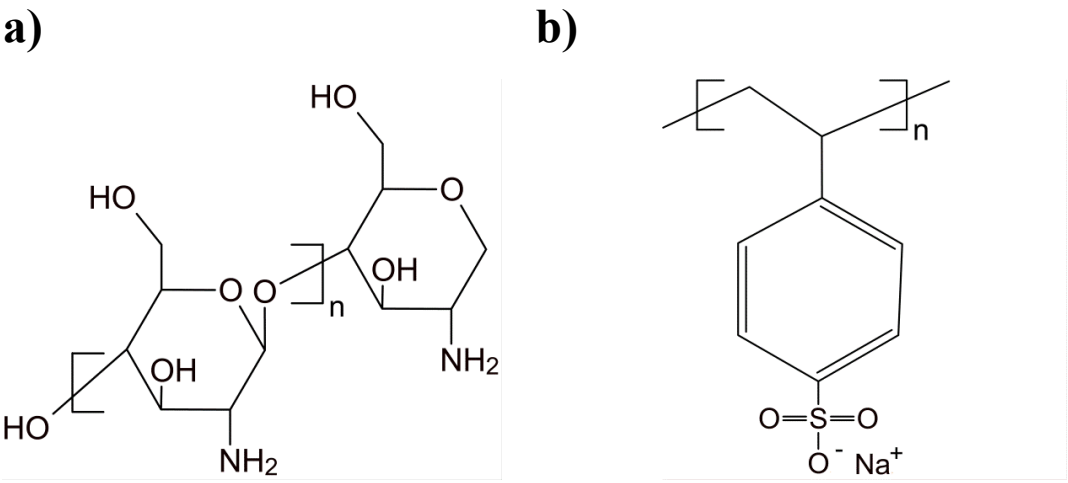

Figure 4-5: Chemical structure of (a) Chitosan, (b) PSS.

The pH dependent behaviour of the Chitosan/AuNPs-PSS PEM arises from ionisation of Chitosan. Deprotonation of amino group on Chitosan (Ch) occurs at high pH:

$$Ch - NH_3{}^+ \rightarrow Ch - NH_2 + H^+$$

resulting in an excess negative charges contributed by PSS. Repulsion between PSS leads to PEM swelling that increases the interparticle distance between the embedded AuNPs, reduce the extent of plasmonic coupling and thus lower LSPR absorbance and narrows the absorbance peak. The swelling of the PEM also reduces the dielectric constant of the AuNPs environment that shifts absorbance peak to shorter wavelength.

By letting

$$\alpha = \frac{[Ch - NH_2]}{[Ch - NH_2] + [Ch - NH_3{}^+]} = \frac{T - T_{min}}{T_{max} - T_{min}}$$

where T_{min} is the minimum transmittance corresponding to fully protonated Chitosan, T_{max} is the maximum transmittance when Chitosan is fully deprotonated, and α, the degree of deprotonation of Chitosan, the curve in Figure 4-6 is obtained from data

presented in Figure 4-4b. This curve is fitted using an extended Henderson-Hasselbach equation which describes the titration behavior of polyelectrolytes [190]:

$$pH = pK_a + nlog\frac{\alpha}{1-\alpha}$$

where *n* is an empirical parameter. The curve is a close fit (R^2 = 0.98) to the data points with a pKa value of 7.44 which is higher than commonly reported values of Chitosan in solution form [190, 191]. This is similarly observed for other PEM systems and attributed to energetically favorable ionic pairing in a PEM that makes polyacid more difficult to deprotonate, hence higher basicity [192].

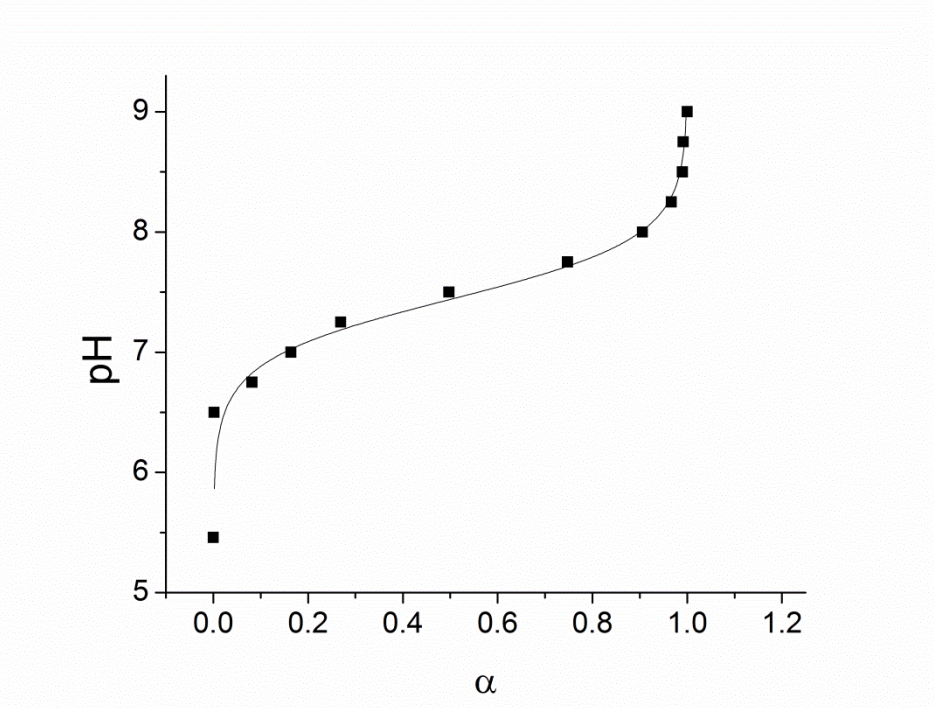

Figure 4-6: Fitting of empirical results with the extended Henderson-Hasselbach equation. (R^2 = 0.98).

4.3.5 Effect of number of bilayers

The pH response of fibers with varying number of bilayers is plotted in Figure 4-7. Sensors with a larger number of bilayers show a larger response with a 6 bilayers coated sensor showing an approximate 70% higher response than the 4 bilayers. All

curves show a similar inflection point, indicating that the apparent pKa of Chitosan in a PEM is relatively unchanged by the number of bilayers.

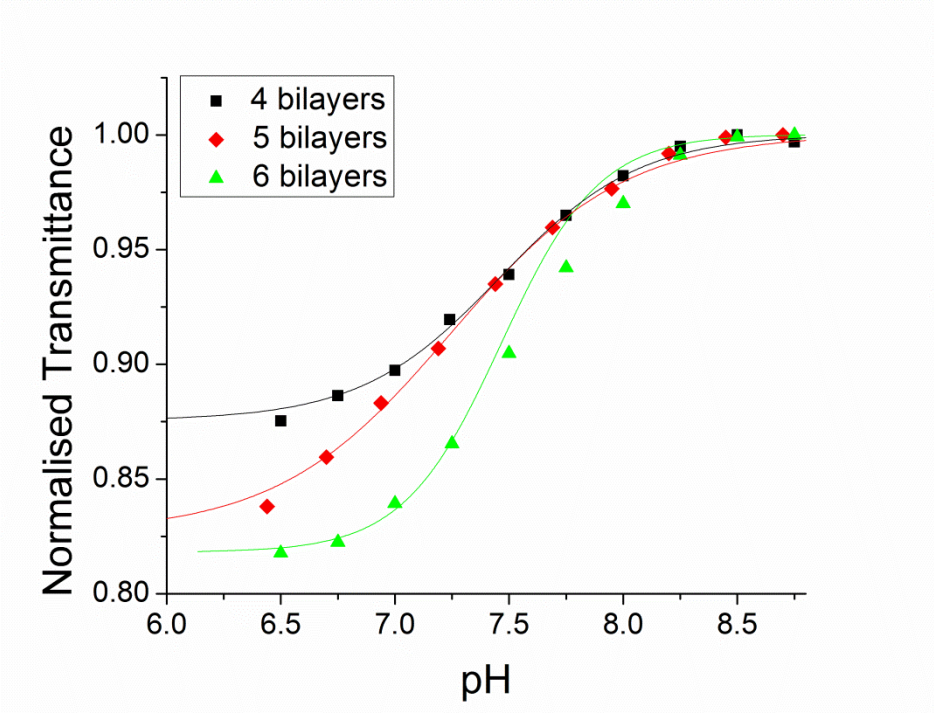

Figure 4-7: Effect of number of bilayers on pH response.

4.3.5 Effect of AuNPs loading

The amount of AuNPs absorbed into the PEM is increased by increasing the number density of AuNPs in the coating solution through centrifuging. The curve in Figure 4-8 compares the pH response of 5 bilayer PEM coated using a 1X and 4X concentrate of the synthesized gold colloid. Higher concentrate was found to be unstable and forms black particles and thus not explored.

A significant improvement in pH response (more than twice) is observed for the sensor coated using the 4X concentrate.

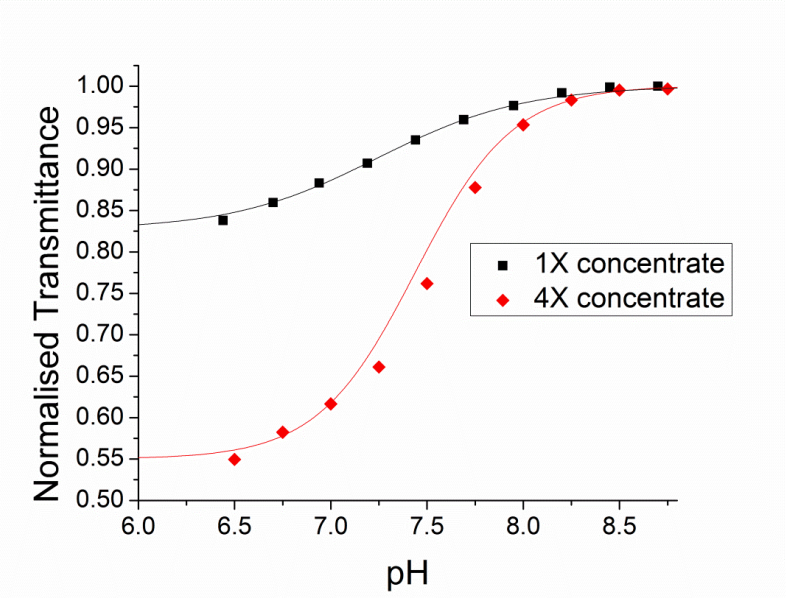

Figure 4-8: Effect of AuNPs loading on pH response. 5 bilayers PEM are used.

4.3.6 Dynamic response of the sensor

The dynamic response of a 5 bilayer PEM was tested between the physiological relevant pH range of 7.0 to 7.5 and shown in Figure 4-9. Rise and fall time to reach 90% response are 26 s and 166 s respectively which is sufficient for most biological measurements.

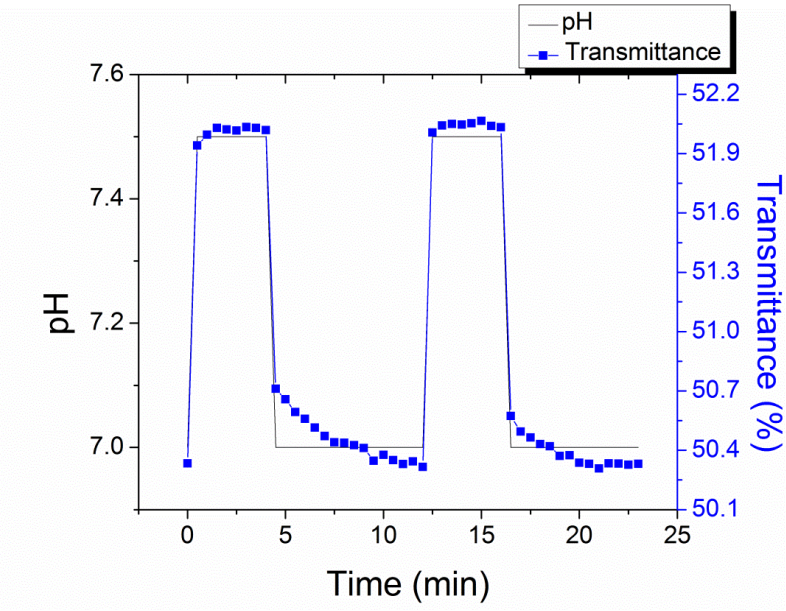

Figure 4-9: Dynamic response of pH sensor between pH 7.0 and 7.5.

4.3.7 Reflection configuration

To improve portability of the sensor, a reflection based sensor is investigated by coating the PEM on the end face of a MMF. The MMF is first cleaved with a precision cleaver and treated with Piranha solution as outlined in §4.2.2.3. A dip coater (KSV NIMA) is programmed to alternatively dip the fiber tip in Chitosan, water, AuNPs-PSS solutions to realize the PEM.

Figure 4-10 illustrates the setup for the reflection based sensor. Light is coupled into a 2X2 50/50 multimode fiber coupler. The PEM coated fiber tip is spliced to an arm on the other side of the coupler. The reflected light is detected by the spectrometer.

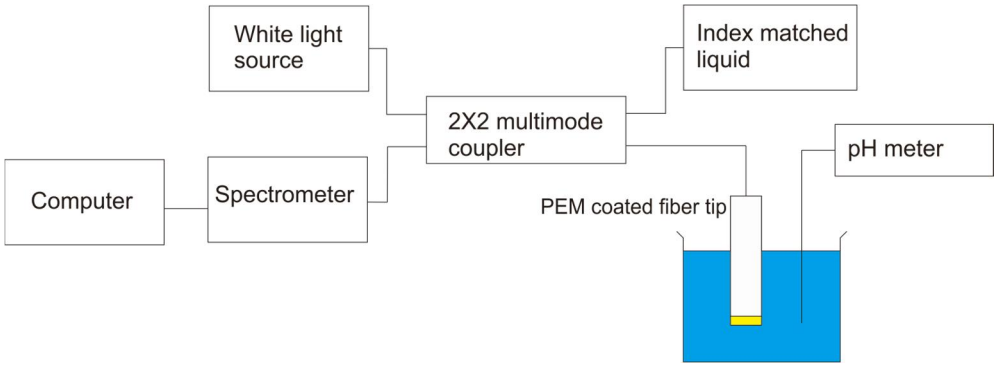

Figure 4-10: Illustration of experimental setup for reflection based sensor.

Reflectance is measured using reflected light off a clean cleaved surface as a reference. In contrast to the transmission based sensor where both absorbance and scattering of the AuNPs alter transmitted light intensity, only the backscattered light is measured in the reflection based sensor. LSPR leads to increased reflectance in the resonance wavelength, accounting for the reflectance peak seen in Figure 4-10 for a 5 bilayer PEM using 4X concentrate AuNPs-PSS.

Similar to §4.3.4, reflectance at 585 nm is used to monitor pH changes (see Figure 4-11). Reflectance is noted to decrease with pH increase and attributed to swelling of the PEM, leading to decreased scattering. There is no significant change in sensitivity and the pH response is a close fit to the extended Henderson-Hasselbach equation ($R^2 = 0.95$).

The reflection based sensor offers further advantages in its miniature size and probe tip design enables insertion of sensor into the body for in-vivo measurement. Use of automated dip coater allows inexpensive mass production of the fiber probe.

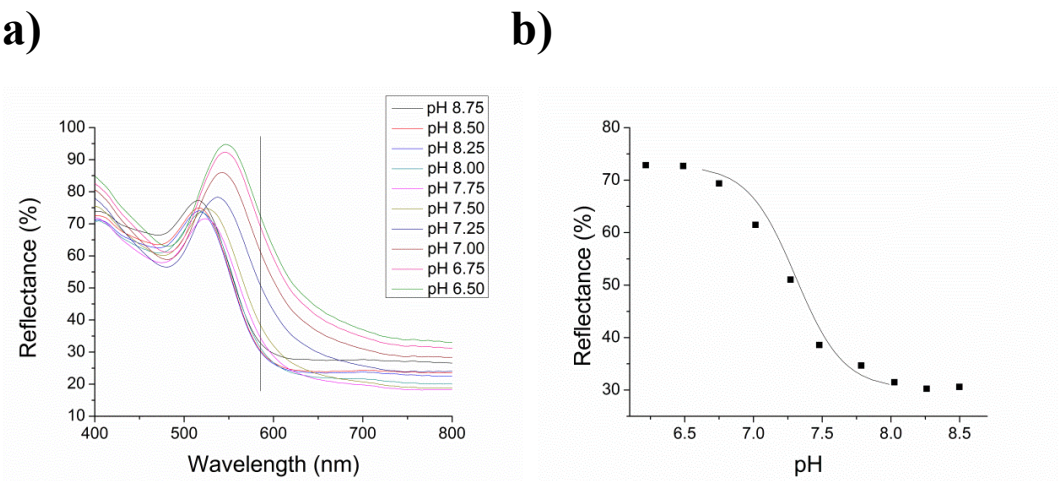

Figure 4-11: pH response of reflection based sensor using 5 bilayer PEM with increased AuNPs loading (4X concentrate). (a) Reflectance spectra. (b) Plot of reflectance versus pH at 585 nm.

4.4 Chapter conclusions

The fabrication and characterization of a LSPR fiber optic pH sensor is reported based on the refractometer reported in Chapter 3. A unique pH responsive PEM consisting Chitosan and PSS is fabricated onto fiber surface by LBL techniques. Both materials are biocompatible and Chitosan, in particular, is of immense research due to its abundance of amino groups that allow facile modification of chemical

properties for a wide array of applications including drug delivery, tissue engineering. AuNPs is synthesised in PSS solution and embedded within the PEM to report its pH dependent swelling/deswelling behaviour via LSPR.

The swelling/deswelling alter interplasmonic coupling between embedded AuNPs, resulting in increased/decreased absorbance or scattering. Both transmission and reflection based sensors are tested and pH response can be modelled by the extended Henderson-Hasselbach equation. Both show pH responsiveness within the physiological range of pH 6.5 to pH 8 with similar sensitivity. However, the reflection based sensor is much easier to fabricate and demonstrates potential for the fiber pH probe for in-vivo biological applications.

Few (if present) reports of a LSPR based pH sensor exist. Gayatri et al [193] reported a LSPR pH sensor fabricated by chemically attaching poly(allylamine) onto gold nanoprisms bound on a silanised glass surface. A LSPR peak shift of 17 nm was reported from pH 7.1 to 3.5. No sensitivity or limit of detection is given and the sensitivity of the sensor is limited to the acidic region.

Shao et al [194] reported a tilted fiber Bragg grating pH sensor based on self-assembled multilayer film, poly(diallyldimethylammonium chloride) (PDDA) and poly(acrylic acid) (PAA). The reported sensor is linearly responsive within the range of 4.66 to 6.02 with response time in order of tens of seconds similar to our reported sensor. However, the similarly responsivity to only acidic regions limits its application for physiological measurements which require that the sensor is responsive to pH around 7.4. In this regard, Gui et al [195] have designed a interferometer based pH sensor utilising a poly(diallyldimethylammonium) (PDDA) / poly(acrylic acid) (PAA) that is responsive between pH 3 to pH 10. However, the

sensitivity, though not explicitly stated is relatively lower than this reported work as well as that reported in the next Chapter.

Chapter 5

Double-pass Mach Zehnder fiber interferometer pH sensor*

5.1 Introduction

While PEM offers a versatile approach for thin film formation with precise control of thickness and morphology, their usage in chemical sensing has largely been limited to pH or merely as a supporting matrix. In this chapter, hydrogel (§2.4.3) is explored for sensor applications using an interferometry based transducer.

The basics of interferometry is introduced in §2.3.2 and reiterated here with emphasis on the Mach Zehnder configuration (see Figure 5-1). A physical or chemical parameter introduces a phase difference between two coherent beams of light which interfere, with the phase interference measured by fringe counting or incremental phase [196]. In a typical Mach Zehnder setup, a beam splitter splits light from a coherent source into a reference path and a sample path that interacts with the sample. Light from both paths are later merged by another beam splitter and interfere. A phase difference with respect to the reference path is accrued due to light interaction with the sample in the sample path.

The phase, θ of the light travelling along one path is given by

$$\theta = knl$$

where $\underline{n}$ is the refractive index along the path length, l and k is the wavenumber given by $2\pi/\lambda$ where λ is the free-space wavelength of the light.

The phase is modulated by a variation in measurand, M that changes n, l or both:

$$\frac{d\theta}{dM} = knl\left[\frac{1}{l}.\frac{\delta l}{\delta M} + \frac{1}{n}.\frac{\delta n}{\delta M}\right]$$

The phase modulation of light is intrinsically highly sensitive to environmental modulation, making possible highly sensitive measurement with high resolution and high dynamic range [197].

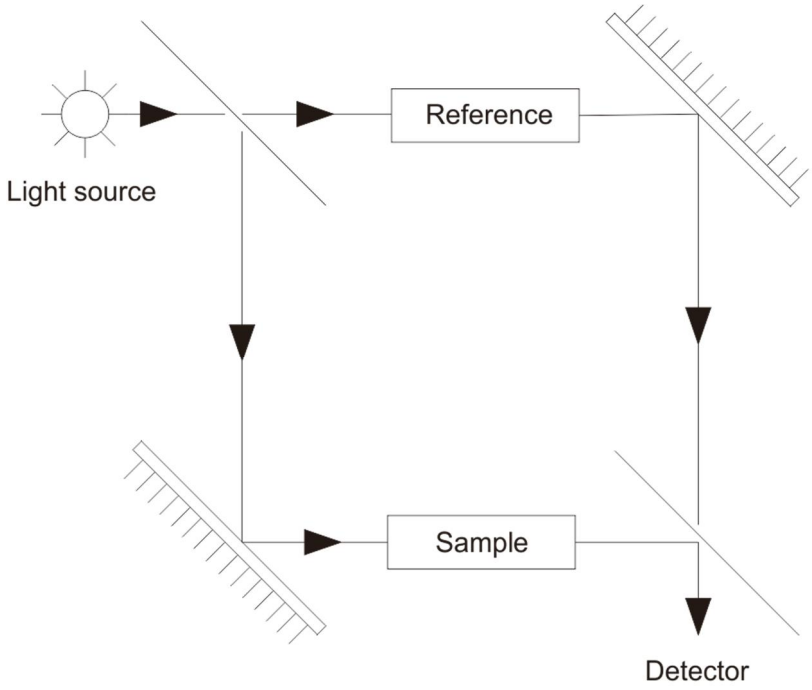

Figure 5-1: Mach Zehnder type interferometer.

The advantages of using fibers in interferometric sensors lie in eliminating the need for optical alignment while retaining the innate capability to increase sensitivity by simply increasing path length. This has spurred the development of various in line Mach Zehnder interferometer (MZI) whereby sample paths and reference paths are located on a single fiber. The core mode which is shielded from the environment usually serves as reference path and cladding mode which propagates via reflection off the cladding-exterior interface serving as sample path. Various ways for splitting light into core and cladding mode have been reported, including the use of LPG [198], splicing optical fiber with a deliberate fiber offset [199], splicing fibers with core mismatch [200] or by tapering fibers [201].

In this work, a MZI similar to work by Choi et al [202] who reported an all fiber MZI based on photonic crystal fiber (PCF) for strain and temperature sensing. PCF is a class of novelty fiber first fabricated in 1995. It guides light by confining it within a periodic array of microscopic air holes running along the fiber length [203]. Choi proposed the use of a solid core PCF as the sensing element of MZI. Light coupling into the core and cladding modes of the PCF was achieved by deliberate collapsing of the air holes at splice intersection with lead-in and lead-out single mode fibers (SMF). Due to PCF construction from a single material, it has very low temperature cross sensitivity that plagues LPG based MZI.

We propose a double-pass fiber MZI by coating a silver mirror on the distal end of the fiber to reflect light which is in turn made to transverse the MZI a second time. The MZI is coated with a pH responsive poly(2-hydroxyethyl methacrylate-co-2-(Dimethylamino)ethyl methacrylate) hydrogel film that exhibits a distinctive pH-dependent volume phase transition [210] to fabricate a MZI based pH sensor. By using a phase modulated interferometry technique, the pH sensor is insensitive to

many problems of many fluorescence based sensors including source fluctuation, photobleaching, fluorophore leeching. Our experimental results have demonstrated that the pH fiber sensor exhibits good sensitivity to pH changes within the physiological range along with good repeatability, responsiveness. In addition, we have also demonstrated the capability of the sensor for in-vitro monitoring of media pH in cell culture experiments. The promising results pave the way for using hydrogel coated interferometry based pH sensors for in-vivo applications.

The detailed construction of the pH sensor and experimental setup is given in §5.2 with results and discussion in §5.3.

5.2 Materials and method

5.2.1 Materials

Optical fibers including SMF and PCF (10.1/125 μm LMA-10) are purchased from Corning and NKT Photonics respectively.

Anhydrous methanol, sodium hydroxide granules, silver nitrate, 2-hydroxyethyl methacrylate (HEMA), 2-(Dimethylamino)ethyl methacrylate (DMAEM) and ethylene glycol dimethacrylate (EGDMA) are purchased from Alfa Aesar and glucose, tin dichloride, 3-(Trimethoxysilyl)propyl methacrylate (TMSPM) and N, N, N', N'- tetramethylethylenediamine (TEMED), inhibitor removers and ammonium persulfate (APS) are procured from Sigma. Sulfuric acid (95-97%) and hydrogen peroxide (30%) are from Merck and VWR respectively.

All reagents are of analytical grade and solutions are prepared using ultrapure water with resistivity 18.2 MΩ cm from Milli-Q system.

5.2.2 Methods

5.2.2.1 Preparation of double-pass MZI

LMA-10 is a PCF in which light is confined within a 10.1 μm solid core via air holes arranged in a regular hexagonal lattice around the core.

A segment of LMA-10 is stripped of its acrylate jacket and fusion spliced in between SMF using an electric arc splicer (Type 39, Sumitomo). SMF is used instead of MMF (used in previous chapters) since modal interferometry is used as the optical technique. Thus, it is crucial that light propagates in a single mode and is split into multiple optical modes only at the sampling site where various optical modes experience varying interaction with the sample, accumulating in a phase difference when recombined into a single mode and measured. All fiber ends are stripped of the acrylate jacket and wiped with ethanol to remove any debris prior to cleaving with a precision fiber cleaver (Fujikura, CT-30).

The arc splicer is operated in the manual mode and fiber ends are aligned based on their edge. An electric arc is applied to melt the fiber ends while simultaneously pushing the fibers towards one another. Repeat arcs added to collapse the air holes at the splice intersection.

The SMF at one end is later spliced to an optical circulator while the SMF at the other end is cleaved and coated with a silver mirror (§5*.2.2.3)*.

5.2.2.2 Surface modification of LMA-10

The LMA-10 surface is hydroxylated by immersing in piranha solution (sulfuric acid and hydrogen peroxide in 7:3 volume ratio at 80ºC for an hour, followed by thorough rinsing with deionised water and drying under stream of Nitrogen gas.

The fibers are then silanised by immersion in 10 v/v % TMSPM prepared in anhydrous methanol for 4 hours and sequentially rinsed with methanol and water before leaving to dry overnight in the dark (to avoid UV exposure as the C=C groups on TMSPM are reactive.).

5.2.2.3 Coating of silver mirror

The silver mirror is coated on the cleaved SMF end using procedures adapted from Wang et al [204]. The piranha solution treated fiber tip is immersed in 8 wt/v % aqueous sodium hydroxide followed by 5 wt/v % tin dichloride to promote silver binding. A 2 wt/v % silver nitrate solution is prepared and aqueous ammonia is added drop wise until the solution just turns clear colorless. The fiber tip is dipped in a final solution consisting of the prepared silver nitrate solution and 4 wt/v % glucose solution in a 5:3 volume ratio for 2 hours after which it is rinsed with deionised water and dried under nitrogen stream.

5.2.2.4 Coating of pH-responsive gel on LMA-10

HEMA and DMAEM are treated with inhibitor removers prior to use. HEMA, DMAEM, EGDMA and water are mixed to obtain the pre gel solution. The amount of EGDMA which is used as the cross linker, is kept at 5 mole %. The total wt/v % of monomers is kept at 60%. The pre gel solution is degassed by bubbling nitrogen gas for 20 mins.

Free radical polymerization is initiated via addition of APS and TEMED (0.05 wt/v % and 0.10 wt/v % of final volume respectively). The fibers are affixed separately in custom made polydimethylsiloxane (PDMS) channels (see Figure 5-2). The pregel is injected into the channels and left overnight in a vacuum oven. The fibers are then removed from the channels by peeling off the PDMS mould and immersed in water to remove any unreacted materials from the hydrogel.

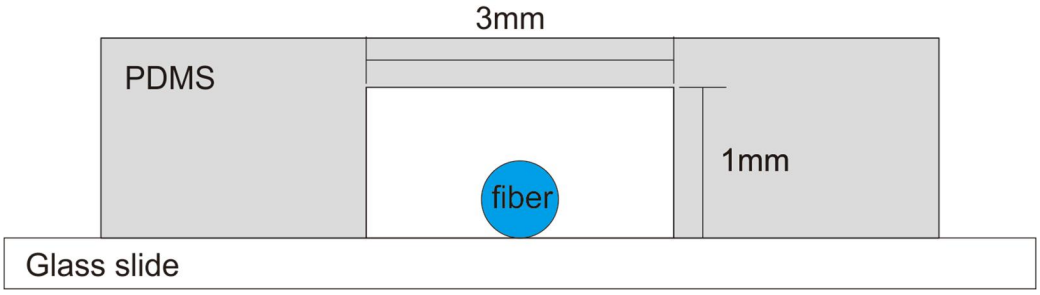

Figure 5-2: Transverse section of PDMS channel used for hydrogel coating.

5.2.2.5 Cell culture of A-375 melanoma cells

A-375 melanoma cells are obtained from ATCC and cultured using Dulbecco's Modified Eagle Medium (Gibco, 10566) with 10 v/v% fetal bovine serum (Gibco, 10270) and 1 v/v% Penicillin Streptomysin (Gibco, 15140) in an incubator maintained at 37 ^{o}C and a 5% carbon dioxide atmosphere.

The cell culture medium, DMEM, is used in a wide range of mammalian cell culture applications. It consists key amino acids, vitamins and inorganic salts required for cell survival and proliferation. pH regulation is achieved by the bicarbonate buffering system from bicarbonate salts in the DMEM and atmospheric carbon dioxide that dissolves into the medium.

$$CO_2 + H_2O \rightleftarrows H_2CO_3 \rightleftarrows HCO_3^- + H^+$$

Any disturbance of pH (within the buffering capacity) will be compensated by a shift in the chemical equilibrium according to Le Chatelier's principle, thus maintaining pH at approximately 7.4 (in 5% atmospheric carbon dioxide environment).

An initial 25,000 cells are seeded in a 24-well plate. The cell proliferation and pH of the culture medium are monitored daily over 7 days. The pH of the medium is measured both by the proposed optical fiber sensor and a conventional glass electrode pH meter (Jenning). Cell proliferation is monitored by trypsin (BI, 03-050-1B) treatment followed by cell counting in a hemocytometer using trypan blue (Gibco, 15250) staining.

5.2.2.6 Experimental setup for double pass MZI pH sensor

A broadband light source (AS3223-BA2) with emission wavelengths from 1530 nm to 1605 nm is used to interrogate the fiber sensor with the reflected light detected by an optical spectrum analyzer (AQ6370, Yokogawa) via an optical circulator as outlined in Figure 5-3. The reflection spectra are recorded and further processed using Matlab. pH response is characterised by immersing the pH sensor in phosphate buffer saline spiked with aqueous hydrochloric acid or sodium hydroxide.

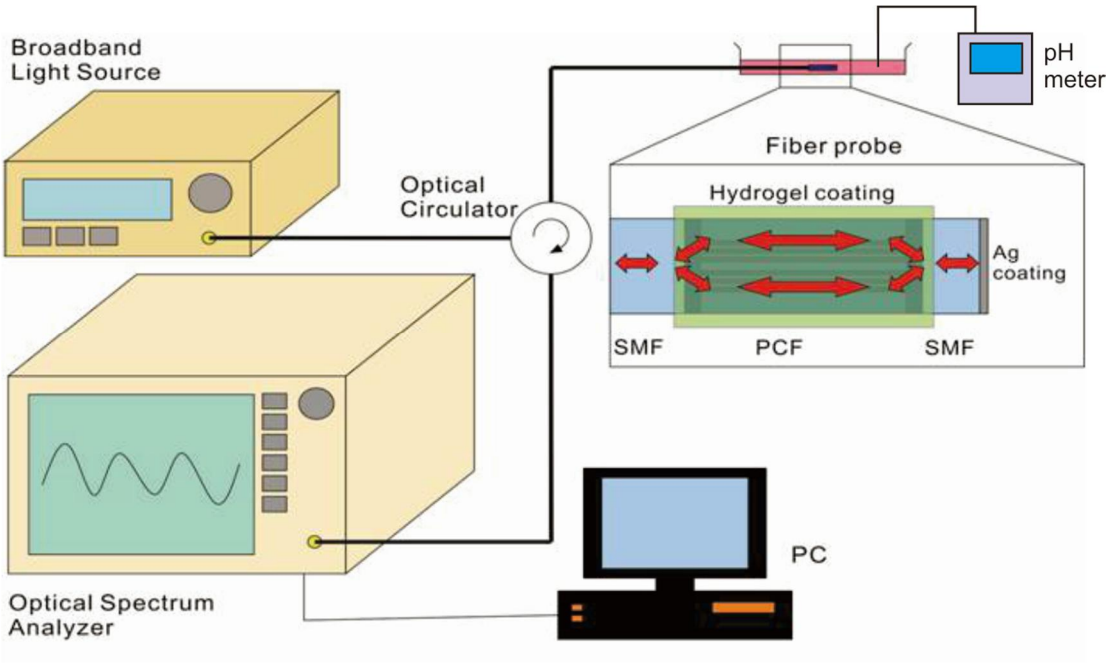

Figure 5-3: Experimental setup for double-pass MZI pH sensor.

5.3 Results and discussion

5.3.1 Principle of operation of MZI and the improved double-pass MZI

Light from the broadband light source is coupled into SMF and guided as a single fundamental mode. On reaching the first splice intersection of collapsed air holes, the fundamental mode is enlarged since there is total loss of light confinement in the uniform refractive index collapsed region. This enlarged mode excites both the core and cladding modes within the PCF which are later recombined into the SMF fundamental mode by the second collapsed region. The effective index difference between the excited PCF core and cladding modes induce phase difference responsible for intermodal interference.

By assuming the excitation of a single main cladding mode, the interference can be described as a two beam interference with transmission intensity, I that is commonly given as [202]:

$$I = I_1 + I_2 + 2\sqrt{I_1 I_2} cos\Delta\theta$$

where I_1 and I_2 are intensities of the different modes and Δθ is the intermodal phase difference given by:

$$\Delta\theta = k\Delta n_{eff} L$$

where k, Δn_{eff} and L are the wavenumber, intermodal effective refractive index difference and length of the MZI respectively. Since the interference spectrum is usually measured as a function of wavelength, the phase can be expressed by the Taylor expansion of k at the center wavelength, taking into consideration only the first order term:

$$\Delta\theta \approx \Delta\theta_o - \frac{2\pi\Delta\lambda}{\lambda_o^2}\Delta n_{eff} L$$

With no initial intermodal phase difference, intermodal phase difference is linearly proportional to L, Δn_{eff} and wavelength deviation, Δλ where

$$\Delta\lambda = \lambda - \lambda_o$$

To take into account the effect of material and waveguide dispersion on Δn_{eff}, the phase relationship is generally expressed in terms of differential modal group index, Δm_{eff}:

$$\Delta\theta \approx \Delta\theta_o - \frac{2\pi\Delta\lambda}{\lambda_o^2}\Delta m_{eff} L$$

where

$$\Delta m_{eff} = \Delta n_{eff} - \lambda_o \frac{\partial}{\partial\lambda}\Delta n_{eff}$$

Again, assuming $\Delta\theta_o = 0$ since light is split from the same coherent source,

the cosine term can be expressed

$$cos\Delta\theta = \cos\left(-\frac{2\pi\Delta\lambda}{\lambda_o^2}\Delta m_{eff}L\right) = \cos\left[2\pi\left(\frac{\Delta m_{eff}L}{\lambda_o^2}\right)\Delta\lambda\right] = \cos(2\pi\psi\Delta\lambda)$$

where ψ is the spatial frequency.

Since the PCF cladding mode reflects off the cladding exterior interface, a change in the exterior refractive index in the immediate vicinity within the penetration depth alters its modal effective index. Since the PCF core mode has no interaction with the exterior, this is accompanied by similar change in Δm_{eff} and $\Delta\theta$.

The response of this single pass MZI to external refractive indices is tested in glycerol (Sigma Aldrich) solutions of varying concentration. The refractive indices of the glycerol solutions are measured using an electronic portable refractometer (Atago, PAL- RI). The interferograms of the MZI in the glycerol solutions are presented in Figure 5-4a.

The interference pattern exhibits 3 distinct transmission minima within the excitation bandwidth (referred as 1 to 3 from left to right). The shifting of the local transmission minima (w.r.t to RI 1.3324) are plotted in Figure 5-4c. The minima positions are observed to shift towards higher wavelengths when external refractive index is increased. The sensitivity of the local transmission minima shift in response to external refractive index varies from minima to minima (63.4 nm/RIU, $R^2 = 0.984$; 40.9 nm/RIU, $R^2 = 0.993$; 75.3 nm/RIU, $R^2 = 0.999$). This is because the interference pattern is not perfectly sinusoidal as more than one cladding mode may be excited. This can be seen in the Fast Fourier Transform of the interferogram (Figure 5-4b). 3 distinctive peaks can be identified, thus at least 2 cladding modes are excited.

A common drawback of the MZI is the inverse relationship between the L and the free spectral range of the interference pattern (FSR) [205] that is the wavelength spacing between 2 successive minima. A longer L, while able to give higher sensitivity through a larger intermodal phase difference, decreases the free spectral range (FSR), thus limiting dynamic range.

We seek to mitigate this problem by coating a silver mirror at the interferometer end so that light propagates through the interferometer twice. This also turns the interferometer into a probe device that is more convenient for sensing application.

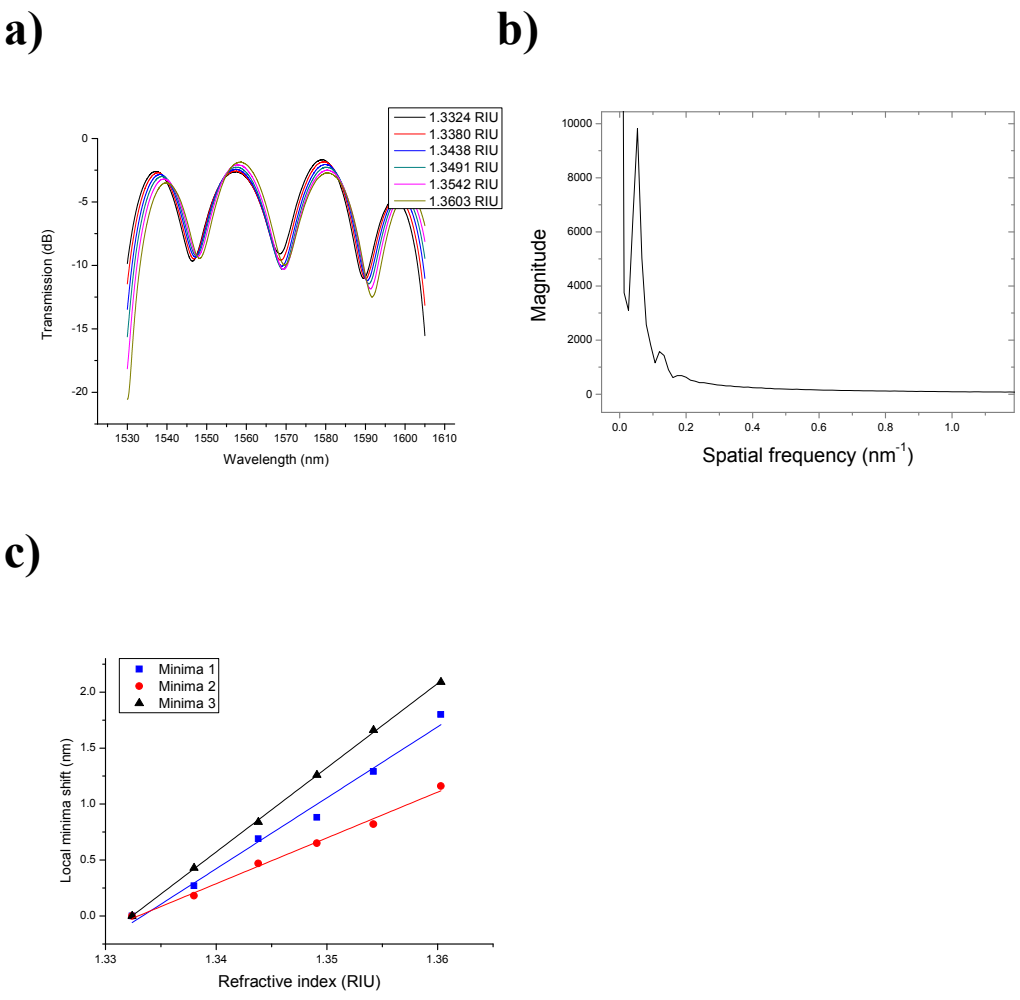

Figure 5-4: Interferogram (a), FFT spectrum (b), and local transmission minima shift (c) of a single pass MZI in response to refractive indices.

The reflectivity of the coated silver mirror is tested using a tunable semiconductor laser (Santec, TSL-510), power meter (Newport, 1935T-C) and an optical circulator setup. The reflected light power (@1550 nm) from a cleaved fiber end is measured to be 3.92 µW. After coating with the silver mirror, the power is measured to be 147.20 µW (approximately 37 fold increase). The optical power from the tunable laser coupled to the power meter via single mode patch cord is 1.50 mW. After accounting for optical loss from the optical circulator, the reflectivity of the silver mirror is estimated to be 17.4 %. This is a conservative estimate since the maximum port coupling loss of the circulator is used for the calculation and the clustering of silver nanoparticles could also have contributed to scattering loss.

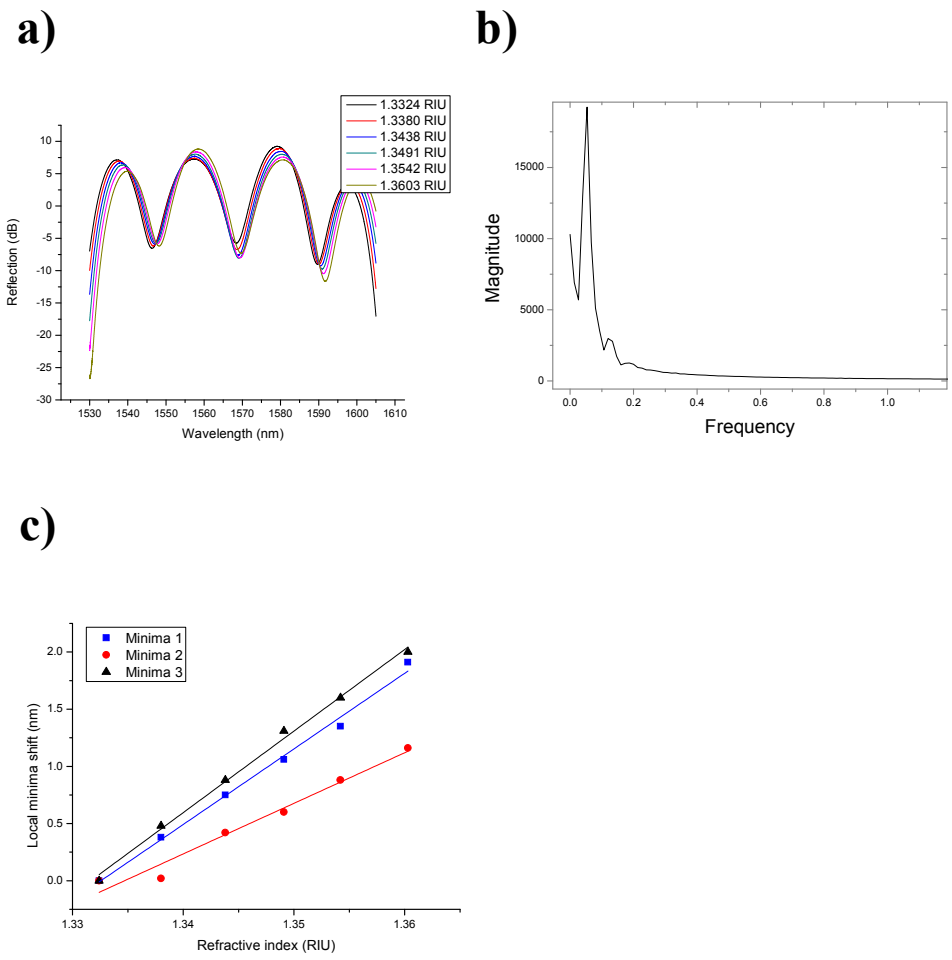

Figure 5-5: Interferogram (a), FFT spectrum (b), and interference minima shift (c) of a double-pass MZI in response to refractive indices.

Figure 5-5 shows the interference pattern for a double pass and MZI, FFT and minima position shift with change in external refractive index. Similarly, the minima positions are observed to shift towards higher wavelengths when external refractive index is increased. The minima positions can be fitted with a linear regression line with sensitivity 66.1 nm/RIU, $R^2 = 0.994$; 44.25 nm/RIU, $R^2 = 0.973$; 71.3 nm/RIU, $R^2 = 0.996$).Comparing the single-pass and double-pass MZI in Figure 5-6, it is surprising that there is no significant improvement in sensitivity for double-pass MZI despite light transversing the sensing arm twice. However, larger fringe contrast is observed in the interferogram of the double-pass interferometer. Peak-to-peak values normalized with respect to the FSR was 0.863 and 0.444 for double-pass and single-pass interferometer respectively, hence the quality factor, Q of the double-pass interferometer is improved [206].

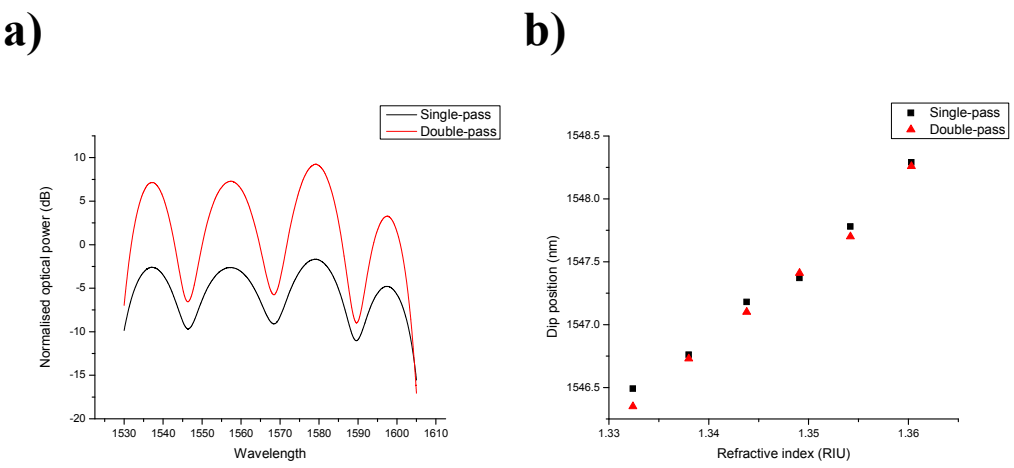

Figure 5-6: Comparing performance of single-pass and double-pass MZI. (a) Higher Q factor for double-pass MZI. (b) Both MZI yield similar sensitivity.

5.3.2 Coating pH responsive hydrogel

Optical fibers are first silanized with TMSPM to modify the surface with vinyl group for chemical attachment with the pH responsive hydrogel. The hydrogel is formed by in-situ free radical initiated polymerization process from pre gel mixture

of the constituent monomers, cross linkers and initiators. The relative amount of monomers, cross linkers and initiator influences the morphology and structure of the hydrogel which in turns affects its swelling/deswelling characteristics. A major challenge lies in the reproducible coating of a thin uniform hydrogel film on the optical fiber. A thin film is desirable since the swelling and deswelling is in part a diffusion driven process and a thicker film would degrade responsiveness of the sensor. Surface initiated polymerization that immobilizes initiator on the surface to fabricate ultra-thin hydrogel films (5-100nm) have been reported [207] but is cumbersome to implement on optical fibers as it requires additional chemical modification steps. By carrying out the polymerization process in custom made PDMS channels, a hydrogel film several micrometers in thickness on the optical fiber can be formed (see Figure 5-7). While the method produces hydrogel coatings of reproducible thickness according to the dimensions of the PDMS channels, Chapter 6 furthers explores a poly(vinyl alcohol) gel coating that can be coated by facile dip coating without need for the PDMS mold.

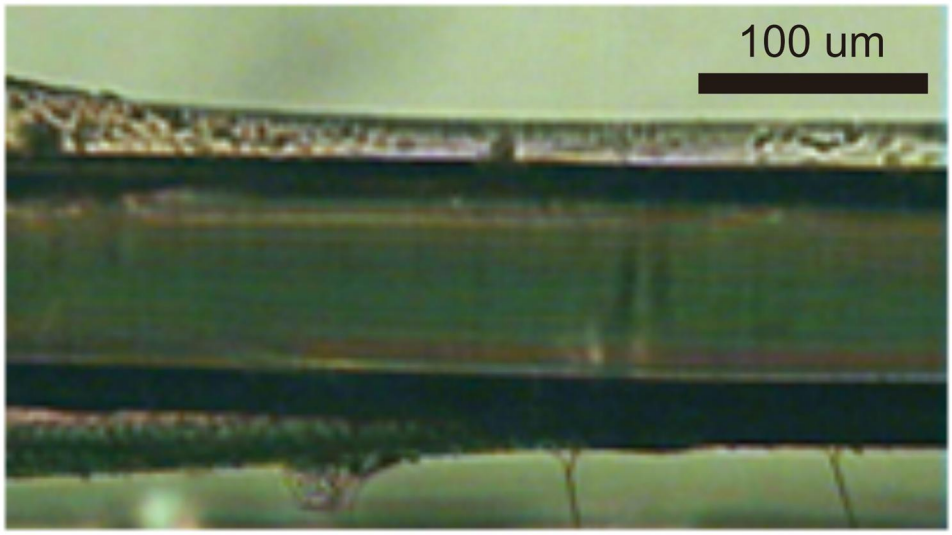

Figure 5-7: Micrograph of hydrogel coating on optical fiber.

5.3.3 pH response of double-pass MZI pH sensor in spiked phosphate buffered saline

The interference spectra while the pH probe is immersed in PBS of varying pH are shown in Figure 5-8 with the corresponding shift in spectral minima position. The spectral positions were obtained using a Matlab script that locates spectral minima based on the first derivative of spectra data. It is observed that spectral minima consistently shifts to longer wavelength when pH is increased from 5 to 9.

This behavior is attributed to the swelling/deswelling behavior of the hydrogel in response to pH. The hydrogel, having a higher refractive index than the solution, increases the refractive index at the fiber surface when it deswells. This increases the effective index of the cladding mode, causing the interference pattern to shift towards longer wavelength. The reverse is true when the hydrogel swells, reducing the refractive index at the fiber surface.

This swelling/deswelling behavior of hydrogels is described previously by thermodynamic theories which treat swollen gel as a polymer solution of an analogous linear polymer in a solvent [208, 209]. Polymer-solvent interactions, governed by thermodynamic variables, determine the mixing tendency between polymer and solvent responsible for driving solvent into the gel, thus exerting an expansion force that is opposed by an elastic retractive force exerted by polymer chains between the crosslinks. An equilibrium swelling state is reached when expansion force balances the retractive force.

pH responsive gel incorporates ionisable acidic or basic groups that alter their swelling behavior. The ionization state of these groups is affected by local pH and changes the charge density within the gel. Here, DMAEM is co-polymerized with

HEMA with the former contributing basic amino groups to the gel network. Under acidic conditions, protonation of the amino groups within the gel leads to an increased charge density. Electrostatic repulsion between the charged groups causes the expansion of the gel network. In addition, diffusion of counter ions from the solution to balance the internal charges also increases the osmotic pressure within the gel and contributes to gel swelling. The equilibrium swelling of pH responsive gel has been modelled by various groups and found to depend on charge of the ionic monomer, pKa of the ionizable group, mole ratio of ionizable monomer, degree of crosslinking and nature of surrounding solvent [210].

The graph in Figure 5-8b assumes a typical sigmoidal titration curve with an apparent pKa value fitted to be 7.31. This is approximately 1.1 pH units lower than the pKa of DMAEM in solution [134] as more acidic condition is required to protonate DMAEM in the polymeric form owning to unfavorable electrostatic interactions [211]. The apparent pKa is close to physiological pH of pH 7.4, making it apt for physiological measurements due to its high sensitivity around the physiological pH.

A linear regression line can be used to fit the pH range: pH 6.75 to 8.25 with R^2 value of 0.986. The pH sensitivity within this linear range was 1.71 nm/pH which is higher than reported sensors using pH sensitive polyelectrolyte multilayers [212, 213]. The limit of detection (LOD) based on a ratio of sensitivity over 3σ, where σ is the standard deviation of 5 readings, is 0.004.

a)

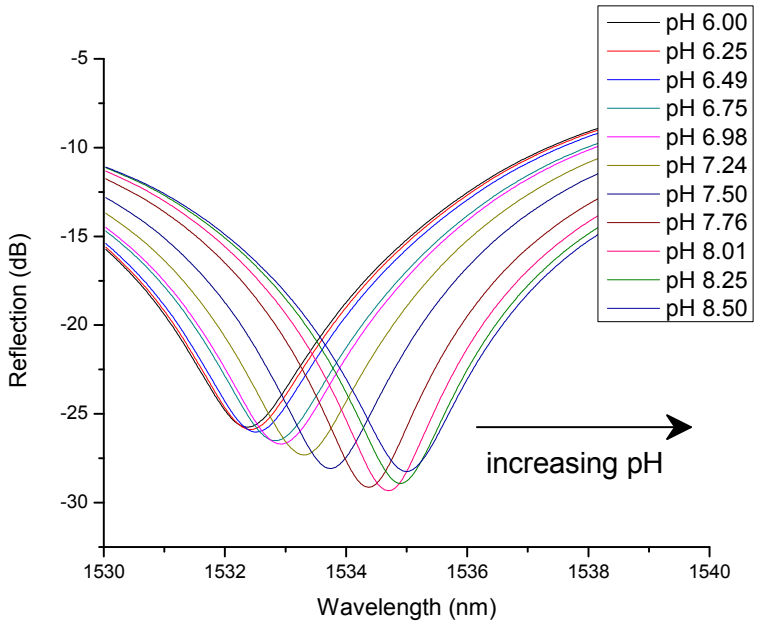

b)

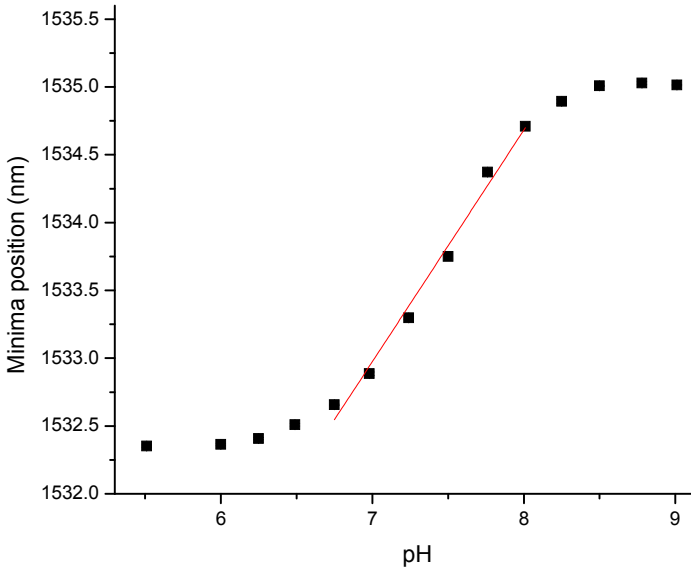

Figure 5-8: (a) Interferogram at varying pH in phosphate buffered saline. (b) Corresponding spectral minima position. The DMAEM in pre gel mixture was 10 mole %.

5.3.4 Responsiveness of the pH sensor

The responsiveness of the proposed pH sensor is tested by allowing the sensor to equilibrate in spiked PBS of pH 6.75 before changing to a spiked PBS of pH 7.75 (Figure 5-9). The solution was changed to pH 6.75 spiked PBS following equilibrium at the higher pH.

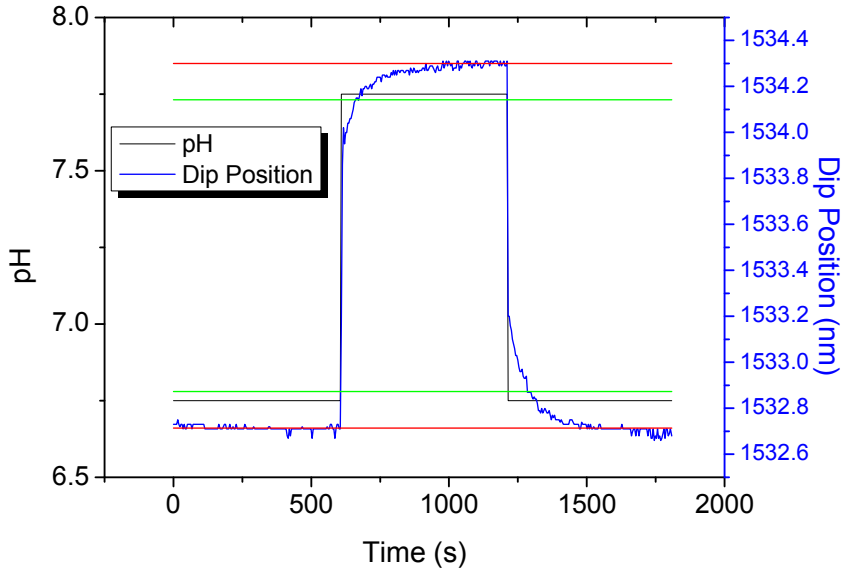

Figure 5-9: Step response of fiber pH sensor from pH 6.75 to pH 7.75.

The time taken to reach 90 % response, τ_{90}, was measured to be 55 s for change to higher pH and 79 s for change to lower pH. This responsiveness is slightly improved over other reported hydrogel based pH sensor [214] and is in part due to the robustness of an optical based sensing platform. The diffusion of protons through the hydrogel matrix plays an important role in the kinetics of gel swelling/deswelling [215], thus thinner gel with larger mesh size (see §2.4.3) are thought to be more responsive. The responsiveness of our sensor could be further increased by decreasing the gel thickness, decreasing cross linking density by reducing molar ratio of EGDMA in the pre gel solution or by introducing a interconnected pore

network structure through use of sacrificial components [195]. Nevertheless, the responsiveness of the sensor is sufficient to investigate most biological processes.

a)

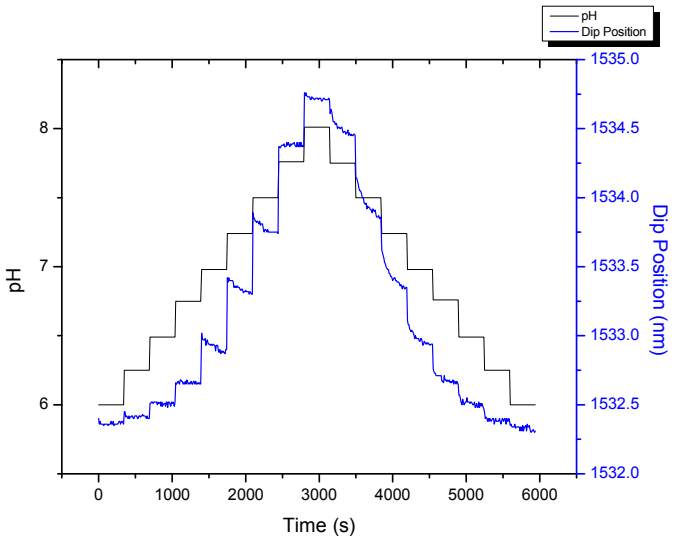

b)

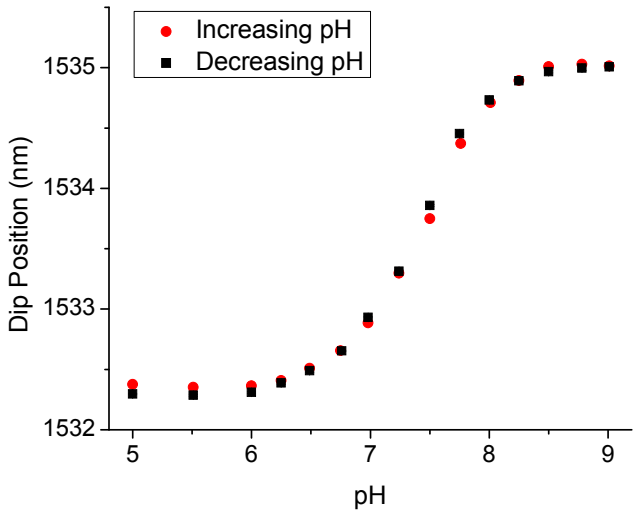

Figure 5-10: Sensor pH response under cyclic pH change. pH sensor shows minimal hysteresis with largest error of 0.8%.

5.3.5 Hysteresis behaviour of the pH sensor

The pH sensor is subjected to cyclic changes in pH to test for its repeatability which is essential for practical usage (Figure 5-10). The reversible swelling and deswelling of HEMA-co-DMAEM hydrogel ensures minimal hysteresis with largest reported error of 0.8%.

5.3.6 Stability of the pH sensor

The stability of the sensor was tested over an 8 hours period. Figure 5-11 shows the sensor performance with minimal fluctuations in PBS of varying pH. The maximum deviation is 0.04 nm corresponding to pH 0.0234 units. Therefore, the proposed sensor has minimal drifting and does not require frequent recalibration that is common for a conventional glass electrode pH meter, making the sensor suitable for continuous pH monitoring.

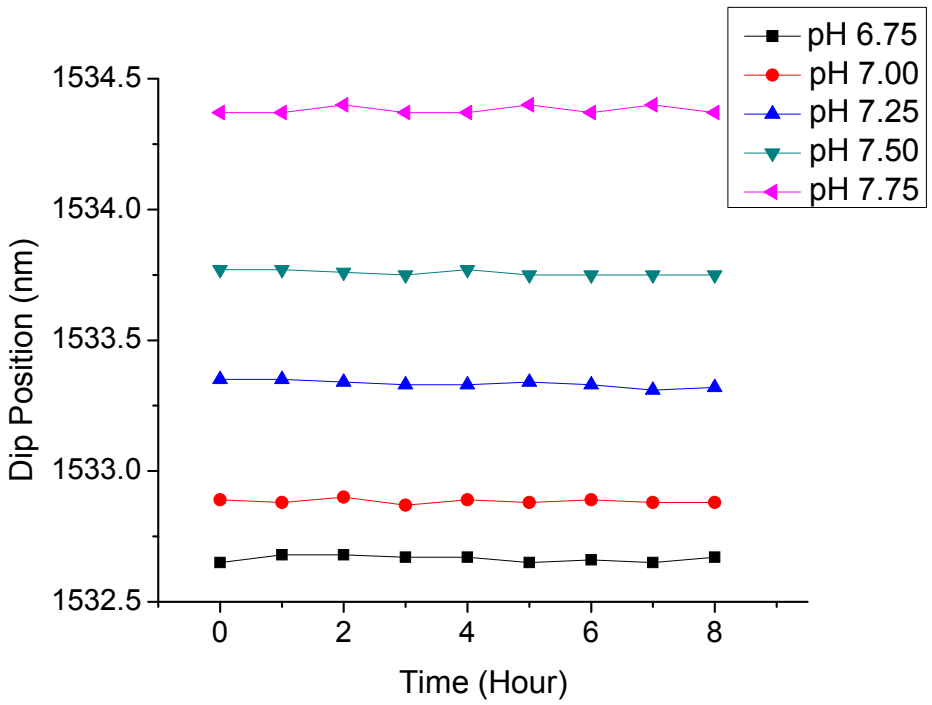

Figure 5-11: Stability of pH sensor over an 8 hour period.

5.3.7 Application of the pH sensor for cell culture monitoring

Extracellular pH is amongst the most important parameter influencing cell health and growth and is thus closely monitored in cell culture experiments. The unique demands for continuous monitoring over time under a sterile enclosed environment in typical cell cultures render the conventional glass electrode pH meter inadequate owning to its bulkiness and need for regular calibration and maintenance.

The proposed pH sensor poses several advantages like its miniature size. The use of HEMA as the backbone of the pH responsive gel ensures good biocompatibility, resistance to degradation and allows the sensor to undergo heat sterilization without sustaining damage.

The fiber pH sensor is calibrated in spiked culture media prior to measurement (Figure 5-12a). Figure 5-12b illustrates the pH change in the culture media measured by our fiber pH sensor and a conventional pH meter, highlighting the close proximity between readings from both devices with an average 0.465% error. The media pH is noted to drop drastically from Day 3 corresponding to a sharp increase in cell number before stabilizing at around pH 6.8 from Day 5. Cell death rate was below 10% throughout the duration of the experiment.

The data agrees with reported pH 6.5 -6.7 in in-vivo studies of tumor microenvironment [216]. The acidic microenvironment that has become characteristic of a tumor is the result of increased metabolic activities and a shift in cellular metabolism in response to hypoxia or in part, to confer competitive advantage over normal cells that are intolerant to acidity [217]. The fall in pH is also part of a malignant progression and favors upregulation of proteolytic enzymes that drives metastasis [218]. Clearly, pH is vital in cancer studies and our proposed

sensor could be useful in vitro studies to understand cancer or evaluate pH targeted cancer therapies.

a)

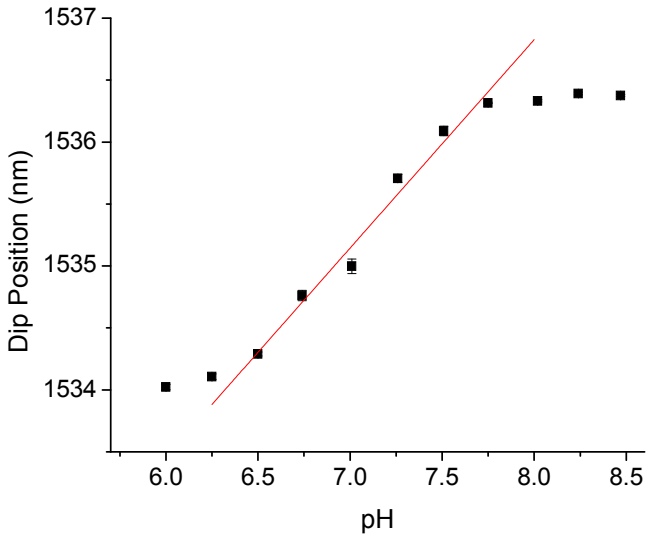

b)

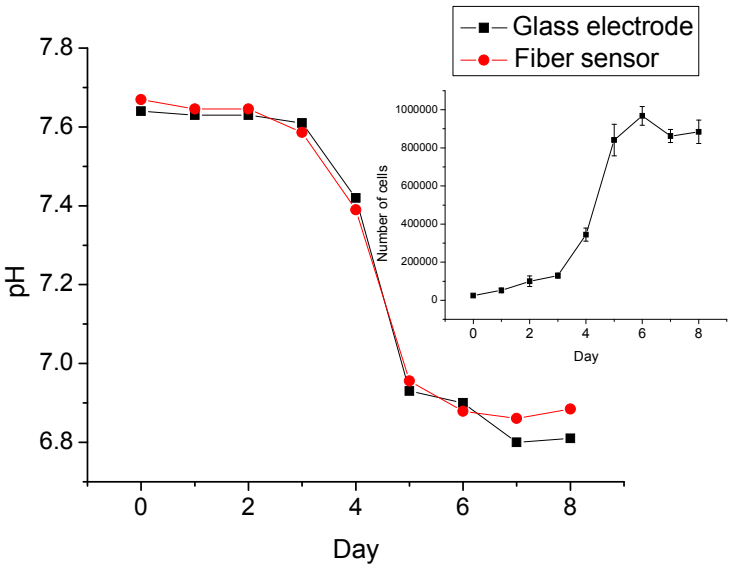

Figure 5-12 (a) Calibration of pH sensor in DMEM. Fitting of linear regression line between pH6.50 and pH7.75 with R^2 value of 0.9762. (b) Monitoring of cell culture pH using fiber pH sensor and glass electrode pH meter. Inset: Monitoring of cell proliferation.

5.4 Chapter conclusions

A fiber optic pH sensor has been demonstrated by coating a pH responsive HEMA-co-DMAEM hydrogel on a novel double pass Mach Zehnder interferometer and successfully applied in a cell culture experiment to monitor media pH. In spiked phosphate buffer saline, the pH sensor demonstrates high sensitivity of 1.71 nm/pH, pH 0.004 limit of detection with good responsiveness, repeatability and stability.

To date, hydrogels responsive to various stimuli ranging from the physical like temperature [135] to chemical like pH [134], heavy metal ion [219], bio/chemical molecules [220] have been developed and fiber interferometer proves a viable platform for various hydrogel-based sensors. A challenge lies in a facile method in coating ultra-thin hydrogel films of controlled thickness on optical fiber. This is addressed in Chapter 5 where a versatile hydrogel system is investigated that promises facile preparation of thin hydrogel film that is potentially applicable for a wide range of sensing applications.

Chapter 6

Poly(vinyl alcohol) hydrogel based fiber interferometer sensor for heavy metal cations*

6.1 Introduction

The previous chapter demonstrates the feasibility of a hydrogel based pH sensor on a fiber MZI platform, opening up numerous sensing possibilities for fiber MZI. While the pH sensor is capable of high sensitivity, responsive pH measurements with minimal hysteresis, one caveat lies in the redox initiated free radical polymerization technique commonly used for hydrogel formation. This technique, along with newer radical polymerization methods like atom transfer radical polymerization (ATRP) and reversible addition-fragmentation chain transfer (RAFT), requires an Oxygen free atmosphere to avoid unwanted consumption of free radicals. Furthermore, it is challenging to obtain a uniform hydrogel coating with precise control of thickness.

In this chapter, we propose a poly(vinyl alcohol) (PVA) -co-poly(acrylic acid) (PAA) hydrogel that offers a facile approach by dip coating. The hydrogel can be functionalized with receptors to perform specific sensing of a desired analyte. A heavy metal cation sensor is proposed here on a MZI as a proof-of-concept.

The use of heavy metals in modern industries has led to an ever increasing

environmental burden. These metals (e.g. Hg, Pb, Ni, Cu, Cd, Zn, As) are non-biodegradable and accumulate in the ecological systems, posing a serious threat to humans due to its toxicological and carcinogenic effects. High exposure to Ni, for instance, can lead to cardiovascular, lung and kidney diseases and even cancer through altering of cellular metabolism, gene expression, gene repair and increased oxidative stress [221].

Such is the adverse effect on human health that there is active research in new sensing strategies for trace heavy metals [222] and various health and environmental agencies have set standards on maximum allowable heavy metals.

Current techniques for trace heavy metal detection requires costly and sophisticated equipment like atomic absorption spectroscopy and inductively coupled plasma atomic emission spectroscopy that are operated by highly trained personnel, driving the need for inexpensive alternatives that could be rapidly adapted for continuous, remote monitoring applications.

Miniature fiber optic sensors capable of remote sensing offer a plausible alternative for trace metal sensing in the environment. Using a single-pass MZI similar to Ref [202] and described in §5.3.1, a thin submicron layer of PVA/PAA hydrogel film is coated via the dip coating method and chemically modified to be sensitive to Ni^{2+}. The hydrogel film is characterised using field emission scanning electron microscope (FESEM) and attenuated total reflection-Fourier transform infra-red (ATR-FTIR) and various design considerations are studied to optimise sensitivity of the hydrogel MZI sensor. The facile method of coating thin PVA/PAA hydrogel films and the ease in which the film can be modified with various receptors enables the setup to be adapted for other sensing applications.

The detailed construction of the sensor and experimental setup is given in §6.2 with results and discussion in §6.3.

6.2 Materials and method

6.2.1 Materials

Optical fibers including SMF (8.2/125 μm SMF-28) and PCF (10.1/125 μm LMA-10) are purchased from Corning and NKT Photonics respectively.

PVA with Mw 89,000 – 98,000, 35 wt% PAA with Mw 100,000, N-hydroxysuccinimide (NHS), N-(3-dimethylaminopropyl)-N'-ethylcarbodiimide (EDC), 5-amino-8-hydroxyquinoline dihydrochloride, ethanolamine are purchased from Sigma-Aldrich. Nickel (II) chloride (anhydrous) is from Alfa Aesar. Sulphuric acid (95-97%) and hydrogen peroxide (30%) are from Merck and VWR respectively.

All reagents are of analytical grade and solutions are prepared using ultrapure water with resistivity 18.2 MΩ cm from Milli-Q system.

6.2.2 Methods

6.2.2.1 Preparation of fiber MZI

The method of preparation is similar to §5.2.2.1 except that the arc power and duration have been increased to eliminate the need for repeated arcs. As a result, the segment length of collapsed air holes is increased. This excites higher order cladding modes as further discussed in §6.3.1.

The arc power, duration and offset applied are 41 arbitrary steps, 1.00 s and 10.00 μm respectively. A length of air holes at the splice joint is collapsed simultaneously during the fusion process due to interfacial tension when silica is melted. The fiber MZI is mechanically sound and able to withstand the splicer's inbuilt tensile test.

6.2.2.2 Coating PVA/PAA hydrogel on fiber

The PCF segment is immersed in piranha solution (sulphuric acid and hydrogen peroxide in 7:3 volume ratio) at 80 ^{o}C for 60 min and rinsed thoroughly with deionised water before drying under stream of purified nitrogen gas. The piranha treatment removes any organic residue and hydroxylates the fiber surface.

PVA and PAA are added to deionised water in the required amount to make 10 wt % polymer blend. This is stirred in a 80 ^{o}C water bath for 2 hours for complete dissolution and left to cool overnight with continuous stirring to ensure homogeneity.

A dip coater (KSV NIMA) is used to dip the optical fiber into the polymer blend and withdrawn at a constant speed of 100 mm/min. A thin film of polymer blend coats the fiber and is dried under room temperature conditions before heating in a 130 ^{o}C furnace (Carbolite). The fibers are then left to cool before immersing in water to remove excess polymers that have not been cross linked.

6.2.2.3 Chemical modification of PVA/PAA hydrogel

The PVA/PAA hydrogel coated fiber is immersed in pH 6 phosphate buffer consisting 0.13 M EDC and 0.33 M NHS for 60 mins followed by immersion in 0.01 M 5-amino-8-hydroxyquinoline dihydrochloride (prepared in 0.1 M tris(hydroxymethyl)aminomethane) pH 7.3 buffer) for 4 hours.

The fibers are kept in deionised water to remove any unreacted materials.

6.2.2.4 ATR-FTIR spectroscopy

ATR-FTIR is carried out using a Shimadzu IRPrestige-21 FTIR spectrometer attached with an attenuated total reflection accessory (PIKE MIRacle) that utilises a ZnSe crystal.

Samples are prepared by spin coating PVA/PAA blend on quartz slides and subjected to the required thermal treatment and chemical modification. All samples are dried in a vacuum chamber for a day prior to measurement to minimise background signal from water.

Samples are placed on the ZnSe crystal and clamped with constant pressure. 10 spectra are collected for each sample in the wavenumber range 750 to 3500 cm^{-1} with 4.0 cm^{-1} resolution and Happ-Genzel apodization. All spectra are ratioed against the clean ZnSe crystal surface to obtain absorbance values.

6.2.2.5 UV-VIS spectroscopy

UV-VIS spectroscopy measurements are carried out using UV-2450, Shimadzu spectrometer. Samples are prepared similar to those for FTIR.

6.2.2.6 FESEM

The hydrogel coated fibers are cleaved and the transverse section is viewed using a field emission scanning electron microscope (JSM-6700F, Jeol) after sputtering with a fine layer of Palladium.

6.2.2.7 Experimental setup

A broadband light source (AS3223-BA2) with emission wavelengths from 1530 nm to 1605 nm is used to interrogate the fiber interferometer at one end and the

transmitted light is recorded by an optical spectrum analyzer (AQ6370, Yokogawa) at the other (Figure 6-1). The PCF segment is fixed between 2 fiber holders in a custom made chamber that allows the immersion of the PCF segment in various test solutions. All spectra are later processed using MATLAB (MathWorks) are plotted using OriginPro 8 (OriginLab).

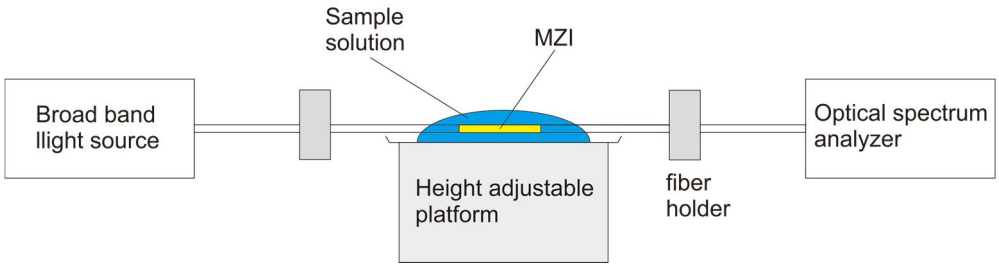

Figure 6-1: Schematic of the MZI heavy metal sensor setup.

6.3 Results and discussion

6.3.1 Principle of operation

The principle of operation of the MZI has been detailed in §5.3.1. Efforts have been made to optimise the splicing procedures to increase sensitivity of the MZI based on collapsed air holes in PCF.

Figure 6-2a shows the spice intersection between SMF (left) and PCF (right) with collapsed air holes in the middle. The length of collapsed air holes region measures approximately 270 µm, almost twice the length used in Chapter 5. The sensitivity to external refractive index change is again demonstrated by immersing the PCF region in glycerol (Sigma-Aldrich) of varying concentration. The interference minima shift towards longer wavelengths (see Figure 6-2b) when refractive index is increased with a sensitivity of approximately 138 nm/RIU in the refractive index range 1.33

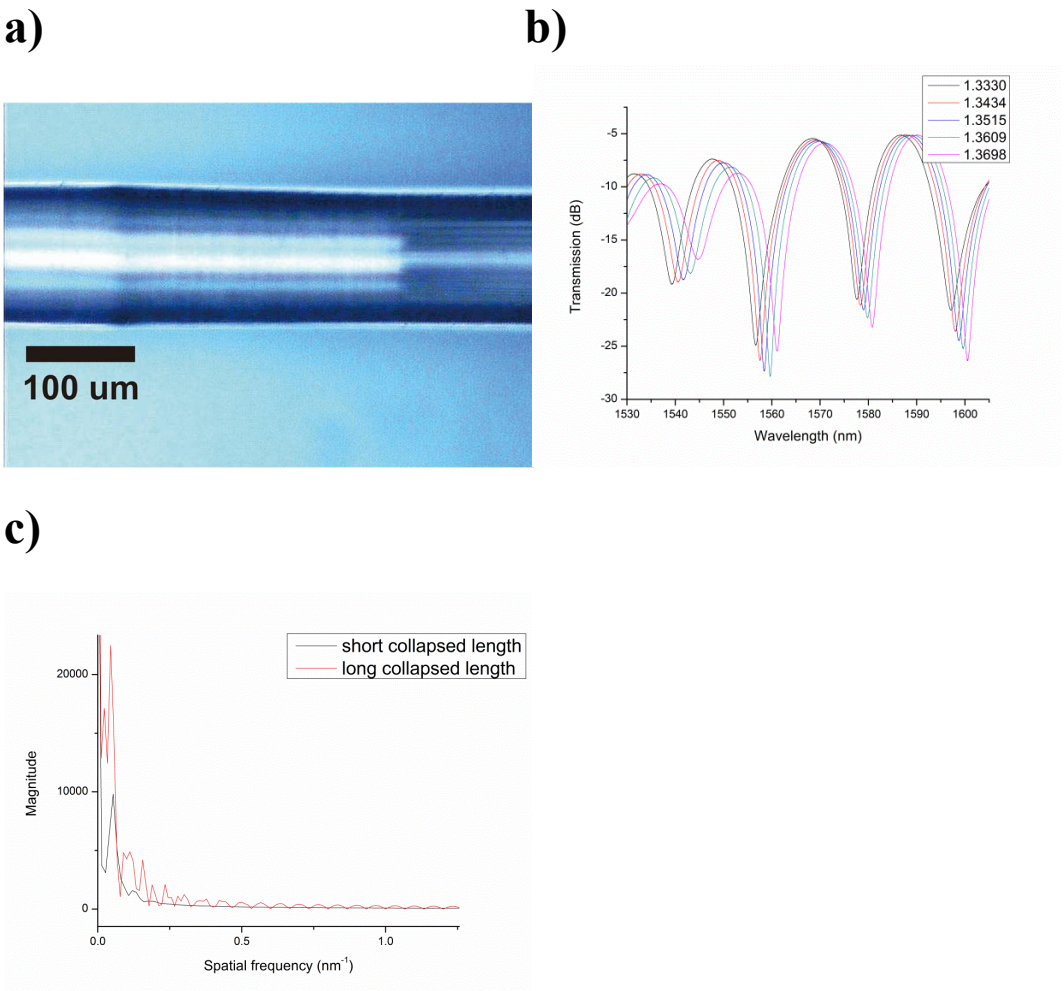

Figure 6-2: (a) Micrograph of a SMF-PCF splice intersection with a middle region of collapsed air holes. (b) Shifting of interference minima towards longer wavelengths when external refractive index is increased. (c) Comparing FFT spectra between a shorter and a longer collapsed length of PCF MZI.

to 1.42 which is higher than a similar length MZI spliced using the method in Chapter 5. A higher fringe visibility is also observed.

A FFT of the spectra of similar length MZI spliced using the different methods are contrasted in Figure 6-2c. A longer collapsed length is capable of exciting more cladding modes as seen in the numerous peaks present in the FFT spectrum. Since spatial frequency, ψ is directly proportional to differential modal group index, Δm_{eff} (see Chapter 5) and higher order cladding modes have lower effective index, n_{eff}, a

longer collapsed region is capable of exciting higher order cladding modes that are more sensitive to the exterior refractive index.

6.3.2 Coating and chemical modification of PVA/PAA hydrogel

PVA is a hydrophilic, biocompatible synthetic polymer with pendant hydroxyl groups and PAA is a homopolymer of acrylic acid (see Figure 6-4). Both polymers are water soluble and are prepared as an aqueous polymer blend form for dip coating.

The coating is heated to induce esterification between hydroxyl groups and carboxyl groups [223] to form cross linkages between strands of PVA and PAA, forming an interconnected network of polymer chains that makes the hydrogel. The process eliminates the need for addition of cross linkers and initiators for polymerisation.

The dip coating process allows a facile fabrication of thin (submicron) hydrogel films on optical fibers. Thin films are essential for responsiveness of hydrogel based sensors with characteristic response time of a hydrogel scaling with the square of its linear dimension [224]. Furthermore, the evanescent field of cladding modes penetrates only several hundreds of nanometers into the exterior and decays exponentially away from the surface, thus thicker hydrogels do not increase sensitivity but degrades response time of the sensor.

The thickness of the hydrogel film can be controlled by composition of the polymer blend and speed of withdrawal of fiber from polymer blend. For a 10 wt % polymer blend consisting PVA:PAA in a 12:6 wt ratio that is dip coated at 100 mm/min and heated at 130 ^{o}C for 30 mins, the thickness of the hydrogel film, measured using FESEM is 881 ± 19 nm (see Figure 6-3a). A thinner hydrogel

coating is obtained using less concentrated polymer blend. Hydrogel film of similar PVA:PAA wt ratio but of 5 wt % total prepared similarly measures 155 ± 5 nm in thickness (see Figure 6-3b) while yet a thinner film measuring 62.3 ± 8.7 nm is obtained from 3 wt % polymer blend (see Figure 6-3c).

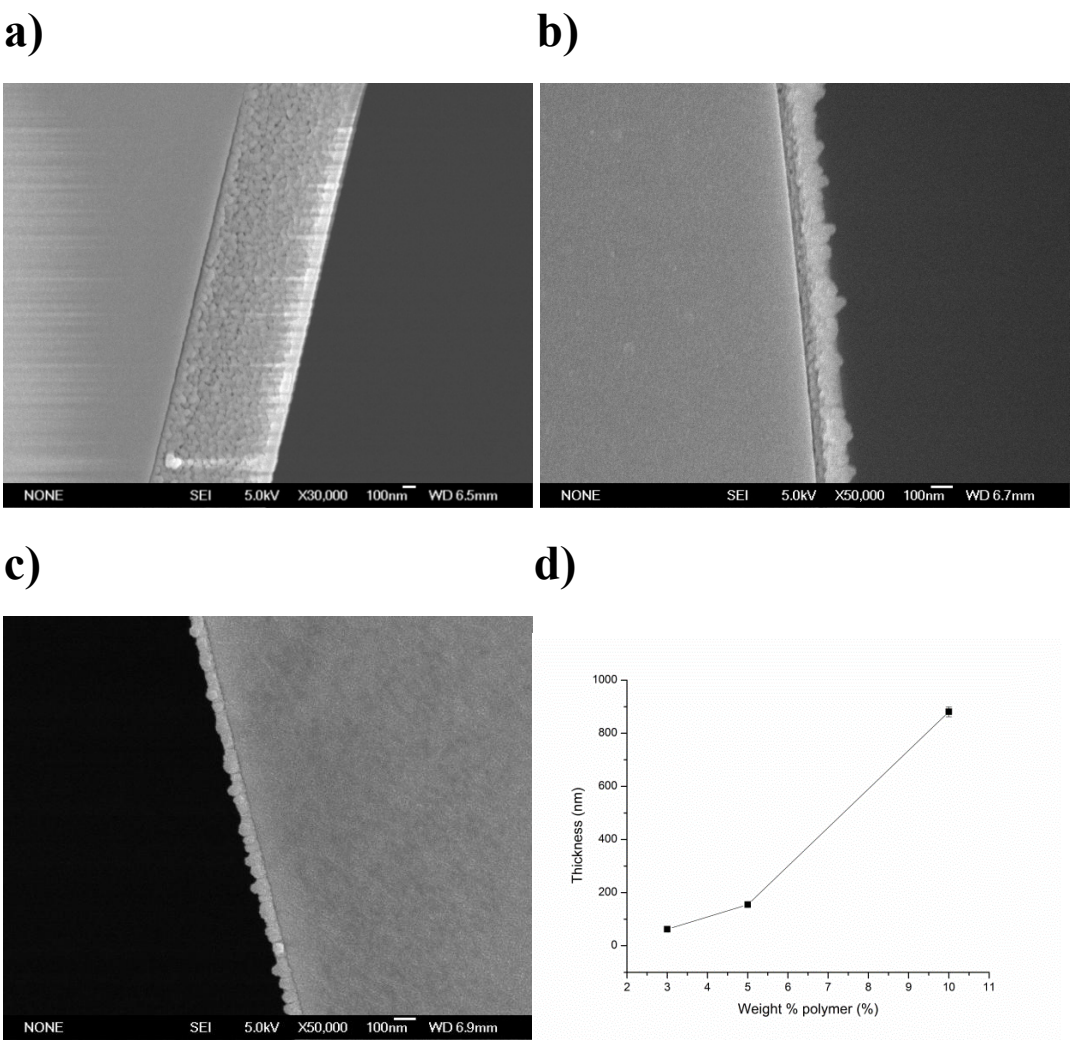

Figure 6-3: FESEM micrograph of 12:6 wt % (a) 10 wt % total (b) 5 wt % total (c) 3 wt % total PVA/PAA hydrogel on optical fiber cross linked at 130 °C for 30 min (d) Plot of hydrogel thickness versus weight percent of polymer blend used for coating.

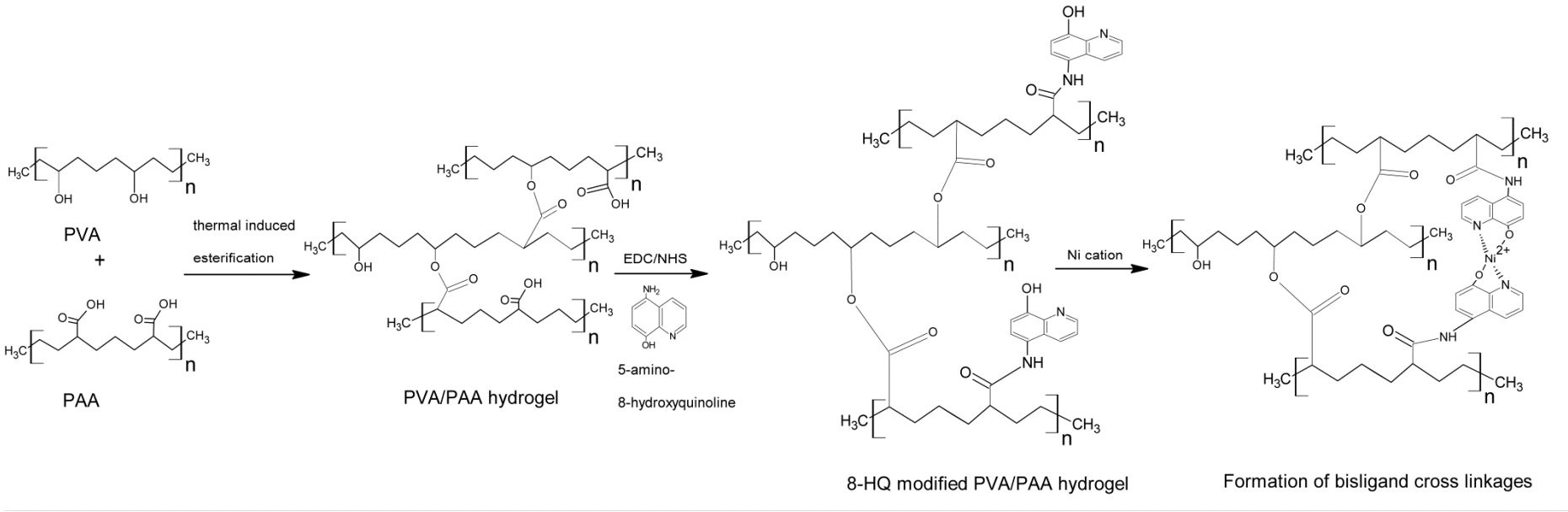

Figure 6-4: Illustration of PVA/PAA hydrogel formation, modification and formation of cross linkage in presence of Ni^{2+}.

The chemical properties of the PVA/PAA hydrogel are investigated using ATR-FTIR. Figure 6-5a shows the PVA/PAA blend prior to cross linking, after cross linking and after chemical modification with 8-hydroxyquinoline.

Strong absorbance peak at ~1705 cm^{-1} is assigned to C=O stretching from the carboxyl group of PAA. Absorbance around 1440 cm^{-1} is attributed to CH_2 and CH_3 deformation bending and absorbance around 1410 cm^{-1} is assigned to OH bend from alcohol groups on PVA. C-O stretch arising from alcohol and carboxyl groups contributes to absorbance in the 1250 cm^{-1} to 1040 cm^{-1} region.

Upon thermal induced cross linking, a decrease in intensity of peak at ~1705 cm^{-1} is observed as carboxyl groups are consumed in the esterification process.

The abundance of carboxyl groups in PVA/PAA hydrogel allows for easy tethering of amino-terminated chemical receptors through amide covalent bonding via EDC/NHS coupling. The efficiency of the coupling process is maximized here in a two-step reaction in which NHS ester formation is first carried out at pH 6 and subsequent reaction with amine group at pH 7.3. 5-amino-8-hydroxyquinoline is chemically immobilized within the PVA/PAA hydrogel and verified via ATR-FTIR and UV-VIS spectroscopy.

New ATR-FTIR absorbance peaks at ~1651 cm^{-1} and ~1539 cm^{-1} are observed with further decrease in the ~1705 cm^{-1} peak after modification of the hydrogel with 5-amino-8-hydroxyquinoline. These correspond to C=O stretch of amide bond and N-H bend of secondary amide bond respectively.

UV-VIS spectroscopy of chemically modified PVA/PAA hydrogel in Figure 6-5b clearly shows the dual absorption bands of 8-hydroxyquinoline arising from n→π* electron transition within the aromatic compound [225].

a)

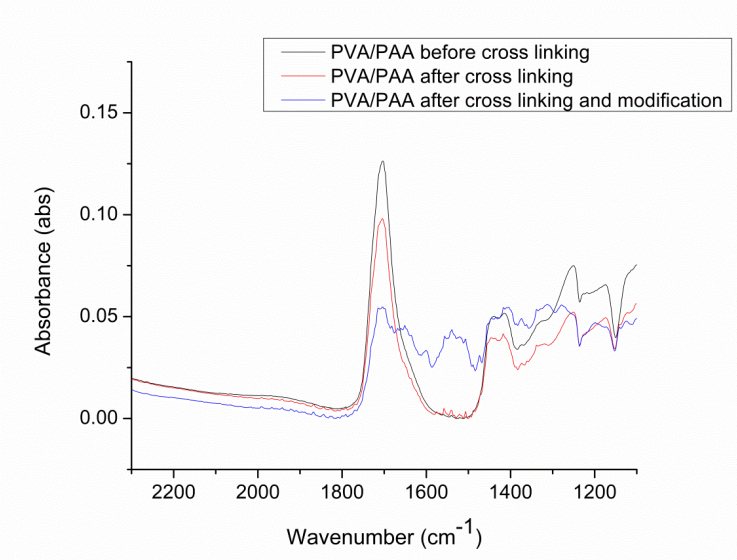

b)

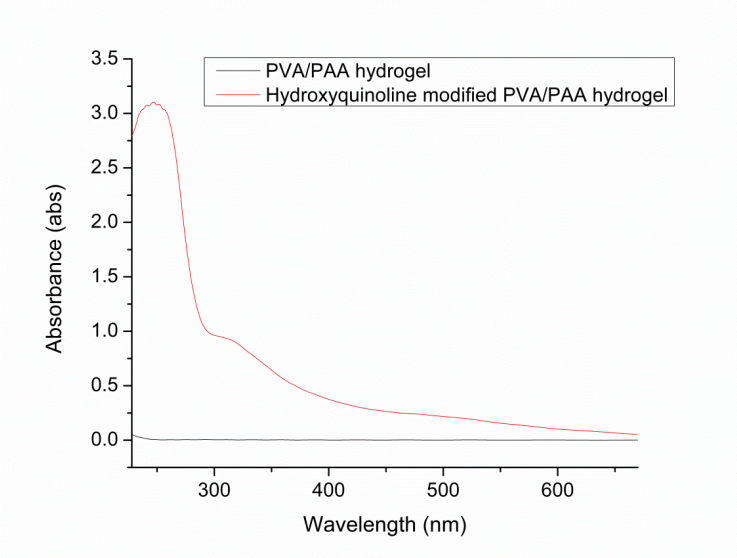

Figure 6-5: (a) ATR-FTIR spectra of 12:6 wt % PVA/PAA blend before cross linking, after thermal induced cross linking at 130 °C for 30 min and after chemical modification with 5-amino-8-hydroxyquinoline using EDC/NHS coupling (b) UV-VIS spectrograph of similar hydrogel before and after chemical modification with 5-amino-8-hydroxyquinoline.

6.3.3 pH responsiveness of PVA/PAA hydrogel coated MZI

The unmodified PVA/PAA hydrogel is inherently pH responsive, exhibiting large swelling and deswelling in response to pH and has been used in various pH sensing applications [214, 226]. The pH responsiveness arises from weakly acidic carboxyl groups that deprotonate above its pKa value of ~ 4.2. The increased charge density leads to swelling of hydrogel by electrostatic repulsion between similarly charged carboxylate groups or osmotic pressure due to diffusion of counter ions from the solution into the hydrogel matrix to ensure charge neutrality.

The pH responsiveness of the unmodified PVA/PAA on our fiber MZI is tested in phosphate buffered saline with pH adjusted using aqueous hydrochloric acid or sodium hydroxide (see Figure 6-6). pH measurement is carried out using glass electrode pH meter (3510, Jenway). Swelling/deswelling corresponds to refractive index decrease/increase at the fiber surface, leading to spectral shift. pH sensitivity of 3.14 nm/pH is obtained between pH 3 to pH 5 using a linear regression line. The minimum detectable pH change, defined as 3 times the background, is 0.02. The apparent pKa was fitted to be 4.23.

pH response is tested again after modification of PVA/PAA hydrogel with ethanolamine using similar EDC/NHS coupling reaction. The reaction consumes carboxyl groups and presents an uncharged hydroxyl group. As a result, the ethanolamine modified gel shows decreased pH response due to decreased swelling/deswelling. The efficiency of EDC/NHS coupling minimises cross sensitivity to pH and ionic concentration after the PVA/PAA hydrogel has been functionally modified.

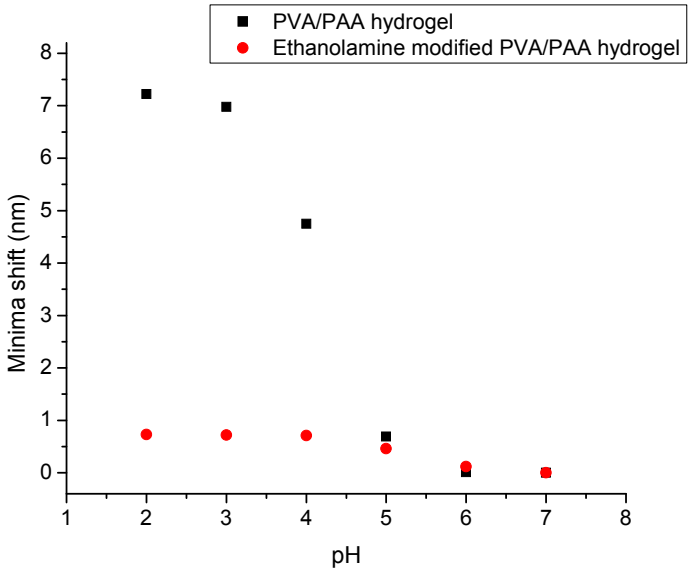

Figure 6-6: pH response of sensor with PVA/PAA hydrogel coating before and after ethanolamine modification. Minima shift is with respect to local reflection minima position at pH 7.

6.3.4 Ni^{2+} responsiveness of PVA/PAA hydrogel coated MZI

The 8-hydroxyquinoline (8HQ) modified PVA/PAA hydrogel based interferometer sensor is tested in varying concentration of $NiCl_2$ in pH 6.7 2-(N-morpholino)ethanesulfonic acid buffer with 150 mM of sodium chloride added to keep ionic concentration relatively constant. Figure 6-7 depicts 8HQ modified sensor response and that of the ethanolamine modified sensor. All readings are recorded after the sensor has equilibrated to the sample solution which typically takes approximately 10 mins.

The interference fringes show a consistent shift towards longer wavelength when Ni^{2+} concentration is increased. The same effect is not observed for the ethanolamine modified sensor. 8HQ is a quinoline derivative with excellent metal coordination ability resulting in its wide use as bidentate chelating agent in many analytical and separation applications [227,228]. It forms a thermodynamically stable complex with divalent metal through a covalent bond to Oxygen and a coordination bond to

Nitrogen. At higher 8HQ concentration, the 8HQ-Metal complex can chelate with another 8HQ to form a biligand complex that encloses the metal ion within the confinement of the Nitrogen and Oxygen atoms (see Figure 6-3). The chelate stability constants for the monoligand and biligand complex are extraordinarily high, thus complex formation could occur in trace metal levels as low as parts per 10^9 [227]. For Ni^{2+}, the stability constants have been found to be 11.65 and 10.4 [229].

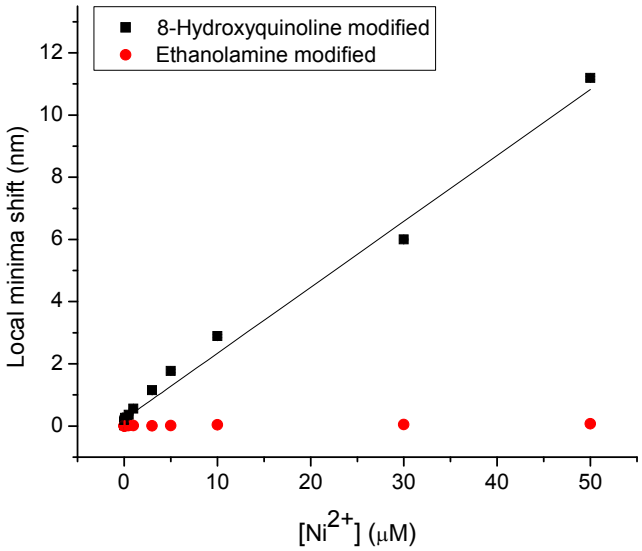

Figure 6-7: Local minima shift of 8-hydroxyquinoline modified sensor versus ethanolamine modified sensor in pH6.70 MES buffer solution of varying Ni^{2+} concentration.

The sensor utilises 8HQ as a Ni^{2+} receptor. Biligand complex formation forms additional cross linkages within the hydrogel, amplifying interactions at the molecular level to a bulk gel volume decrease with increase in refractive index at the fiber sensing surface. The LOD, defined as the minimum concentration of Ni^{2+} that can be detected above 3 times the background signal, of the 8HQ modified sensor is 1 nM, with a sensitivity of 0.214 nm/μM. The LOD is lower than recommended standard of 0.07 ml/L (1.19 μM) set by the World Health Organisation for drinking water [230].

a)

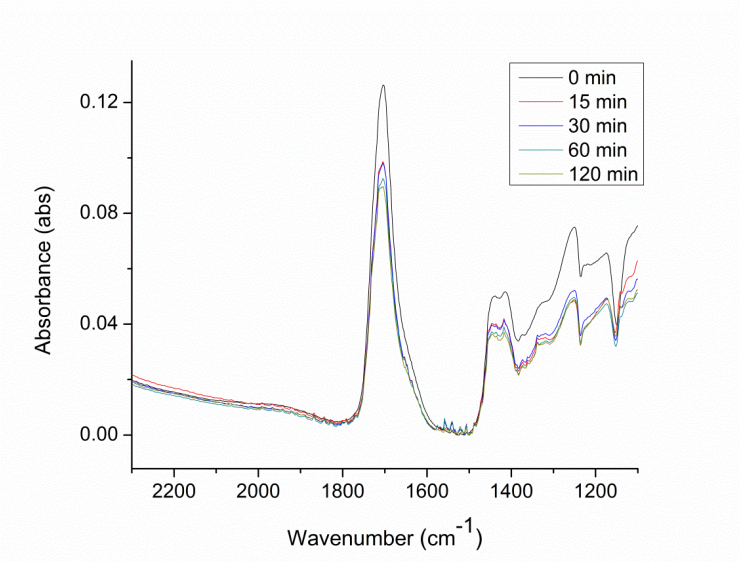

b)

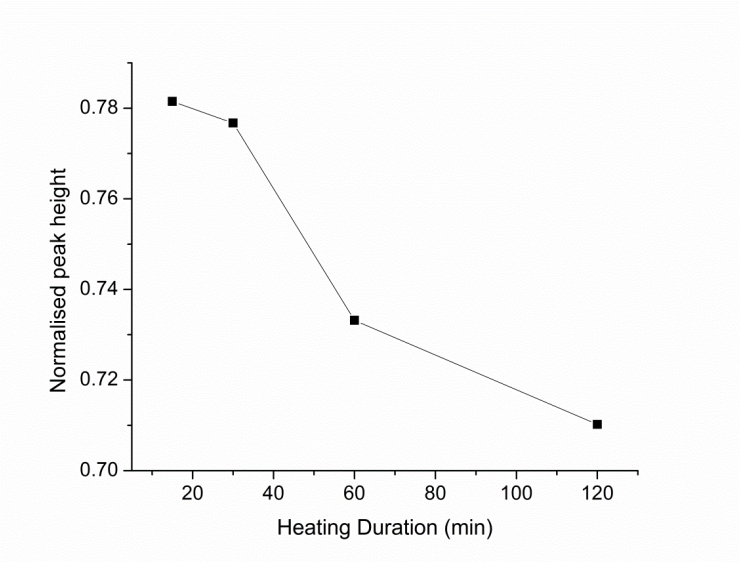

Figure 6-8: (a) ATR-FTIR spectra of 12:6 wt % PVA/PAA blend heated at 130 °C for varying durations. (b) Ratio of the ~1705 cm^{-1} peak height normalised to the peak height when heating is not performed.

6.3.5 Effect of cross linking on sensitivity

Cross linkages within the hydrogel exert a retractile force that opposes osmotic pressure, enabling the hydrogel network to swell without dissolution [91]. The degree of cross linking is an important parameter of the hydrogel apart from its composition and type of cross linking, and affects its equilibrium swell state. A highly cross linked hydrogel exhibits a smaller degree of swelling and a slower solute diffusion rate due to smaller mesh size [231].

The extent of cross linkages within the PVA/PAA hydrogel can be easily modified by the hydrogel composition, heating temperature and heating duration. An increase in heating duration, while keeping temperature constant, increases extent of cross linkages. This is empirically verified in the ATR-FTIR spectra of hydrogel prepared from a 12:6 wt% PVA/PAA blend prepared at 130 ^{o}C for varying period of time (15 min to 120 mins).

Samples heated for less than 15 min are not investigated as they have shown significant loss in mass upon immersion in water, indicating an unstable gel structure. The extensive cross linking in samples heated to 60 min and 120 min is also evident in FESEM where they form thinner, more compact gel films measuring 696 ± 11 nm and 567 ± 13 nm respectively (see Figure 6-9).

The decrease in thickness when coating is heated below 30 mins is attributed to the significant loss in materials due to the low extent of cross linking.

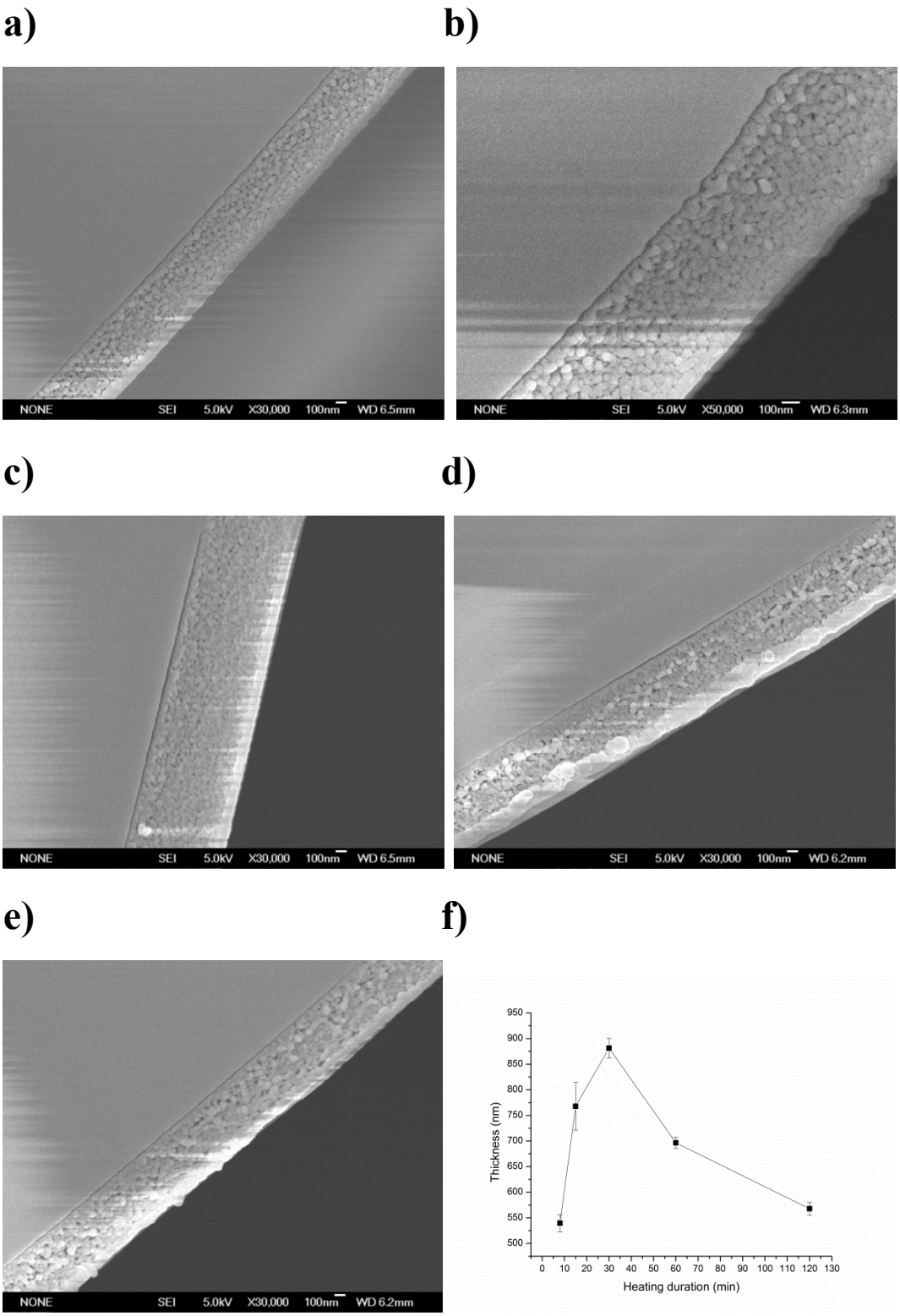

Figure 6-9: SEM micrograph of hydrogel film cross linked at 130 °C for (a) 8min, (b) 15 min, (c) 30 min, (d) 60 min, (e) 120 min. All samples are prepared from 12:6 wt % PVA:PAA (10 wt % total) polymer blend. (f) Plot of hydrogel thickness versus heating duration.

The sensor performance of varying degree cross linked gel is investigated and shown in Figure 6-10. As expected, sensor with gel cross linked for 60 and 120 min show significant decrease in sensitivity due to a reduced swell state. Interestingly, 15 min cross linked sensor shows poorer performance compared to one cross linked for 30 min. This may be attributed to poorer adherence of the hydrogel film on the optical fiber surface.

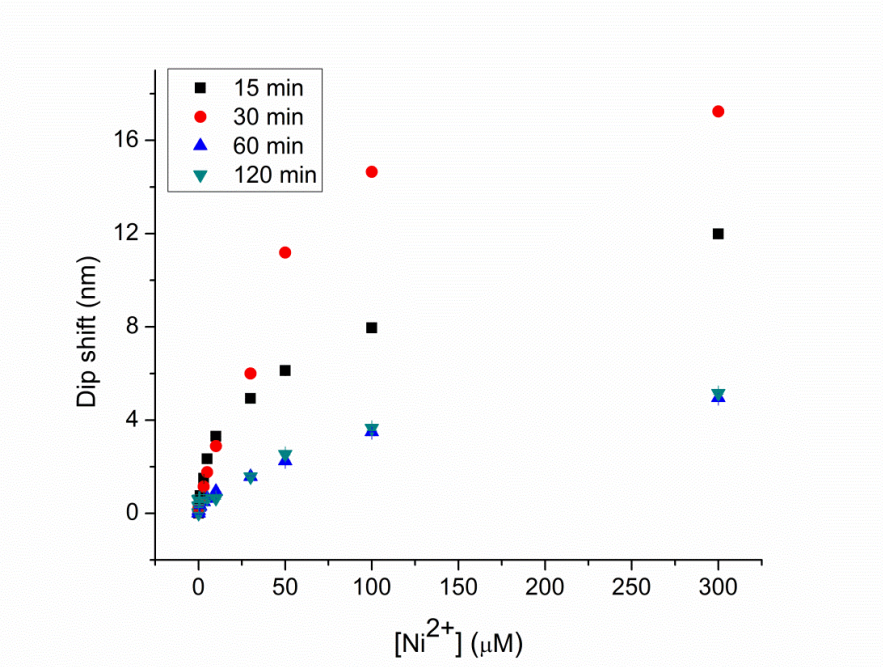

Figure 6-10: Performance of sensors with varying degrees of cross linking.

6.3.6 Effect of composition on sensitivity

The effect of composition of the PVA/PAA hydrogel was also investigated. Keeping total polymer content in the polymer content constant (10 wt %), the PVA/PAA wt ratio was varied 12:3, 12:4.5, 12:6, 12,7.5 and 12:9, corresponding to hydroxyl to carboxyl group ratios of approximately 7, 4.6, 3.5, 2.8 and 2.3 respectively. All gels are cross linked at 130 ^{o}C for 30 min.

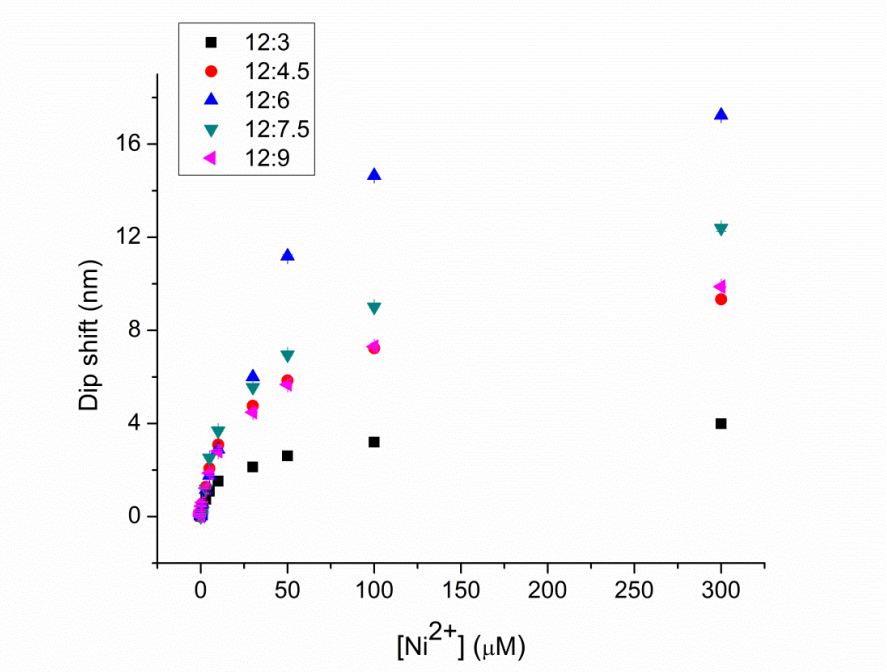

Figure 6-11: Performance of sensors with varying PVA:PAA ratio.

Figure 6-11 shows the performance of sensor with gel of varying PVA/PAA ratio. Sensitivity is increased as PVA/PAA ratio is increased from 12:3 to 12:6, resulting from the increased immobilisation of 8HQ within the hydrogel. This is verified from ATR-FTIR by monitoring the N-H bend peak (~1539 cm^{-1}) in Figure 6-12. A general increase in absorbance is observed as the proportion of PAA is increased.

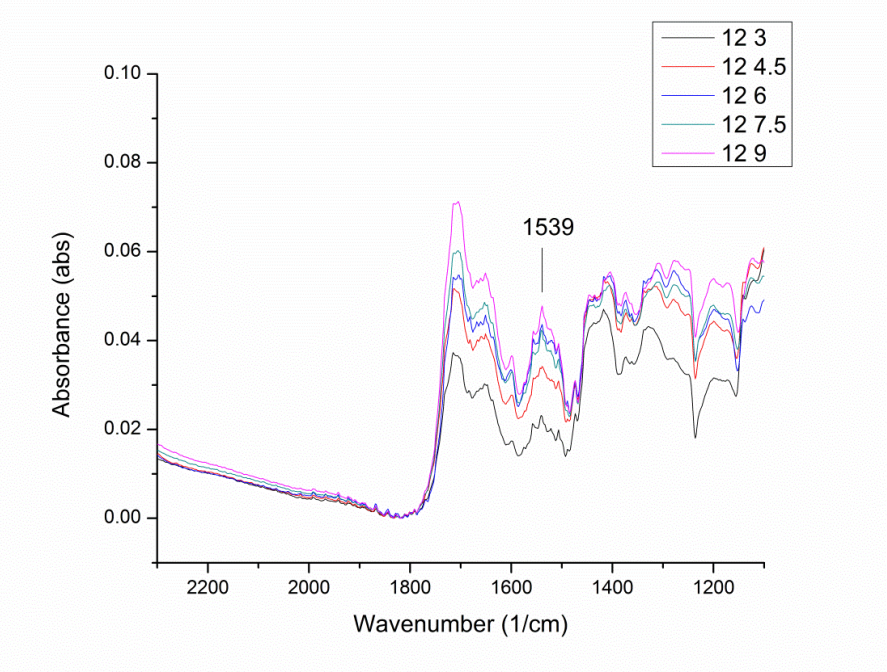

Figure 6-12: ATR-FTIR of 8HQ modified hydrogel of varying PVA:PAA ratios.

Despite a high concentration of immobilised 8HQ, the 12:9 PVA/PAA sensor shows poorer sensitivity. This is attributed to the increased degree of cross linking as seen in the much decreased carboxyl peak in ATR-FTIR after thermal cross linking (see Figure 6-13 and Table 6-1).

Table 6-1: Comparison of the carboxyl peak height in PVA/PAA hydrogels of varying composition before and after 30 mins of heating at 130 °C and the amide peak after 8HQ modification.

PVA: PAA (wt %)	Peak height at 1705 cm^{-1} (abs)		Ratio	Peak height at 1539 cm^{-1} (abs)
	Before heating	After heating		
12:3	0.0703	0.0552	0.785206	0.0202
12:4.5	0.0934	0.0723	0.77409	0.0342
12:6	0.1263	0.0981	0.776722	0.0437
12:7.5	0.1233	0.0934	0.757502	0.0425
12:9	0.1413	0.0764	0.540694	0.0478

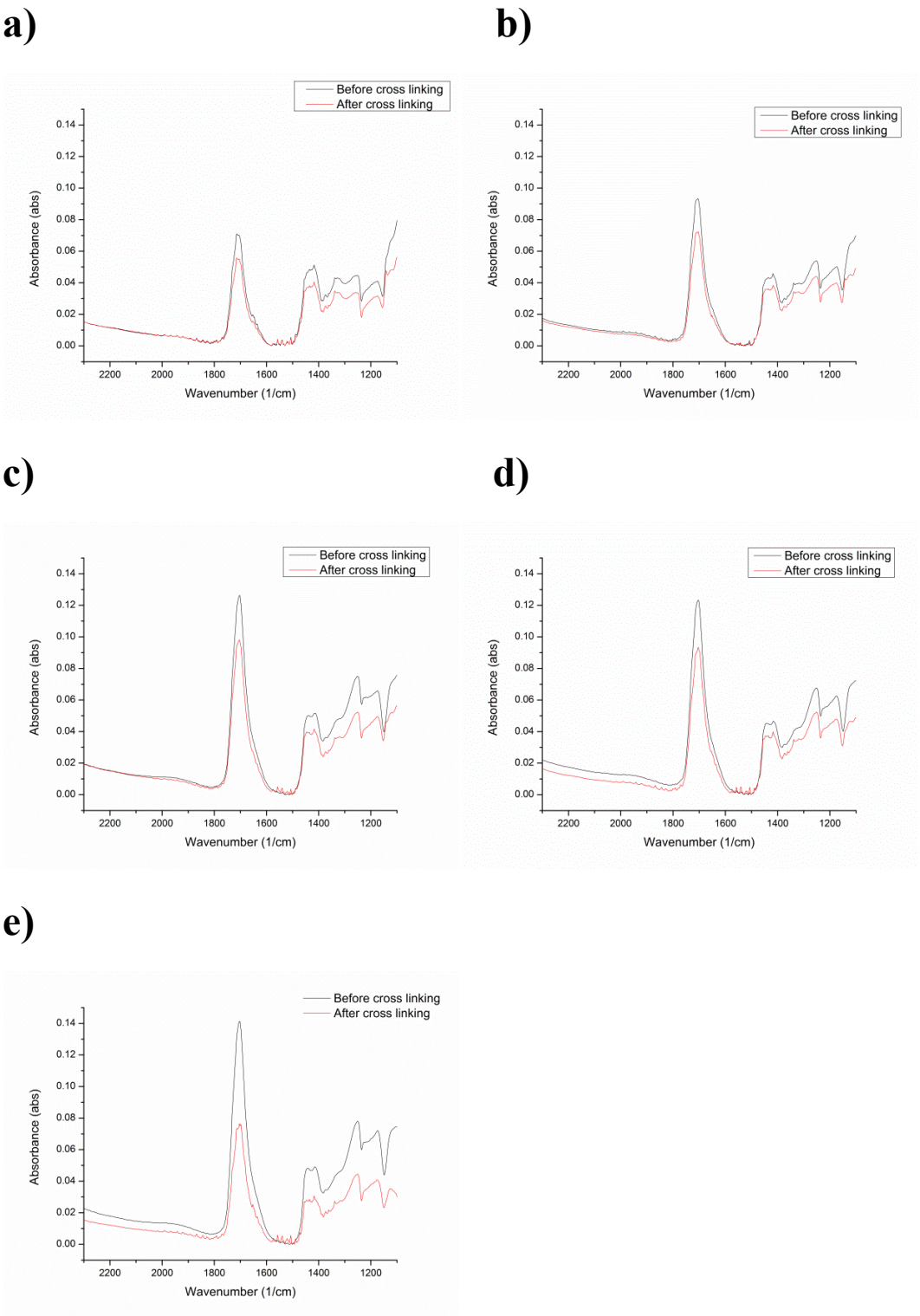

Figure 6-13: ATR-FTIR spectra of PVA/PAA (a) 12:3, (b) 12:4.5, (c) 12:6, (d) 12:7.5, (e) 12:9 wt % before and after cross linking.

6.3.7 Specificity of 8HQ and versatility of the sensor

The specificity of 8HQ is poor with the ligand able to form complexes with many metals like Mn^{+}, Co^{2+}, Cu^{2+}, Zn^{2+} with varying degrees of stability [229]. However, chelating agents that bind specific metals have been an intense area of research [222] and the PVA/PAA hydrogel offers a flexible platform for immobilising these ligands of higher specificity. The PVA/PAA hydrogel can also be used for sensing of other chemical species through immobilisation of various aminated receptors like DNA, proteins, enzymes, aptamers, etc.

6.4 Chapter conclusions

Responsive hydrogels exhibiting volume or phase change in response to specific stimuli have increasingly been used as sensors. We demonstrated the use of such responsive hydrogel on a fiber interferometer platform for sensing small chemical species like heavy metal cations.

The sensing PVA/PAA hydrogel film offers tremendous ease in coating thin films on optical fiber via simple dip coating without need for additional cross linkers and polymerisation initiators. The carboxyl groups on PAA offer efficient coupling to a variety of aminated receptors using carbodiimide coupling to realise a myriad of sensing possibilities. The biocompatibility of both PVA and PAA also makes the proposed sensing film suitable for in-vivo applications.

Sensitivity of the PVA/PAA is affected by the PVA/PAA ratio and duration of heat induced esterification which controls the degree of cross linking and the maximum amount of receptors that can be immobilised.

The Ni^{2+} sensor demonstrates good sensitivity and LOD adequate for continuous monitoring of drinking water. The presence of Ni^{2+} increases degree of cross linkages within the hydrogel and increases its refractive index, leading to phase shift in the interferogram. Ni^{2+} concentration is monitored by the shifting of local interference minima with a sensitivity of 0.214 nm/μM and limit of detection of 1 nM. Specificity, however, can be improved by using more specific receptors.

Chapter 7

Conclusions and future work

7.1 Summary of the investigation

The potential of optical fibers in chemical/biochemical sensing is recognized. Whilst a vast array of optical techniques exist, wavelength based techniques like those based on plasmonic resonance and interferometry stand out with their high sensitivity, label free approach and are relatively free from problems that plagued intensity based techniques based on luminescence probes. Using responsive polymers as the sensitive materials, a sensor device that is miniature in size, low cost, robust, and capable of real time and multiplex sensing with limitless sensing possibilities can be achieved.

The thesis begins with work on an optical fiber refractometer based on LSPR. By using a short segment of PCF, cladding modes excite surface immobilized AuNPs in stark contrast to conventional core mode excitation. Simple splicing and chemical surface modification are used to fabricate the sensor, eradicating the need for cladding removal using chemical etching that is both hazardous and compromises mechanical integrity of the sensor. The LSPR sensor exhibits good linearity (R^2 = 0.9988) in normalized transmitted intensity with high sensitivity of -731 %/RIU in response to external bulk refractive index change in the region 1.33 RIU to 1.43 RIU with a limit of detection of 1.76 x 10^{-5} RIU and is highly reproducible, making it useful for biological and chemical sensing applications.

The basic setup of the LSPR fiber refractometer is then used as a pH sensor in Chapter 4 by coating of a unique pH responsive PEM consisting of Chitosan and PSS onto the fiber surface by LBL technique. Both Chitosan and PSS are biocompatible and the former, in particular, is of immense research due to its abundance of amino groups that allow facile modification of chemical properties for a wide array of applications including drug delivery and tissue engineering. AuNPs is synthesised in PSS solution and becomes embedded within the PEM during LBL assembly. The principle of the sensor lies in the pH dependent swelling/deswelling of the PEM that alters interplasmonic coupling between embedded AuNPs, resulting in increased/decreased extinction. Both transmission and reflection based sensors are tested and pH response can be modelled by the extended Henderson-Hasselbach equation. Both show pH responsiveness within the physiological range of pH 6.5 to pH 8 with similar sensitivity. However, the reflection based sensor is much easier to fabricate and demonstrates potential for in-vivo biological applications.

Fiber interferometers are also of interest for chemical sensing. Chapter 5 proposes a double-pass Mach Zehnder fiber interferometer for pH sensing. The double-pass MZI possesses a higher Q factor than its single-pass counterpart, thus possesses higher resolution. pH responsive poly(HEMA-co-DMAEM) hydrogel is coated onto the fiber by free radical initiated polymerization and the response tested in PBS. The pH sensor exhibits a linear response within the physiological relevant pH range pH 6.75 to 8.25 ($R^2 = 0.986$) with sensitivity of 1.71 nm/pH and LOD of pH 0.004. The sensor is applied to the monitoring of culture media of A375 human melanoma cells and provides insights into cell proliferation and extracellular pH. Extracellular pH is observed to fall and plateau at ~pH 6.8.

With initial success in hydrogel based fiber interferometer sensor, we seek a generalized approach in fabricating such sensors in Chapter 6 through use of PVA/PAA hydrogel and demonstrated it for sensing of small chemical species like Ni^{2+}. The PVA/PAA offers tremendous ease in obtaining thin films on optical fiber via simple dip coating without need for additional cross linkers and polymerisation initiators. The carboxyl groups on PAA offer efficient coupling to a variety of aminated receptors using carbodiimide coupling to realise a myriad of sensing possibilities. The biocompatibility of both PVA and PAA also makes the proposed sensing film suitable for in-vivo applications. Sensitivity of the PVA/PAA is affected by the PVA/PAA ratio and duration of heat induced esterification which controls the degree of cross linking and the maximum amount of receptors that can be immobilised. The optimal PVA/PAA hydrogel is fabrication from a 12:6 wt % ratio and cross linked at 130 ^{o}C for 30 min. By modifying the PVA/PAA hydrogel with hydroxyquinoline, the sensor is able to detect Ni^{2+} with good sensitivity 0.214 nm/μM and LOD 1nM adequate for continuous monitoring of drinking water.

7.2 Suggestions for future work

7.2.1 pH microenvironment modulator

One avenue for future work would be integration of our sensors into a system for real life applications. For instance, there is ongoing investigation on integrating our fiber optic pH interferometric sensor (reported in Chapter 5) into a pH microenvironment modulator as shown in Figure 7-1.

The proposed pH microenvironment modulator will play a role in unraveling the phenomenon of acid-mediated tumor invasion. This local invasion of malignant tumors into normal tissues is a major problem plaguing many advanced stage cancer patients resulting in substantial morbidity and mortality. While it is generally acknowledged that tumor tissue extracellular pH is acidic (~pH 6.6 to 7.0) compared to normal tissue (~pH 7.2 to 7.4) due to hypoxia and increased glycolysis, it has recently been suggested that the acidic pH may not merely be a by-product but a desired state pursued by cancer cells [232, 233]. Various evidence has emerged of the crucial role pH played in driving tumor progression including:

- Creation of a selection pressure for tumor cells since normal cells are unable to survive the acidic pH
- Promotion of angiogenesis [234]
- Degradation of extracellular matrix, thereby increasing invasiveness [235]
- Inhibition of cytotoxic lymphocytes [236]

The proposed pH microenvironment modulator takes into advantage the miniature size, stability, robustness of the reported fiber optic pH meter for in vitro measurement of extracellular pH. The pH information is fed to a computer running a system control software like Labview that, depending on the pH value, instructs a syringe pump to eject bicarbonate solution into the culture media, thereby maintaining the extracellular pH. The proposed system will locally target and buffer the tumor acid microenvironment in real time and is easily transferable to in-vivo applications and is thus a potentially invaluable treatment strategy in limiting local invasion in cancer patients.

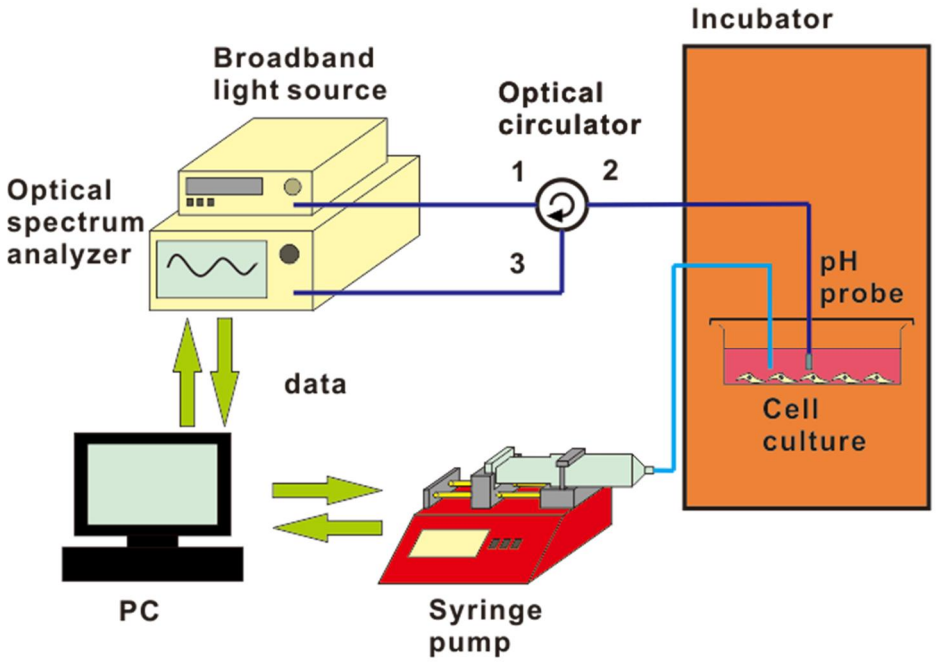

Figure 7-1: Schematic of the proposed pH microenvironment modulator.

7.2.2 Improving PVA/PAA based sensors

A versatile sensing platform is suggested in Chapter 6 utilizing a fiber optic Mach Zehnder interferometer coated with PVA/PAA hydrogel. While it is suggested that the platform could be easily adapted for a wide range of sensing by immobilizing different aminated receptors into the PVA/PAA hydrogel, we did not prove this beyond the sensing of Ni^{2+} by immobilized hydroxyquinoline.

A molecule that of particular sensing interest is glucose, with current researches focusing on the continuous, real time in-vivo measurement of glucose on diabetic patients [237]. Since PVA/PAA gel is biocompatible, it will be interesting to investigate how our sensor would fare in glucose sensing. Already, three common strategies have been suggested including the immobilization of enzyme, glucose oxidase [238], boronic acid groups [239] and concanavalin A [240]. Glucose oxidase is advantageous over the others owning to its specificity for glucose which it

catalyses its conversion to gluconic acid. The PVA/PAA hydrogel is perfect for the sensing owning to its inherent acidic-dependent swelling behavior. The lowering of pH from gluconic acid is expected to deswell the gel, nevertheless, optimization of the extent of cross linking and availability of free carboxyl groups will need to be performed.

The response time of the PVA/PAA hydrogel can be improved by designing its morphology. A plausible technique could be formation of macro pores within the hydrogel structure by using carbonate induced carbon dioxide air pockets or sacrificial colloidal beads that are chemically removed after gel formation. The porous structure would enhance diffusion driven molecular exchange between the hydrogel matrix and the external environment.

7.2.3 Incorporation of nanomaterials and techniques

There is a trend in optical sensing in the use of nanomaterials to improve performance. Metallic nanoparticles, for instance, have been used to amplify fluorescence by providing a strong local field and to help scatter fluorescence signal to improve far field detectable signals [241]. It is felt that many of these materials and techniques can also be transferred to fiber optics.

PVA/PAA hydrogel (Chapter 6) could be synthesized as micro or nanobeads via spray on technique [242] or by synthesis in an organic phase and self- assembled onto optical fiber by electrostatic forces. The colloidal form provides a large surface area to volume ratio that improves response time.

The LBL technique remains the most reliable technique of ultra-thin film formation of controllable thickness, architecture and properties on optical fibers,

however, the traditional polyelectrolyte multilayers system has found limited sensing applications besides pH sensing and long term stability of these films is suspect due to physical forces that hold the film. New materials suitable for LBL using forces other than electrostatics have been investigated and long term stability has been improved through cross linking after the initial LBL process. A possible versatile platform much like the PVA/PAA hydrogel (Chapter 6) is the PAA/polyacrylamide (PAAm) system [243]. The PAA/PAAm multilayers can be formed LBL assembly from pH 3 solutions of PAA and PAAm with hydrogen bonds holding the multilayers. Thermal crosslinking can be induced by imidization reaction between carboxyl groups (PAA) and amide groups (PAAm).

Author's publications

Publications related to the thesis

1. Tou, Z.Q., et al. (2012) "Fiber Optic Refractometer Based on Cladding Excitation of Localized Surface Plasmon Resonance." IEEE Photonics Technology Letters. **25**(6): p. 556-559.

2. Tou, Z. Q., C. C. Chan, et al. (2014). "A fiber-optic pH sensor based on polyelectrolyte multilayers embedded with gold nanoparticles." Measurement Science & Technology **25**(7).

3. Tou, Z. Q., C. C. Chan, et al. (2014). "Double-pass Mach-Zehnder fiber interferometer pH sensor." Journal of Biomedical Optics **19**(4).

4. Tou, Z. Q., T. W. Koh, et al. (2014). "Poly(vinyl alcohol) hydrogel based fiber interferometer sensor for heavy metal cations." Sensors and Actuators B-Chemical **202**: 185-193.

Co-authored publications

1. Tan, Y. C., Z. Q. Tou, et al. (2014). "Continuous refractive index sensing based on carbon-nanotube-deposited photonic crystal fibers." Sensors and Actuators B-Chemical **202**: 1097-1102.

2. Chen, L.H., et al. (2013). "Fabry-Perot fiber-optic immunosensor based on suspended layer-by-layer (chitosan/polystyrene sulfonate) membrane." Sensors and Actuators B-Chemical. **188**: p. 185-192.

3. Chen, L.H., et al. (2013). "Label-free fiber-optic interferometric immunosensors based on waist-enlarged fusion taper." Sensors and Actuators B-Chemical. **178**: p. 176-184.

4. Wong, W.C., et al. (2011). "Highly sensitive miniature photonic crystal fiber refractive index sensor based on mode field excitation." Optics Letters. **36**(9): p. 1731-1733.

5. Wong, W.C., et al. (2011). "Compact Photonic Crystal Fiber Refractometer Based On Modal Interference." 21st International Conference on Optical Fiber Sensors, W.J. Bock, J. Albert, and X. Bao, Editors.

Bibliography

[1] Hulanicki, A., S. Glab, et al. (1991). "Chemical Sensors Definitions and Classification." Pure and Applied Chemistry **63**(9): 1247-1250.

[2] John A. Buck. (2004). "Fundamentals of Optical Fibers 2nd Edition" Wiley-Interscience: Pages 51-87

[3]Russell, P. (2003). "Photonic crystal fibers." Science **299**(5605): 358-362.

[4] Brabec, T. and F. Krausz (2000). "Intense few-cycle laser fields: Frontiers of nonlinear optics." Reviews of Modern Physics **72**(2): 545-591.

[5] Ranka, J. K., R. S. Windeler, et al. (2000). "Visible continuum generation in air-silica microstructure optical fibers with anomalous dispersion at 800 nm." Optics Letters **25**(1): 25-27.

[6] Benabid, F., J. C. Knight, et al. (2002). "Particle levitation and guidance in hollow-core photonic crystal fiber." Optics Express **10**(21): 1195-1203.

[7] Knight, J. C., T. A. Birks, et al. (1996). "All-silica single-mode optical fiber with photonic crystal cladding." Optics Letters **21**(19): 1547-1549.

[8] Cregan, R. F., B. J. Mangan, et al. (1999). "Single-mode photonic band gap guidance of light in air." Science **285**(5433): 1537-1539.

[9] Gauvreau, B., A. Hassani, et al. (2007). "Photonic bandgap fiber-based surface plasmon resonance sensors." Optics Express **15**(18): 11413-11426.

[10] Ghenuche, P., H. Rigneault, et al. (2012). "Hollow-core photonic crystal fiber probe for remote fluorescence sensing with single molecule sensitivity." Optics Express **20**(27): 28379-28387.

[11] Han, Y., M. K. K. Oo, et al. (2010). "Photonic Crystal Fiber as an Optofluidic Platform for Surface-Enhanced Raman Scattering." 2nd Workshop on Specialty Optical Fibers and Their Applications Wsof-2 **7839**.

[12] Yang, X., A. S. P. Chang, et al. (2013). "High sensitivity gas sensing by Raman spectroscopy in photonic crystal fiber." Sensors and Actuators B-Chemical **176**: 64-68.

[13]Wang, H., Q. Wang, et al. (2008). "Measurement technique for methane concentration by wavelength scanning of a distributed-feedback laser." Laser Physics **18**(4): 491-494.

[14] Wu, X.-j., P. Wang, et al. (2009). "Methane Optic Fiber Sensor Network Based on Infrared Spectrum Absorption in Coal Mine." Spectroscopy and Spectral Analysis **29**(9): 2365-2369.

[15] Cubillas, A. M., J. M. Lazaro, et al. (2009). "Gas Sensor Based on Photonic Crystal Fibres in the 2 nu(3) and nu(2)+2 nu(3) Vibrational Bands of Methane." Sensors **9**(8): 6261-6272.

[16] Tao, S. Q. and T. V. S. Sarma (2006). "Evanescent-wave optical CrVI sensor with a flexible fused-silica capillary as a transducer." Optics Letters **31**(10): 1423-1425.

[17] Kneipp, K., H. Kneipp, et al. (1999). "Ultrasensitive chemical analysis by Raman spectroscopy." Chemical Reviews **99**(10): 2957-+.

[18] Campion, A. and P. Kambhampati (1998). "Surface-enhanced Raman scattering." Chemical Society Reviews **27**(4): 241-250.

[19] Khijwania, S. K., V. S. Tiwari, et al. (2007). "A fiber optic Raman sensor for hydrocarbon detection." Sensors and Actuators B-Chemical **125**(2): 563-568.

[20] Lucotti, A., A. Pesapane, et al. (2007). "Use of a geometry optimized fiber-optic surface-enhanced Raman scattering sensor in trace detection." Applied Spectroscopy **61**(3): 260-268.

[21] McDonagh, C., C. S. Burke, et al. (2008). "Optical chemical sensors." Chemical Reviews **108**(2): 400-422.

[22] Leung, A., P. M. Shankar, et al. (2007). "A review of fiber-optic biosensors." Sensors and Actuators B-Chemical **125**(2): 688-703.

[23] Khijwania, S. K. and B. D. Gupta (2000). "Maximum achievable sensitivity of the fiber optic evanescent field absorption sensor based on the U-shaped probe." Optics Communications **175**(1-3): 135-137.

[24] Rao, Y. J. (1997). "In-fibre Bragg grating sensors." Measurement Science & Technology **8**(4): 355-375.

[25] Cong, J., X. M. Zhang, et al. (2002). "Fiber optic Bragg grating sensor based on hydrogels for measuring salinity." Sensors and Actuators B-Chemical **87**(3): 487-490.

[26] Albert, J., L. Y. Shao, et al. (2013). "Tilted fiber Bragg grating sensors." Laser & Photonics Reviews **7**(1): 83-108.

[27] James, S. W. and R. P. Tatam (2003). "Optical fibre long-period grating sensors: Characteristics and application." Measurement Science & Technology **14**(5): R49-R61.

[28] Trouillet, A., E. Marin, et al. (2006). "Fibre gratings for hydrogen sensing." Measurement Science & Technology **17**(5): 1124-1128.

[29] Gordon, J. G. and S. Ernst (1980). "Surface-Plasmons as a Probe of the Electrochemical Interface." Surface Science **101**(1-3): 499-506.

[30] Liedberg, B., C. Nylander, et al. (1983). "Surface-Plasmon Resonance for Gas-Detection and Biosensing." Sensors and Actuators **4**(2): 299-304.

[31] Sharma, A. K., R. Jha, et al. (2007). "Fiber-optic sensors based on surface plasmon resonance: A comprehensive review." IEEE Sensors Journal **7**(7-8): 1118-1129.

[32] Srivastava, S. K., R. Verma, et al. (2012). "Surface plasmon resonance based fiber optic glucose biosensor." Third Asia Pacific Optical Sensors Conference. J. Canning and G. D. Peng. Bellingham, Spie-Int Soc Optical Engineering. **8351**.

[33] Willets, K. A. and R. P. Van Duyne (2007). "Localized surface plasmon resonance spectroscopy and sensing." Annual Review of Physical Chemistry. **58:** 267-297.

[34] Kreibig U, Vollmer M (eds) (1995) "Cluster materials." Springer Berlin Heidelberg New York, p 532

[35] Haes, A. J. and R. P. Van Duyne (2002). "A nanoscale optical blosensor: Sensitivity and selectivity of an approach based on the localized surface plasmon resonance spectroscopy of triangular silver nanoparticles." Journal of the American Chemical Society **124**(35): 10596-10604.

[36] Storhoff, J. J., A. A. Lazarides, et al. (2000). "What controls the optical properties of DNA-linked gold nanoparticle assemblies?" Journal of the American Chemical Society **122**(19): 4640-4650.

[37] Sepulveda, B., P. C. Angelome, et al. (2009). "LSPR-based nanobiosensors." Nano Today **4**(3): 244-251.

[38] Grattan, K.T.V.; Meggitt, B.T. "Optical Fiber Sensor Technology." Chapman & Hall: Orange, CA, USA, 1995.

[39] Lee, B. H., Y. H. Kim, et al. (2012). "Interferometric Fiber Optic Sensors." Sensors **12**(3): 2467-2486.

[40] Sanchez-Barragan, I., J. M. Costa-Fernandez, et al. (2006). "A ratiometric approach for pH optosensing with a single fluorophore indicator." Analytica Chimica Acta **562**(2): 197-203.

[41] Glenn, S. J., B. M. Cullum, et al. (2001). "Lifetime-based fiber-optic water sensor using a luminescent complex in a lithium-treated Nafion (TM) membrane." Analytica Chimica Acta **448**(1-2): 1-8.

[42] Chodavarapu, V. P., D. O. Shubin, et al. (2007). "CMOS-based phase fluorometric oxygen sensor system." IEEE Transactions on Circuits and Systems I-Regular Papers **54**(1): 111-118.

[43] Manivannan, S., A. M. Saranya, et al. (2012). "Single-walled carbon nanotubes wrapped poly-methyl methacrylate fiber optic sensor for ammonia, ethanol and methanol vapors at room temperature." Sensors and Actuators B-Chemical 171: 634-638.

[44] Kharat, H. J., K. P. Kakde, et al. (2008). "Development of PPy-PVS optical fiber ammonia sensor." Optoelectronics and Advanced Materials-Rapid Communications 2(9): 553-560.

[45] Watanabe, T., S. Okazaki, et al. (2010). "A fiber-optic hydrogen gas sensor with low propagation loss." Sensors and Actuators B-Chemical 145(2): 781-787.

[46] Monzon-Hernandez, D., D. Luna-Moreno, et al. (2009). "Fast response fiber optic hydrogen sensor based on palladium and gold nano-layers." Sensors and Actuators B-Chemical 136(2): 562-566.

[47] Shukla, S. K., A. Tiwari, et al. (2009). "Exploring fiber optic approach to sense humid environment over nano-crystalline zinc oxide film." Talanta 80(2): 565-571.

[48] Xiong, Y., Z. B. Ye, et al. (2013). "An integrated micro-volume fiber-optic sensor for oxygen determination in exhaled breath based on iridium(III) complexes immobilized in fluorinated xerogels." Analyst 138(6): 1819-1827.

[49] Renganathan, B., D. Sastikumar, et al. (2011). "Nanocrystalline ZnO coated fiber optic sensor for ammonia gas detection." Optics and Laser Technology 43(8): 1398-1404.

[50] Mariammal, R. N., K. Ramachandran, et al. (2012). "On the enhancement of ethanol sensing by CuO modified SnO_2 nanoparticles using fiber-optic sensor." Sensors and Actuators B-Chemical 169: 199-207.

[51] Hu, X. and S. Tao (2011). "An Optical Fiber H_2O_2-Sensing Probe Using a Titanium(IV) Oxyacetylacetonate Immobilized Nafion Coating on an Bent Optical Fiber Probe." IEEE Sensors Journal 11(9): 2032-2036.

[52] Ohira, S.-I., P. K. Dasgupta, et al. (2009). "Fiber Optic Sensor for Simultaneous Determination of Atmospheric Nitrogen Dioxide, Ozone, and Relative Humidity." Analytical Chemistry 81(11): 4183-4191.

[53] Wu, S., W. Cheng, et al. (2010). "Fiber optic pH sensor based on mode-filtered light detection." Sensors and Actuators B-Chemical 144(1): 255-259.

[54] Segawa, H., E. Ohnishi, et al. (2003). "Sensitivity of fiber-optic carbon dioxide sensors utilizing indicator dye." Sensors and Actuators B-Chemical 94(3): 276-281.

[55] Carter, J. C., R. M. Alvis, et al. (2006). "Fabricating optical fiber imaging sensors using inkjet printing technology: A pH sensor proof-of-concept." Biosensors & Bioelectronics 21(7): 1359-1364.

[56] Warren-Smith, S. C., S. Heng, et al. (2011). "Fluorescence-Based Aluminum Ion Sensing Using a Surface-Functionalized Microstructured Optical Fiber." Langmuir 27(9): 5680-5685.

[57] Long, F., C. Gao, et al. (2011). "Reusable evanescent wave DNA biosensor for rapid, highly sensitive, and selective detection of mercury ions." Biosensors & Bioelectronics 26(10): 4018-4023.

[58] Korposh, S. O., Y. P. Sharkan, et al. (2008). "Response of bacteriorhodopsin thin films to ammonia." Sensors and Actuators B-Chemical 129(1): 473-480.

[59] Qin, H., A. Kukarni, et al. (2011). "Polypyrrole thin film fiber optic chemical sensor for detection of VOCs." Sensors and Actuators B-Chemical 158(1): 223-228.

[60] Zhang, H., A. Kulkarni, et al. (2011). "Detection of Acetone Vapor Using Graphene on Polymer Optical Fiber." Journal of Nanoscience and Nanotechnology 11(7): 5939-5943.

[61] Liu, N., L. Li, et al. (2010). "Silver-embedded zeolite thin film-based fiber optic sensor for in situ, real-time monitoring Hg^{2+} ions in aqueous media with high sensitivity and selectivity." Journal of Materials Chemistry 20(41): 9029-9031.

[62] Yanaz, Z., H. Filik, et al. (2010). "Development of an optical fibre reflectance sensor for lead detection based on immobilised arsenazo III." Sensors and Actuators B-Chemical 147(1): 15-22.

[63] Koshiba, Y., Y. Nakamura, et al. (2010). "Development of a durable fiber-optic oxygen sensor for harsh underground environments." Talanta 82(4): 1495-1499.

[64] Chen, R., A. D. Farmery, et al. (2011). "A fibre optic oxygen sensor for monitoring of human breathing." 2011 International Conference on Optical Instruments and Technology: Optical Sensors and Applications 8199.

[65] Chu, C.-S. and Y.-L. Lo (2008). "Ratiometric fiber-optic oxygen sensors based on sol-gel matrix doped with metalloporphyrin and 7-amino-4-trifluoromethyl coumarin." Sensors and Actuators B-Chemical 134(2): 711-717.

[66] Perrotton, C., N. Javahiraly, et al. (2011). "Fiber optic Surface Plasmon Resonance sensor based on wavelength modulation for hydrogen sensing." Optics Express 19(23): A1175-A1183.

[67] Lin, T.-J. and M.-F. Chung (2009). "Detection of cadmium by a fiber-optic biosensor based on localized surface plasmon resonance." Biosensors & Bioelectronics 24(5): 1213-1218.

[68] Lin, T.-J. and M.-F. Chung (2008). "Using monoclonal antibody to determine lead ions with a localized surface plasmon resonance fiber-optic biosensor." Sensors 8(1): 582-593.

[69] Yang, M., Z. Yang, et al. (2012). "Fiber optic hydrogen sensors with sol-gel WO3 coatings." Sensors and Actuators B-Chemical 166: 632-636.

[70] Dass, S., R. K. Gangwar, et al. (2011). “A Novel Optical Fiber Humidity Sensor Coated with Superhydrophilic Silica Nanoparticles. Optics: Phenomena, Materials, Devices, and Characterization.” Optics 2011: International Conference on Light. P. Predeep, M. Thakur and M. K. R. Varma. 1391.

[71] Wei, X., T. Wei, et al. (2008). "Nano-structured Pd-long period fiber gratings integrated optical sensor for hydrogen detection." Sensors and Actuators B-Chemical 134(2): 687-693.

[72] Tang, X., K. Remmel, et al. (2009). "Perovskite-Type Oxide Thin Film Integrated Fiber Optic Sensor for High-Temperature Hydrogen Measurement." Analytical Chemistry 81(18): 7844-7848.

[73] Liu, N., J. Hui, et al. (2006). "Nanoporous zeolite thin film-based fiber intrinsic Fabry-Perot interferometric sensor for detection of dissolved organics in water." Sensors 6(8): 835-847.

[74] Ahn, S. K., R. M. Kasi, et al. (2008). "Stimuli-responsive polymer gels." Soft Matter **4**(6): 1151-1157.

[75] Wu, T., P. Gong, et al. (2007). "Behavior of surface-anchored poly(acrylic acid) brushes with grafting density gradients on solid substrates: 1. Experiment." Macromolecules **40**(24): 8756-8764.

[76] Xu, C., T. Wu, et al. (2006). "Effect of block length on solvent response of block copolymer brushes: Combinatorial study with block copolymer brush gradients." Macromolecules **39**(9): 3359-3364.

[77] Stuart, M. A. C., W. T. S. Huck, et al. (2010). "Emerging applications of stimuli-responsive polymer materials." Nature Materials **9**(2): 101-113.

[78] Ionov, L. and S. Minko (2012). "Mixed Polymer Brushes with Locking Switching." ACS Applied Materials & Interfaces **4**(1): 483-489.

[79] Decher, G., J. Maclennan, et al. (1991). "Highly-Ordered Ultrathin LC Multilayer Films on Solide Substrates." Advanced Materials **3**(12): 617-619.

[80] Tan, H. L., M. J. McMurdo, et al. (2003). "Temperature dependence of polyelectrolyte multilayer assembly." Langmuir **19**(22): 9311-9314.

[81] Ram, M. K., M. Salerno, et al. (1999). "Physical properties of polyaniline films: Assembled by the layer-by-layer technique." Langmuir **15**(4): 1252-1259.

[82] Dubas, S. T. and J. B. Schlenoff (1999). "Factors controlling the growth of polyelectrolyte multilayers." Macromolecules **32**(24): 8153-8160.

[83] Stockton, W. B. and M. F. Rubner (1997). "Molecular-level processing of conjugated polymers .4. Layer-by-layer manipulation of polyaniline via hydrogen-bonding interactions." Macromolecules **30**(9): 2717-2725.

[84] Serizawa, T., K. Nanameki, et al. (2002). "Thermoresponsive ultrathin hydrogels prepared by sequential chemical reactions." Macromolecules **35**(6): 2184-2189.

[85] Goicoechea, J., C. R. Zamarreno, et al. (2008). "Optical fiber pH sensors based on layer-by-layer electrostatic self-assembled Neutral Red." Sensors and Actuators B-Chemical **132**(1): 305-311.

[86] Delcea, M., H. Mohwald, et al. (2011). "Stimuli-responsive LbL capsules and nanoshells for drug delivery." Advanced Drug Delivery Reviews **63**(9): 730-747.

[87] Wang, W., L. Liu, et al. (2009). "A Novel Thermo-Induced Self-Bursting Microcapsule with Magnetic-Targeting Property." Chemphyschem **10**(14): 2405-2409.

[88] Quinn, J. F., A. P. R. Johnston, et al. (2007). "Next generation, sequentially assembled ultrathin films: beyond electrostatics." Chemical Society Reviews **36**(5): 707-718.

[89] Buenger, D., F. Topuz, et al. (2012). "Hydrogels in sensing applications." Progress in Polymer Science **37**(12): 1678-1719.

[90] Flory, P. J. and J. Rehner (1943). "Statistical mechanics of cross-linked polymer networks I Rubberlike elasticity." Journal of Chemical Physics **11**(11): 512-520.

[91] Flory, P. J. and J. Rehner (1943). "Statistical mechanics of cross-linked polymer networks II Swelling." Journal of Chemical Physics **11**(11): 521-526.

[92] Flory, P. J. (1950). "Statistical mechanics of swelling of network structures." Journal of Chemical Physics **18**(1): 108-111.

[93] Edwards, S. F. (1977). "Theory of Rubber Elasticity." British Polymer Journal **9**(2): 140-143.

[94] Peppas, N. A. (2004) "Biomaterials Science: An Introduction to Materials in Medicine" Academic Press, New York p100-107

[95] Peppas, N. A. and E. W. Merrill (1977). "Crosslinked poly(vinyl alcohol) hydrogels as swollen elastic networks." Journal of Applied Polymer Science **21**(7): 1763-1770.

[96] Gerlach, G., M. Guenther, et al. (2004). "Application of sensitive hydrogels in chemical and pH sensors." Macromolecular Symposia **210**: 403-410.

[97] Tang, T., V. Castelletto, et al. (2006). "Thermo-responsive poly(methyl methacrylate)-block-poly(N-isopropylacrylamide) block copolymers synthesized by RAFT polymerization: Micellization and gelation." Macromolecular Chemistry and Physics **207**(19): 1718-1726.

[98] Cai, Q. Y., K. F. Zeng, et al. (2004). "A wireless, remote query glucose biosensor based on a pH-sensitive polymer." Analytical Chemistry **76**(14): 4038-4043.

[99] Kim, J. S., N. Singh, et al. (2006). "Label-free biosensing with hydrogel microlenses." Angewandte Chemie-International Edition **45**(9): 1446-1449.

[100] Ehrick, J. D., S. Stokes, et al. (2007). "Chemically tunable lensing of stimuli-responsive hydrogel microdomes." Advanced Materials **19**(22): 4024-+.

[101] Sato, Y., S. Ikegaki, et al. (2003). "Hydrogel-microsphere-enhanced surface plasmon resonance for the detection of a K-ras point mutation employing peptide nucleic acid." Journal of Biomaterials Science-Polymer Edition **14**(8): 803-820.

[102] Fine, T., P. Leskinen, et al. (2006). "Luminescent yeast cells entrapped in hydrogels for estrogenic endocrine disrupting chemical biodetection." Biosensors & Bioelectronics **21**(12): 2263-2269.

[103] Endo, T., R. Ikeda, et al. (2008). "Stimuli-responsive hydrogel-silver nanoparticles composite for development of localized surface plasmon resonance-based optical biosensor." Analytica Chimica Acta **611**(2): 205-211.

[104] Sharma, P. S., M. Dabrowski, et al. (2013). "Surface development of molecularly imprinted polymer films to enhance sensing signals." Trac-Trends in Analytical Chemistry **51**: 146-157.

[105] Whitcombe, M. J., I. Chianella, et al. (2011). "The rational development of molecularly imprinted polymer-based sensors for protein detection." Chemical Society Reviews **40**(3): 1547-1571.

[106] Lanza, F. and B. Sellergren (1999). "Method for synthesis and screening of large groups of molecularly imprinted polymers." Analytical Chemistry **71**(11): 2092-2096.

[107] Chianella, I., M. Lotierzo, et al. (2002). "Rational design of a polymer specific for microcystin-LR using a computational approach." Analytical Chemistry **74**(6): 1288-1293.

[108] Liao, P.-C., Y.-C. Tyan, et al. (2009). "Assessing the binding selectivity of molecularly imprinted polymer artificial antibodies by mass spectrometry-based profiling system." Journal of Biomedical Materials Research Part A 91A(2): 597-604.

[109] Wang, H., Y. He, et al. (2009). "BSA-imprinted synthetic receptor for reversible template recognition." Journal of Separation Science 32(11): 1981-1986.

[110] Tai, D.-F., M.-H. Jhang, et al. (2010). "Epitope-Cavities Generated by Molecularly Imprinted Films Measure the Coincident Response to Anthrax Protective Antigen and Its Segments." Analytical Chemistry 82(6): 2290-2293.

[111] Okutucu, B., F. Zihnioglu, et al. (2008). "Shell-core imprinted polyacrylamide crosslinked chitosan for albumin removal from plasma." Journal of Biomedical Materials Research Part A 84A(3): 842-845.

[112] Lin, Y., S. Tang, et al. (2008). "Protein recognition via molecularly imprinted agarose gel membrane." Journal of Biomedical Materials Research Part A 85A(3): 573-581.

[113] Kan, X., Q. Zhao, et al. (2010). "Preparation and Recognition Properties of Bovine Hemoglobin Magnetic Molecularly Imprinted Polymers." Journal of Physical Chemistry B 114(11): 3999-4004.

[114] Li, F., J. Li, et al. (2008). "Molecularly imprinted polymer grafted on polysaccharide microsphere surface by the sol-gel process for protein recognition." Talanta 74(5): 1247-1255.

[115] Yao, W., B. Ning, et al. (2008). "Recognition of Staphylococcus enterotoxin via molecularly imprinted beads." Journal of Separation Science 31(2): 413-418.

[116] Wang, Y., Y. Zhou, et al. (2008). "A potentiometric protein sensor built with surface molecular imprinting method." Biosensors & Bioelectronics 24(1): 162-166.

[117] Lu, Y., C.-L. Yan, et al. (2009). "Protein imprinting and recognition via forming nanofilms on microbeads surfaces in aqueous media." Applied Surface Science 256(5): 1341-1346.

[118] Shiomi, T., M. Matsui, et al. (2005). "A method for the molecular imprinting of hemoglobin on silica surfaces using silanes." Biomaterials 26(27): 5564-5571.

[119] Ferreira, G. N. M., A. C. Da-Silva, et al. (2009). "Acoustic wave biosensors: physical models and biological applications of quartz crystal microbalance." Trends in Biotechnology **27**(12): 689-697.

[120] Sauerbrey, G.Z. (1959) "Use of quartz vibrator for weighing thin films on a microbalance".Z. Phys.155, 206–222

[121] Lavrik, N. V., M. J. Sepaniak, et al. (2004). "Cantilever transducers as a platform for chemical and biological sensors." Review of Scientific Instruments **75**(7): 2229-2253.

[122]Bashir, R., J. Z. Hilt, et al. (2002). "Micromechanical cantilever as an ultrasensitive pH microsensor." Applied Physics Letters **81**(16): 3091-3093.

[123] Abu-Lail, N. I., M. Kaholek, et al. (2006). "Micro-cantilevers with end-grafted stimulus-responsive polymer brushes for actuation and sensing." Sensors and Actuators B-Chemical **114**(1): 371-378.

[124] Wohltjen, H. and R. Dessy (1979). "Surface Acoustic-Wave Probes for Chemical-Analysis. 2. Gas-Chromatography Dectector." Analytical Chemistry **51**(9): 1465-1470.

[125]Voiculescu, I. and A. N. Nordin (2012). "Acoustic wave based MEMS devices for biosensing applications." Biosensors & Bioelectronics **33**(1): 1-9.

[126] Pui, T. S., A. Agarwal, et al. (2009). "Ultra-sensitive detection of adipocytokines with CMOS-compatible silicon nanowire arrays." Nanoscale **1**(1): 159-163.

[127] Sallacan, N., M. Zayats, et al. (2002). "Imprinting of nucleotide and monosaccharide recognition sites in acrylamidephenylboronic acid-acrylamide copolymer membranes associated with electronic transducers." Analytical Chemistry **74**(3): 702-712.

[128] Gabai, R., N. Sallacan, et al. (2001). "Characterization of the swelling of acrylamidophenylboronic acid-acrylamide hydrogels upon interaction with glucose by faradaic impedance spectroscopy, chronopotentiometry, quartz-crystal microbalance (QCM), and surface plasmon resonance (SPR) experiments." Journal of Physical Chemistry B **105**(34): 8196-8202.

[129] Tokareva, I., I. Tokarev, et al. (2006). "Ultrathin molecularly imprinted polymer sensors employing enhanced transmission surface plasmon resonance spectroscopy." Chemical Communications(31): 3343-3345.

[130] Tokarev, I., I. Tokareva, et al. (2010). "Specific Biochemical-to-Optical Signal Transduction by Responsive Thin Hydrogel Films Loaded with Noble Metal Nanoparticles." Advanced Materials **22**(12): 1412-+.

[131] Dong, L., A. K. Agarwal, et al. (2006). "Adaptive liquid microlenses activated by stimuli-responsive hydrogels." Nature **442**(7102): 551-554.

[132] Tierney, S., D. R. Hjelme, et al. (2008). "Determination of swelling of responsive gels with nanometer resolution. Fiber-optic based platform for hydrogels as signal transducers." Analytical Chemistry **80**(13): 5086-5093.

[133] Tierney, S., S. Volden, et al. (2009). "Glucose sensors based on a responsive gel incorporated as a Fabry-Perot cavity on a fiber-optic readout platform." Biosensors & Bioelectronics **24**(7): 2034-2039.

[134] Marshall, A. J., J. Blyth, et al. (2003). "pH-sensitive holographic sensors." Analytical Chemistry **75**(17): 4423-4431.

[135] Kang, J. H., J. H. Moon, et al. (2008). "Thermoresponsive hydrogel photonic crystals by three-dimensional holographic lithography." Advanced Materials **20**(16): 3061-3065.

[136] Asher, S. A., J. Holtz, et al. (1998). "Mesoscopically periodic photonic-crystal materials for linear and nonlinear optics and chemical sensing." MRS Bulletin **23**(10): 44-50.

[137] Lee, K. and S. A. Asher (2000). "Photonic crystal chemical sensors: pH and ionic strength." Journal of the American Chemical Society **122**(39): 9534-9537.

[138] Kimble, K. W., J. P. Walker, et al. (2006). "Progress toward the development of a point-of-care photonic crystal ammonia sensor." Analytical and Bioanalytical Chemistry **385**(4): 678-685.

[139] Asher, S. A., V. L. Alexeev, et al. (2003). "Photonic crystal carbohydrate sensors: Low ionic strength sugar sensing." Journal of the American Chemical Society **125**(11): 3322-3329.

[140] Asher, S. A., A. C. Sharma, et al. (2003). "Photonic crystal aqueous metal cation sensing materials." Analytical Chemistry **75**(7): 1676-1683.

[141] Liedberg, B., C. Nylander, and I. Lundstrom (1983). "Surface-Plasmon Resonance for Gas Detection and Biosensing." Sensors and Actuators **4**(2): p. 299-304.

[142] Jonsson, U., et al. (1991). "Real-Time Biospecific Interaction Analysis Using Surface-Plasmon Resonance and a Sensor Chip Technology." Biotechniques. **11**(5): p. 620-&.

[143] Kretschm.E. (1971). "Determination of Optical Constants of Metals by Excitation of Surface Plasmons." Zeitschrift Fur Physik. **241**(4): p. 313-&.

[144] Maier, S.A., et al. (2002) “Observation of Near-Field Coupling in Metal Nanoparticle Chains Using Far-Field Polarization Spectroscopy.” Physical Review B. **65**(19).

[145] Huang, H., et al. (2009). “A Novel Label-Free Multi-Throughput Optical Biosensor Based on Localized Surface Plasmon Resonance.” Biosensors & Bioelectronics. **24**(7): p. 2255-2259.

[146] Jeong, H. H., N. Erdene, et al. (2011). "Fabrication of fiber-optic localized surface plasmon resonance sensor and its application to detect antibody-antigen reaction of interferon-gamma." Optical Engineering **50**(12).

[147] Shao, Y. L., S. P. Xu, et al. (2010). "Optical Fiber LSPR Biosensor Prepared by Gold Nanoparticle Assembly on Polyelectrolyte Multilayer." Sensors **10**(4): 3585-3596.

[148] Mitsui, K., Y. Handa, et al. (2004). "Optical fiber affinity biosensor based on localized surface plasmon resonance." Applied Physics Letters **85**(18): 4231-4233.

[149] Lee, H., H. J. Kim, et al. (2010). "Effects of surface density and size of gold nanoparticles in a fiber-optic localized surface plasmon resonance sensor and its application to peptide detection." Measurement Science & Technology **21**(8).

[150] Sai, V. V. R., T. Kundu, et al. (2009). "Novel U-bent fiber optic probe for localized surface plasmon resonance based biosensor." Biosensors & Bioelectronics **24**(9): 2804-2809.

[151] Chiang, C. Y., M. L. Hsieh, et al. "Fiber-optic particle plasmon resonance sensor for detection of interleukin-1β in synovial fluids." Biosensors and Bioelectronics **26**(3): 1036-1042.

[152] Cheng, S. F. and L. K. Chau (2003). "Colloidal gold-modified optical fiber for chemical and biochemical sensing." Analytical Chemistry **75**(1): 16-21.

[153] Chau, L. K., Y. F. Lin, et al. (2006). "Fiber-optic chemical and biochemical probes based on localized surface plasmon resonance." Sensors and Actuators B-Chemical **113**(1): 100-105.

[154] Lin, T. J. and M. F. Chung (2009). "Detection of cadmium by a fiber-optic biosensor based on localized surface plasmon resonance." Biosensors & Bioelectronics **24**(5): 1213-1218.

[155] Chen, C.H., et al. (2010). “Novel U-shape gold nanoparticles-modified optical fiber for localized plasmon resonance chemical sensing.” Microsystem Technologies-Micro-and Nanosystems-Information Storage and Processing Systems. 1**6(**7): p. 1207-1214.

[156] Tang, J.L., et al. (2006). “Fiber-optic biochemical sensing with a colloidal gold-modified long period fiber grating.” Sensors and Actuators B-Chemical. 1**19(**1): p. 105-109.

[157] Lee, J.Y., et al. (2008) “Single live cell refractometer using nanoparticle coated fiber tip.” Applied Physics Letters. **93**(17).

[158] http://www.nktphotonics.com/files/files/LMA-10.pdf

[159] Turkevich, J., P.C. Stevenson, and J. Hillier. (1951) “A study of the nucleation and growth processess in the synthesis of colloidal gold.” Discussions of the Faraday Society, 1951(11): p. 55-&.

[160] Haiss, W., et al. (2007). “Determination of size and concentration of gold nanoparticles from UV-Vis spectra.” Analytical Chemistry. 7**9(**11): p. 4215-4221.

[161] Bohren, C. F.; Huffman, D. R. (1983). “Absorption and Scattering of Light by Small Particles.” Wiley-Interscience: New York.

[162] Johnson, P. B. and R. W. Christy (1972). "Optical constants of noble metals." Physical Review B **6**(12): 4370-4379.

[163] Frens, G. (1973). “Controlled nucleation for regulation of particle-size in monodisperse god suspensions.” Nature-Physical Science. 2**41(**105): p. 20-22.

[164] Tu, M. H., T. Sun, et al. (2012). "Optimization of gold-nanoparticle-based optical fibre surface plasmon resonance (SPR)-based sensors." Sensors and Actuators B-Chemical **164**(1): 43-53.

[165] Srivastava, J., D. L. Barber, et al. (2007). "Intracellular pH sensors: Design principles and functional significance." Physiology **22**: 30-39.

[166] Lin, J. (2000). "Recent development and applications of optical and fiber-optic pH sensors." Trac-Trends in Analytical Chemistry **19**(9): 541-552.

[167] Korostynska, O., K. Arshak, et al. (2008). "Review paper: Materials and techniques for in vivo pH monitoring." Ieee Sensors Journal **8**(1-2): 20-28.

[168] http://www.electrochem.org/dl/interface/sum/sum04/if6-04-pages19-20.pdf

[169] McKinley, B. A. (2008). "ISFET and fiber optic sensor technologies: In vivo experience for critical care monitoring." Chemical Reviews **108**(2): 826-844.

[170] M.J.P. Leiner, O.S. Wolfbeis, in: O.S. Wolfbeis (Editor). (1991). “Fiber Optic Chemical Sensors and Biosensors, Vol. I.” CRC Press, Boca Raton, FL, p. 359.

[171] Peterson, J. I., S. R. Goldstein, et al. (1980). "Fiber optic pH probe for physiological use." Analytical Chemistry **52**(6): 864-869.

[172] Jin, W. Z., L. X. Wu, et al. (2011). "Continuous Intra-Arterial Blood pH Monitoring by a Fiber-Optic Fluorosensor." IEEE Transactions on Biomedical Engineering **58**(5): 1232-1238.

[173] Henning, P. E. and P. Geissinger (2012). "Application of time-correlated single photon counting and stroboscopic detection methods with an evanescent-wave fibre-optic sensor for fluorescence-lifetime-based pH measurements." Measurement Science & Technology **23**(4).

[174] Anker, J. N., W. P. Hall, et al. (2008). "Biosensing with plasmonic nanosensors." Nature Materials **7**(6): 442-453.

[175] Hutter, E. and J. H. Fendler (2004). "Exploitation of localized surface plasmon resonance." Advanced Materials **16**(19): 1685-1706.

[176] Sun, X. P., S. J. Dong, et al. (2005). "One-step preparation of highly concentrated well-stable gold colloids by direct mix of polyelectrolyte and HAuCl4 aqueous solutions at room temperature." Journal of Colloid and Interface Science **288**(1): 301-303.

[177] Busher, K., K. Graf, et al. (2002). "Influence of adsorption conditions on the structure of polyelectrolyte multilayers." Langmuir **18**(9): 3585-3591.

[178] Ladam, G., P. Schaad, et al. (2000). "In situ determination of the structural properties of initially deposited polyelectrolyte multilayers." Langmuir **16**(3): 1249-1255.

[179] Brust, M., D. Bethell, et al. (1998). "Self-assembled gold nanoparticle thin films with nonmetallic optical and electronic properties." Langmuir **14**(19): 5425-5429.

[180] Jiang, C. Y., S. Markutsya, et al. (2004). "Collective and individual plasmon resonances in nanoparticle films obtained by spin-assisted layer-by-layer assembly." Langmuir **20**(3): 882-890.

[181] Rinaudo, M. (2006). "Chitin and chitosan: Properties and applications." Progress in Polymer Science **31**(7): 603-632.

[182] Caner, C., P. J. Vergano, et al. (1998). "Chitosan film mechanical and permeation properties as affected by acid, plasticizer, and storage." Journal of Food Science **63**(6): 1049-1053.

[183]Devlieghere, F., A. Vermeulen, et al. (2004). "Chitosan: antimicrobial activity, interactions with food components and applicability as a coating on fruit and vegetables." Food Microbiology **21**(6): 703-714.

[184] Riva, R., H. Ragelle, et al. (2011). "Chitosan and Chitosan Derivatives in Drug Delivery and Tissue Engineering." Chitosan for Biomaterials Ii. R. Jayakumar, M. Prabaharan and R. A. A. Muzzarelli. **244:** 19-44.

[185] Miretzky, P. and A. F. Cirelli (2009). "Hg(II) removal from water by chitosan and chitosan derivatives: A review." Journal of Hazardous Materials **167**(1-3): 10-23.

[186] Park, J. W., K. H. Choi, et al. (1983). "Acid-base equilibria and related properties of Chitosan." Bulletin of the Korean Chemical Society **4**(2): 68-72.

[187] Sen, A. K., S. Roy, et al. (2007). "Effect of structure on solution and interfacial properties of sodium polystyrene sulfonate (NaPSS)." Polymer International **56**(2): 167-174.

[188] Castro, C., L. Gargallo, et al. (2011). "Blends containing chitosan and poly(sodium-4-styrene sulphonate). Compatibility behavior." Carbohydrate Polymers **83**(1): 81-87.

[189]Aravind, U. K., J. Mathew, et al. (2007). "Transport studies of BSA, lysozyme and ovalbumin through chitosan/polystyrene sulfonate multilayer membrane." Journal of Membrane Science **299**(1-2): 146-155.

[190] Katchalsky, A. and P. Spitnik (1947). "Potentiometric titrations of polymethacrylic acid." Journal of Polymer Science **2**(4): 432-446.

[191] Sorlier, P., A. Denuziere, et al. (2001). "Relation between the degree of acetylation and the electrostatic properties of chitin and chitosan." Biomacromolecules **2**(3): 765-772.

[192] Rmaile, H. H. and J. B. Schlenoff (2002). ""Internal pK(a)'s" in polyelectrolyte multilayers: Coupling protons and." Langmuir **18**(22): 8263-8265.

[193]Joshi, G. K., M. A. Johnson, et al. (2014). "Novel pH-responsive nanoplasmonic sensor: controlling polymer structural change to modulate localized surface plasmon resonance response." Rsc Advances **4**(30): 15807-15815.

[194] Shao, L.-Y., M.-J. Yin, et al. (2013). "Fiber Optic pH Sensor with Self-Assembled Polymer Multilayer Nanocoatings." Sensors **13**(2): 1425-1434.

[195] Gui, Z., J. Qian, et al. (2010). "A novel fast response fiber-optic pH sensor based on nanoporous self-assembled multilayer films." Journal of Materials Chemistry **20**(36): 7754-7760.

[196] Gilbert Boisde, Alan Harmer. (1996) “Chemical and biochemical sensing with optical fibers and waveguides.” Artech House: Page 226-228

[197] B. Culshaw. (1984) “Optical fibre sensing and signal processing.” Peter Peregrinus Ltd: Page 87-88

[198] Tan, Y. Z., L. P. Sun, et al. (2013). "Microfiber Mach-Zehnder interferometer based on long period grating for sensing applications." Optics Express **21**(1): 154-164.

[199] Yu, X. J., G. Li, et al. (2012). “Characteristics of in-fiber Mach-Zehnder interferometer formed by lateral offset splicing.” Advanced Sensor Systems and Applications V. B. Culshaw, Y. Liao, A. Wang, X. Bao and X. Fan. **8561**.

[200] Rong, Q. Z., X. G. Qiao, et al. (2012). "High-Sensitive Fiber-Optic Refractometer Based on a Core-Diameter-Mismatch Mach-Zehnder Interferometer." IEEE Sensors Journal **12**(7): 2501-2505.

[201] Shao, M., X. G. Qiao, et al. (2014). "A Mach-Zehnder interferometric humidity sensor based on waist-enlarged tapers." Optics and Lasers in Engineering **52**: 86-90.

[202] Choi, H. Y., M. J. Kim, et al. (2007). "All-fiber Mach-Zehnder type interferometers formed in photonic crystal fiber." Optics Express **15**(9): 5711-5720.

[203] Russell, P. (2003). "Photonic crystal fibers." Science **299**(5605): 358-362.

[204] Wang, S. Q., H. Zhao, et al. (2008). "Silver-coated near field optical scanning microscope probes fabricated by silver mirror reaction." Applied Physics B-Lasers and Optics **92**(1): 49-52.

[205] Wu, D., T. Zhu, et al. (2011). "Refractive index sensing based on Mach-Zehnder interferometer formed by three cascaded single-mode fiber tapers." Applied Optics **50**(11): 1548-1553.

[206] Geng, Y., X. Li, et al. (2011). "A cascaded photonic crystal fiber Mach-Zehnder interferometer formed by extra electric arc discharges." Applied Physics B-Lasers and Optics **102**(3): 595-599.

[207] Kim, D. J., S. M. Kang, et al. (2005). "Formation of thermoresponsive gold nanoparticle/PNIPAAm hybrids by surface-initiated, atom transfer radical polymerization in aqueous media." Macromolecular Chemistry and Physics **206**(19): 1941-1946.

[208] Flory, P. J. (1941). "Thermodynamics of high polymer solutions." Journal of Chemical Physics **9**(8): 660-661.

[209] Huggins, M. L. (1941). "Solutions of long chain compounds." Journal of Chemical Physics **9**(5): 440-440.

[210] Brannonpeppas, L. and N. A. Peppas (1991). "Equilibrium swelling behavior of pH-sensitive hydrogels." Chemical Engineering Science **46**(3): 715-722.

[211] Wen, S., X. N. Yin, et al. (1991). "Preparation and characterization of polyelectrolyte copolymers containing methyl-methacrylate and 2-hydroxyethyl methacrylate. 2. Polymers based on dimethylaminoethyl methacrylate." Journal of Applied Polymer Science **43**(1): 205-212.

[212] Yin, M. J., B. B. Gu, et al. (2011). "Highly sensitive and fast responsive fiber-optic modal interferometric pH sensor based on polyelectrolyte complex and polyelectrolyte self-assembled nanocoating." Analytical and Bioanalytical Chemistry **399**(10): 3623-3631.

[213] Gu, B., M. J. Yin, et al. (2009). "Low-cost high-performance fiber-optic pH sensor based on thin-core fiber modal interferometer." Optics Express **17**(25): 22296-22302.

[214] Richter, A., G. Paschew, et al. (2008). "Review on hydrogel-based pH sensors and microsensors." Sensors **8**(1): 561-581.

[215] Chu, Y., P. P. Varanasi, et al. (1995). "pH-induced swelling kinetics of polyelectrolyte hydrogels." Journal of Applied Polymer Science **58**(12): 2161-2176.

[216] Gillies, R. J., N. Raghunand, et al. (2002). "MRI of the tumor microenvironment." Journal of Magnetic Resonance Imaging **16**(4): 430-450.

[217] Moellering, R. E., K. C. Black, et al. (2008). "Acid treatment of melanoma cells selects for invasive phenotypes." Clinical & Experimental Metastasis **25**(4): 411-425.

[218] Rofstad, E. K., B. Mathiesen, et al. (2006). "Acidic extracellular pH promotes experimental metastasis of human melanoma cells in athymic nude mice." Cancer Research **66**(13): 6699-6707.

[219] Holtz, J. H. and S. A. Asher (1997). "Polymerized colloidal crystal hydrogel films as intelligent chemical sensing materials." Nature **389**(6653): 829-832.

[220] Charles, P. T., E. R. Goldman, et al. (2004). "Fabrication and characterization of 3D hydrogel microarrays to measure antigenicity and antibody functionality for biosensor applications." Biosensors & Bioelectronics **20**(4): 753-764.

[221] Denkhaus, E. and K. Salnikow (2002). "Nickel essentiality, toxicity, and carcinogenicity." Critical Reviews in Oncology Hematology **42**(1): 35-56.

[222] Aragay, G., J. Pons, et al. (2011). "Recent Trends in Macro-, Micro-, and Nanomaterial-Based Tools and Strategies for Heavy-Metal Detection." Chemical Reviews **111**(5): 3433-3458.

[223] Vazqueztorres, H., J. V. Cauichrodriguez, et al. (1993). "Poly(vinyl alcohol) Poly(acrylic acid) blends- Miscibility studies by DSC and characterization of their thermally-induced hydrogels." Journal of Applied Polymer Science **50**(5): 777-792.

[224] Tanaka, T. and D. J. Fillmore (1979). "Kinetics of swelling of gels." Journal of Chemical Physics **70**(3): 1214-1218.

[225] Elena M. Filip, Ionel V. Humelnicu, et al. (2009). "Some aspects of 8-hydroxyquinoline in Solvents." ACTA CHEMICA IASI **17**: 85-96

[226] Sorber, J., G. Steiner, et al. (2008). "Hydrogel-based piezoresistive pH sensors: Investigations using FT-IR attenuated total reflection spectroscopic Imaging." Analytical Chemistry **80**(8): 2957-2962.

[227] Baiocchi, C., G. Saini, et al. (1988). "Pre-cloumn chelation with 8-hydroxyquinoline for the simulataneous determination of metal-ions by reversed-phase high-performance liquid-chromatography." Analyst **113**(5): 805-807.

[228] Sugawara, K. F., H. H. Weetall, et al. (1974). "Preparation, properties and applications of 8-hydroxyquinoline immobilized chelate." Analytical Chemistry **46**(4): 489-492.

[229] Richard, C. F., R. L. Gustafson, et al. (1959). "Stability of metal chelates of 8-quinolinol-5-sulfonate." Journal of the American Chemical Society **81**(5): 1033-1040.

[230] U.S. Environmental Protection Agency. "Risk Assessment, Management and Communication of Drinking Water Contamination." US EPA 625/4-89/024, EPA: Washington, DC, 1989

[231] Gander, B., R. Gurny, et al. (1989). "Effect of polymeric network structure on drug release from cross-linked poly(vinyl alcohol) micromatrices." Pharmaceutical Research **6**(7): 578-584.

[232]Veronica Estrella, et al. (2013) “Acidity generated by the tumor microenvironment drives local invasion.” Cancer Research **73**: 1524-1535.

[233]Robert A. Gatenby, et al. (2006) “Acid-mediated tumor invasion: a multidisciplinary study.” Cancer Research **66**: 5216-5223.

[234]Fukumura D, Xu L, Chen Y, et al. (2000). “Hypoxia and acidosis independently up-regulate vascular endothelial growth factor transcription in brain tumors in vivo.” Cancer Res. 61: 6020–4

[235] Del Rosso M, Fibbi G, Pucci M, et al. (2002). “Multiple path-ways of cell invasion are regulated by multiple families of serine proteases.” Clin Exp Metastasis. 19: 193–207.

[236] Fischer K, Hoffmann P, Voelkl S, et al. (2007). “Inhibitory effect of tumor cell-derived lactic acid on human T cells.” Blood. 109: 3812–9.

[237] Oliver, N. S., C. Toumazou, et al. (2009). "Glucose sensors: a review of current and emerging technology." Diabetic Medicine. **26**(3): 197-210.

[238] Ye, G., X. Y. Li, et al. (2010). "Diffraction grating of hydrogel functionalized with glucose oxidase for glucose detection." Chemical Communications **46**(22): 3872-3874.

[239] Zhang, C. J., M. D. Losego, et al. (2013). "Hydrogel-Based Glucose Sensors: Effects of Phenylboronic Acid Chemical Structure on Response." Chemistry of Materials **25**(15): 3239-3250.

[240] Cummins, B. M., J. T. Garza, et al. (2013). "Optimization of a Concanavalin A-Based Glucose Sensor Using Fluorescence Anisotropy." Analytical Chemistry **85**(11): 5397-5404.

[241] Aslan, K., et al. (2007). “Fluorescent core-shell Ag@SiO2 nanocomposites for metal-enhanced fluorescence and single nanoparticle sensing platforms.” Journal of the American Chemical Society. **129**(6): p. 1524-+.

[242] Raula, J., H. Eerikainen, et al. (2004). "Influence of the solvent composition on the aerosol synthesis of pharmaceutical polymer nanoparticles." International Journal of Pharmaceutics **284**(1-2): 13-21.

[243] Lee, S. W., K. E. Tettey, et al. (2012). "Controlling the Cell-Adhesion Properties of Poly(acrylic acid)/Polyacrylamide Hydrogen-Bonded Multilayers." Macromolecules **45**(15): 6120-6126.